

**Structural behaviour of a calcium silicate brick masonry assemblage
Quasi-static cyclic pushover and dynamic identification test (C31B60-7)**

Ravenshorst, Geert; Esposito, Rita; Schipper, Roel; Messali, Francesco; Tsouvalas, Apostolos; Lourens, Eliz-Mari; Rots, Jan

Publication date

2016

Document Version

Final published version

Citation (APA)

Ravenshorst, G., Esposito, R., Schipper, R., Messali, F., Tsouvalas, A., Lourens, E.-M., & Rots, J. (2016). *Structural behaviour of a calcium silicate brick masonry assemblage: Quasi-static cyclic pushover and dynamic identification test (C31B60-7)*. Delft University of Technology.

Important note

To cite this publication, please use the final published version (if applicable).
Please check the document version above.

Copyright

Other than for strictly personal use, it is not permitted to download, forward or distribute the text or part of it, without the consent of the author(s) and/or copyright holder(s), unless the work is under an open content license such as Creative Commons.

Takedown policy

Please contact us and provide details if you believe this document breaches copyrights.
We will remove access to the work immediately and investigate your claim.

<i>Project number</i>	C31B60
<i>File reference</i>	C31B60-7
<i>Date</i>	21 October 2016
<i>Corresponding author</i>	Geert Ravenshorst (g.j.p.ravenshorst@tudelft.nl) Rita Esposito (r.esposito@tudelft.nl)

Physical Testing and Modelling – Masonry Structures

STRUCTURAL BEHAVIOUR OF A CALCIUM SILICATE BRICK MASONRY ASSEMBLAGE: QUASI-STATIC CYCLIC PUSHOVER AND DYNAMIC IDENTIFICATION TEST

Authors: Geert J.P. Ravenshorst, Rita Esposito, Roel Schipper, Francesco Messali, Apostolos Tsouvalas, Eliz-Mari Lourens, Jan G. Rots

Cite as: Ravenshorst, G.J.P., Esposito, R., Schipper, R., Messali, F. Tsouvalas, A. Lourens, E-M., and Rots, J.G. Structural behaviour of a calcium silicate brick masonry assemblage: quasi-static cyclic pushover and dynamic identification test. Report No. C31B60-7, 21 October 2016. Delft University of Technology.

This document is made available via the website ‘Structural Response to Earthquakes’ and the TU Delft repository. While citing, please verify if there are recent updates of this research in the form of scientific papers.

All rights reserved. No part of this publication may be reproduced, stored in a retrieval system of any nature, or transmitted, in any form or by any means, electronic, mechanical, photocopying, recording or otherwise, without the prior written permission of TU Delft.

TU Delft and those who have contributed to this publication did exercise the greatest care in putting together this publication. This report will be available as-is, and TU Delft makes no representations of warranties of any kind concerning this Report. This includes, without limitation, fitness for a particular purpose, non-infringement, absence of latent or other defects, accuracy, or the presence or absence of errors, whether or not discoverable. Except to the extent required by applicable law, in no event will TU Delft be liable for on any legal theory for any special, incidental consequential, punitive or exemplary damages arising out of the use of this report.

This research work was funded by NAM Hazard and Risk stream.

Table of Contents

1	Introduction	4
2	Nomenclature	5
2.1	Symbols.....	5
2.2	Abbreviations	5
3	Description of the assembled structure.....	6
3.1	Material properties	6
3.2	Assembled structure	7
4	Quasi-static cyclic pushover test	12
4.1	Testing protocol	12
4.2	Experimental results	17
4.2.1	Global behaviour	17
4.2.2	Deformations and drifts	38
5	Dynamic identification test.....	41
5.1	Testing protocol	41
5.2	Experimental results	42
6	Interpretation of the results.....	44
6.1	Capacity.....	44
6.2	Asymmetric behaviour	46
6.3	Drifts	48
6.4	First natural frequency.....	49
7	Conclusions and recommendations.....	51
	References	53
	Appendixes	54
A.	Explanation of the load distribution on the assemblage during the test	54
B.	Instrumentation list	62
C.	Material Properties	70
D.	Capacity curve per cycle	72
E.	Photographic documentation	85

1 Introduction

Within the framework of the large-scale testing campaign developed in 2015 within the NAM Hazard & Risk project, a quasi-static cyclic pushover test on a masonry assemblage has been performed at the Stevin II laboratory of Delft University of Technology. Additionally, dynamic identification tests have been performed at various damage levels to identify the dynamic properties of the structure. The test has been designed to serve as a benchmark for the validation of numerical and analytical models.

A two-storey assembled structure composed of calcium silicate masonry walls and concrete floors has been chosen as the object of the test. The assembled structure is representative of a typical terraced house built in the period between 1960 and 1980 in the Groningen area. The geometry of the assemblage has been designed to investigate the influence of the following buildings' characteristics:

- Presence of slender piers, due to the presence of large openings in the facades
- Presence of long transversal walls that are connected to the facades by the running bond
- Limited connection between concrete floor and masonry wall

The test does not address the influence of the following characteristics:

- Interaction between soil and structure
- Presence of spandrels connecting the masonry piers and openings
- Cooperation between inner and outer leaf of cavity walls

The assembled structure has been tested under quasi-static cyclic pushover load and at different stages a dynamic identification test has been performed. The objective of pushover test is to determine the structural response of the structure under cyclic loading in terms of load-displacement relationship, which provides information on the capacity and ductility of the structure, and to investigate the crack propagation during the test. The objective of the dynamic identification test is to determine the eigenfrequencies of the structure at different damage states.

In this report, the main experimental results are reported. Section 2 presents the adopted nomenclature. A description of the adopted material and the geometry of the assemblage are given in Section 3. Section 4 and Section 5 present respectively the cyclic pushover and the dynamic identification test. Section 6 reports a further interpretation of the results. Concluding remarks and recommendations for future tests are given in Section 7.

2 Nomenclature

2.1 Symbols

This report adopts mainly the nomenclature used in Eurocode 6 and 8.

μ	Masonry (bed joint) shear strength coefficient
μ^*	Shear strength coefficient of bed joint between concrete and masonry
ω	Eigenvalue matrix from which the natural frequencies can be determined
d_1	Average displacement measured at the first floor level
d_2	Average displacement measured at the second floor level
$d_{2,\min}$	Minimum value of d_2 for the i -th cycles
$d_{2,\max}$	Maximum value of d_2 for the i -th cycles
d_r	Drift
f_{cc}	Cubic compressive strength of concrete
f'_m	Compressive strength of masonry in the direction perpendicular to the bed joints
$f'_{m,h}$	Compressive strength of masonry in the direction parallel to the bed joints
f_{x1}	Masonry flexural strength with the moment vector parallel to the bed joints and in the plane of the wall, which generates a plane of failure parallel to the bed joints
f_{x2}	Masonry flexural strength with the moment vector orthogonal to the bed joints and in the plane of the wall, which generates a plane of failure perpendicular to the bed joints
f_{x3}	Masonry flexural strength with the moment vector orthogonal to the plane of the wall
f_{v0}	Masonry (bed joint) initial shear strength
f^*_{v0}	Initial shear strength of the dry connection (mortar bed joint) between concrete floor and masonry wall
f_w	Masonry uniaxial bond strength between the masonry unit and the mortar
E_3	Chord elastic modulus of masonry subject to a compressive loading perpendicular to the bed joints, evaluated at between 1/10 and 1/3 of the maximum stress
$E_{3,h}$	Chord elastic modulus of masonry subject to a compressive loading parallel to the bed joints, evaluated at between 1/10 and 1/3 of the maximum stress
F_j	Force in the j -th hydraulic actuator
K	Stiffness matrix
M	Mass matrix

2.2 Abbreviations

Avg.	Average
C.o.V.	Coefficient of variation
FF	First floor
GF	Ground floor
SF	Second floor
St. Dev.	Standard deviation

2.3 Terminology

Base shear force	Total lateral force applied to the assembled structure, measured as the sum of the forces in the actuators.
Capacity	Maximum resistance of the assembled structure to withstand the lateral forces.
Capacity curve	The relation between base shear force and the control displacement.
Control displacement	Generally, average displacement of the assembled structure measured at the second floor level. In some cases where specified, average displacement of the assembled structure measured at the first floor level
Drift	Ratio between the relative floor displacement and the interstorey height

3 Description of the assembled structure

The assembled structure represents the inner bearing leaf of a terraced house, which was typically built in 1960-1980 in the Netherlands. In this section the materials properties and the structure characteristics are described.

3.1 Material properties

The replicated masonry adopted in the tested assemblage was composed of calcium silicate bricks and general purpose mortar. The bricks had a nominal dimension of 210x71x102 mm and a declared mean compressive strength of 16 MPa. A cement-based mortar in the M5 strength class was used. For both bricks and mortar a single batch of production was used. The thickness of both head and bed joints was set to 10 mm with possible variation between 9 to 12 mm. A stretcher bond was selected. Each floor was made of two reinforced concrete slabs, with thickness of 165 mm and strength class C53/65. The slabs were connected in-situ by wet concrete joints.

The material properties of the calcium silicate masonry were determined in the first period of the campaign, when both material tests and large-scale tests on components were performed. During the construction of the assembled structure (second period), the following material tests were repeated: test on mortar, vertical compressive test on masonry, shear test on masonry and bond-wrench test. Table 3.1 lists the material properties of the calcium silicate masonry considering all the results obtained in the two periods. A detailed description of the material properties is reported in Appendix A and Ref. [1].

To characterise the friction behaviour of the wall-to-floor connection, a shear-compression test was performed similarly to the one for masonry. Being the floor laying on the loadbearing walls and connected by a mortar joint, the friction behaviour is of importance. Applying the Coulomb friction criterion, the friction properties of the floor-to-wall connection resulted similar to the shear properties of masonry (Table 3.1). Consequently, this connection can be considered equivalent to any other mortar joint [1].

Table 3.1 – Material properties of calcium silicate masonry and of the connection with concrete floor [1].

Symbol	Material property	Avg.	St. dev.	C.o.V.
		MPa	MPa	
f'_m	Compressive strength of masonry perpendicular to the bed joints	5.84	0.54	0.09
E_1	Elastic modulus of masonry in the direction perpendicular to bed joints evaluated between at 1/3 of the maximum compressive stress	3264	644	0.20
E_2	Elastic modulus of masonry in the direction perpendicular to bed joints evaluated between at 1/10 of the maximum compressive stress	4788	1768	0.37
E_3	Elastic modulus of masonry in the direction perpendicular to bed joints evaluated between 1/10 and 1/3 of the maximum compressive stress	2887	460	0.16
$f'_{m,h}$	Compressive strength of masonry parallel to the bed joints	7.55	0.17	0.02
$E_{1,h}$	Elastic modulus of masonry in the direction parallel to the bed joints evaluated between at 1/3 of the maximum compressive stress	2212	660	0.30
$E_{2,h}$	Elastic modulus of masonry in the direction parallel to the bed joints evaluated between at 1/10 of the maximum compressive stress	3583	1668	0.47
$E_{3,h}$	Elastic modulus of masonry in the direction parallel to the bed joints evaluated between 1/10 and 1/3 of the maximum compressive stress	2081	864	0.42
$f_{x,1}$	Out-of-plane masonry flexural strength parallel with the bed joint	0.21	0.05	0.25
$f_{x,2}$	Out-of-plane masonry flexural strength perpendicular to the bed joint	0.76	0.36	0.47
$f_{x,3}$	In-plane masonry flexural strength perpendicular to the bed joint	0.40	0.09	0.23
f_w	Flexural bond strength	0.28	0.10	0.36
f_{v0}	Masonry (bed joint) initial shear strength	0.14	-	-
μ	Masonry (bed joint) shear friction coefficient	0.43	-	-
f^*_{v0}	Initial shear strength of bed joint between concrete and CS brick	0.09	-	-
μ^*	Shear friction coefficient of bed joint between concrete and CS brick	0.52	-	-
f_{cc}	Cubic compressive strength of concrete	74.7	1.7	0.08

3.2 Assembled structure

Figure 3.1 gives a 3D view of the assemblage with the orientation and nomenclature of the different parts. The assemblage is built on a steel substructure (blue parts in Figure 3.1). The first layer of masonry was glued on the steel substructure, with the glue Sikadur 30, to ensure that the connection of the masonry to the steel substructure is not governing. Consequently, cracking at the base of the assemblage appears in the first mortar joint between the first and second brick layer.

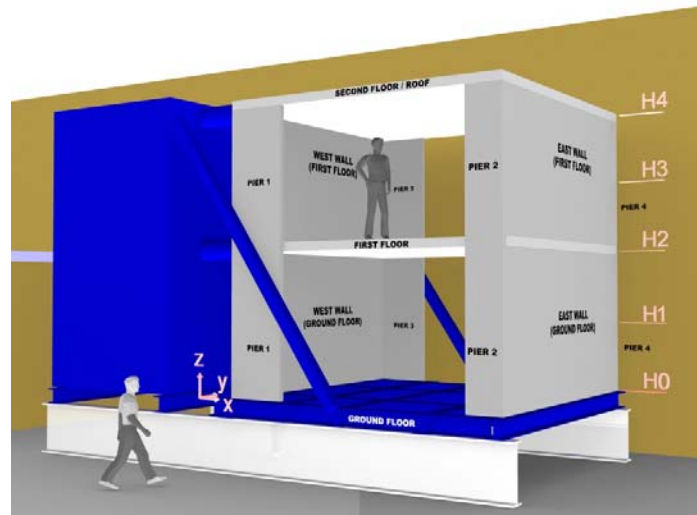


Figure 3.1 – 3D view of the assembled structure.

The structure consists of two loadbearing walls, on the west and east side, and two façades composed of two piers with width of 660 mm and 1100 mm. The masonry was made in stretcher bond (in Dutch "halfsteensverband") and a running bond was adopted at the corner between pier and loadbearing walls (in Dutch "vertand"). Figure 3.2, Figure 3.3 and Figure 3.4 shows the geometry of the structure.

The floors consisted of two prefabricated concrete slabs spanning between the loadbearing walls. The floors were laid up on the loadbearing floors in a mortar bed joint. The two concrete slabs were in-situ connected by reinforced concrete dowels. At first floor level, the floor was connected horizontally to the piers by anchors of 6 mm diameter, casted in the floor and masoned in the piers. The narrow piers are connected by three anchors, while the wide piers by five anchors (Figure 3.5). At the second floor level, the floor was laid on both the loadbearing walls and the piers. However, during construction the floor was first laid on the loadbearing walls and subsequently the joint between the pier and the floor was filled with mortar. As a consequence the load is carried out only by the loadbearing walls. Figure 3.6 shows a summary of the construction phases [2].

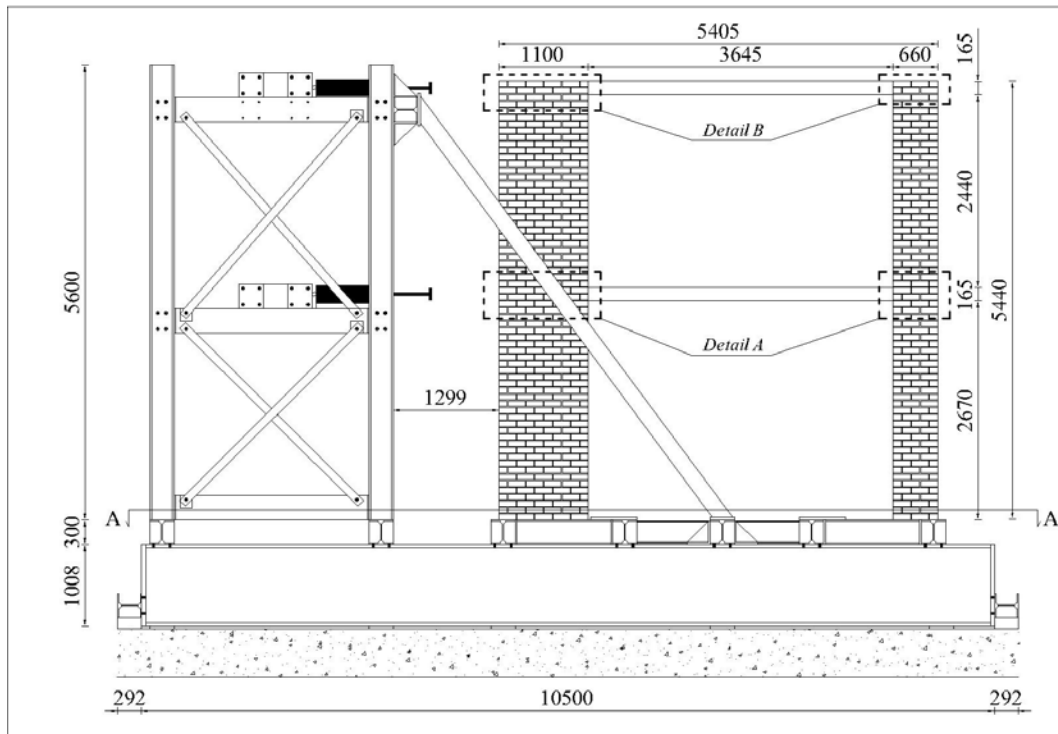


Figure 3.2 – Front view (South side).

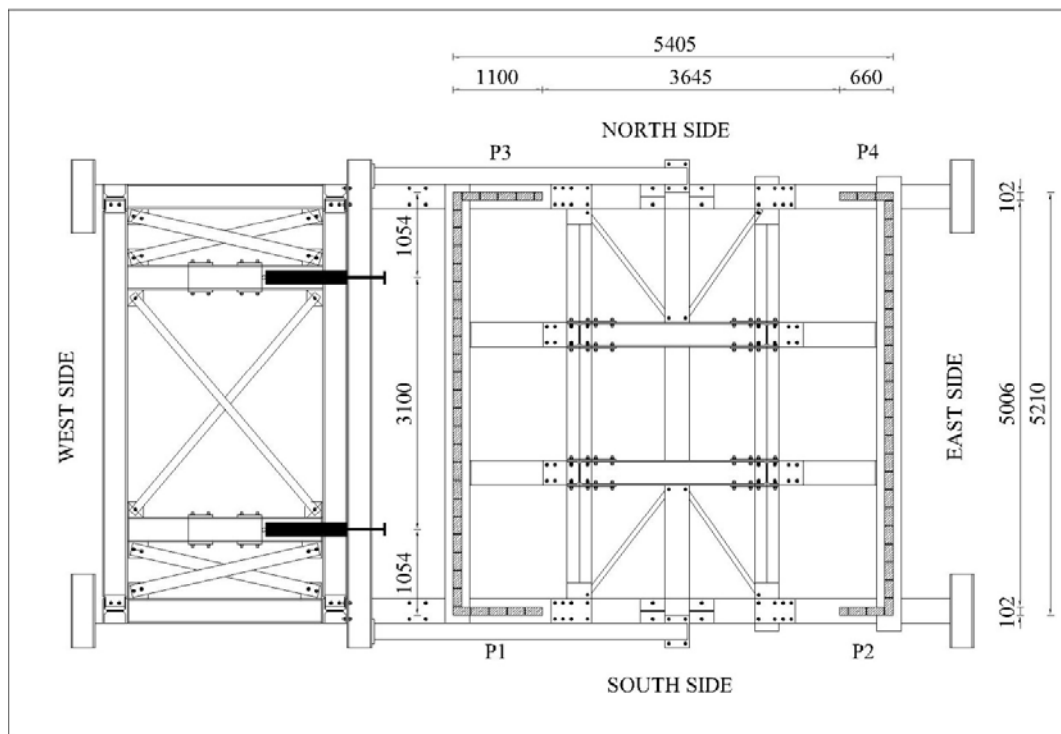


Figure 3.3 – Top view.

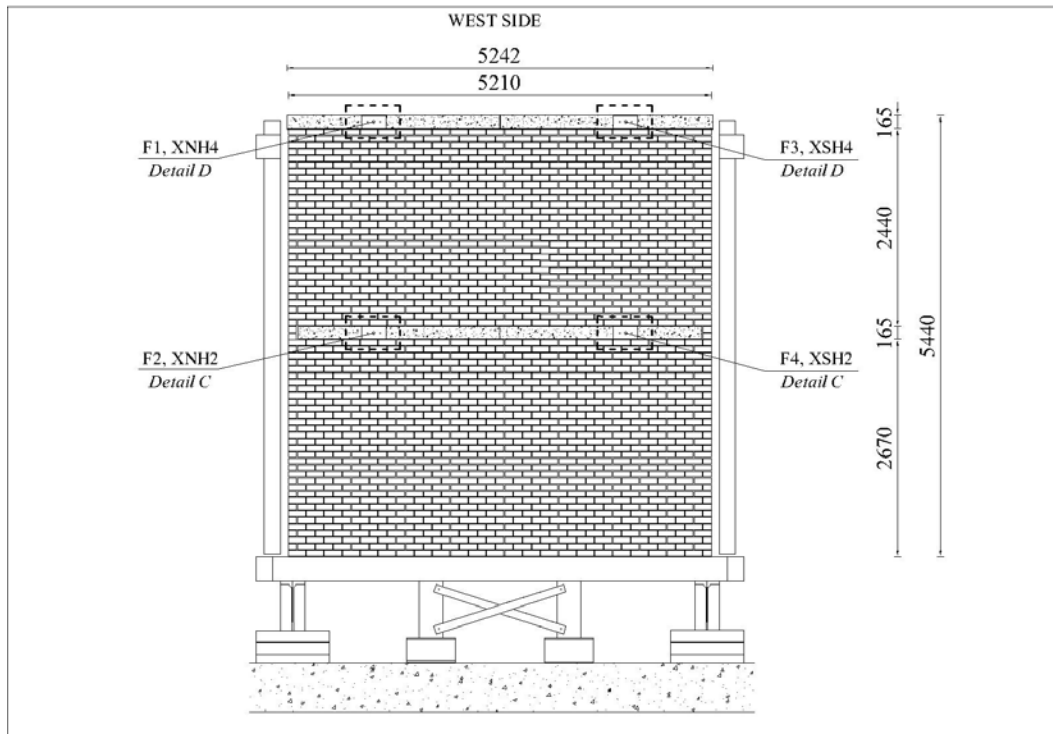
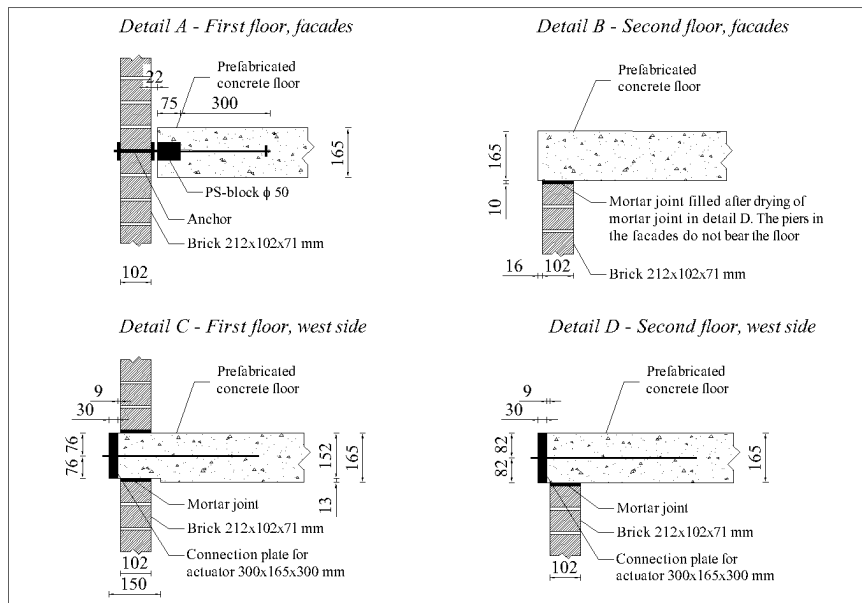


Figure 3.4 – Lateral view (west side).



(a)



(b)

Figure 3.5 – Construction detail of connections: (a) Connection between floor and walls; (b) Reinforcement in one of the in-situ casted shear joints between the two concrete slabs forming the floor.

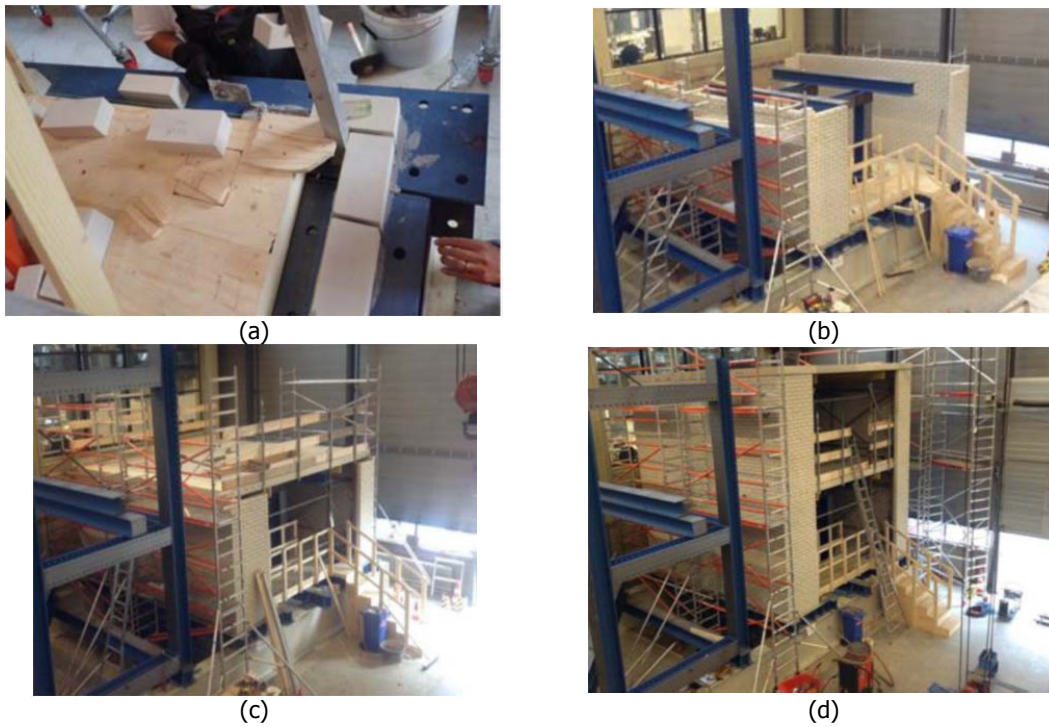


Figure 3.6 – Execution of the assembled structure: (a) gluing of the bottom layer to the steel substructure; (b) masoning of the loadbearing walls and facades from bottom to first floor; (c) positioning of the first floor; (d) Masoning of the loadbearing walls at the first floor and positioning of the second floor.

4 Quasi-static cyclic pushover test

4.1 Testing protocol

A quasi-static cyclic pushover test has been performed on the calcium silicate brick masonry assemblage by applying a lateral load at both floor levels. The aim of the test is to evaluate the structural behaviour along the X-axis under lateral load. To achieve this aim a deformation along the X-axis was applied and simultaneously forces at both floor levels were kept equal. A pre-described displacement was imposed by means of two actuators at the second floor level. The two actuators at the second floor level were coupled to the ones at the first floor level in order to impose a 1:1 ratio between the forces at the floor levels.

In order to apply the load at floor level, a steel reaction frame was built (Figure 4.1 and Figure 4.2). The tower and the assemblage were both connected at two steel HEM 1000 beams. The lateral forces from the actuators to the steel reaction frame and the assemblage make equilibrium in the two steel HEM 1000 beams. To make the steel tower stiff, two steel diagonal square tubes were connected from the top of the steel tower to the HEM 1000 beam. The vertical translation of the HEM 1000 beam from the lab floor was measured with potentiometers on several positions over the length of the beam, to evaluate the rotation of the steel reaction frame and the assemblage. Measurements during the tests showed that these translations in Z direction (and therefore the rotations) were negligible.

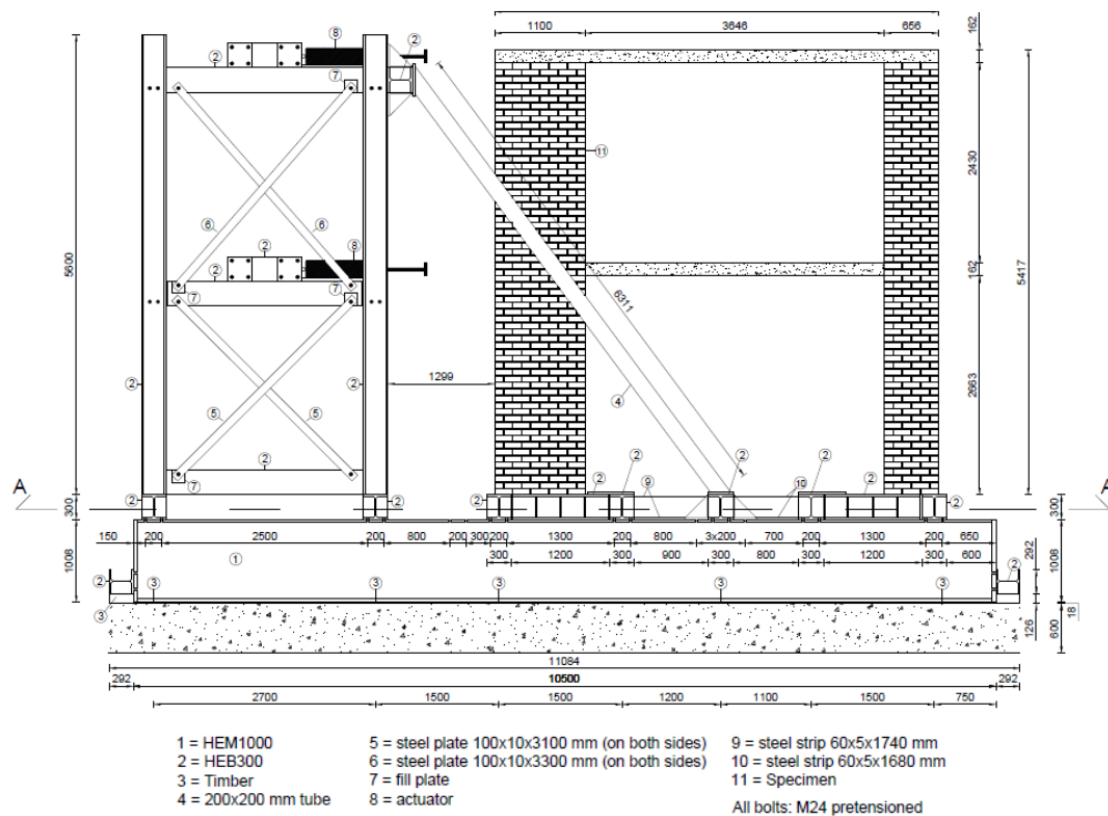


Figure 4.1 – Front view of the test set-up.

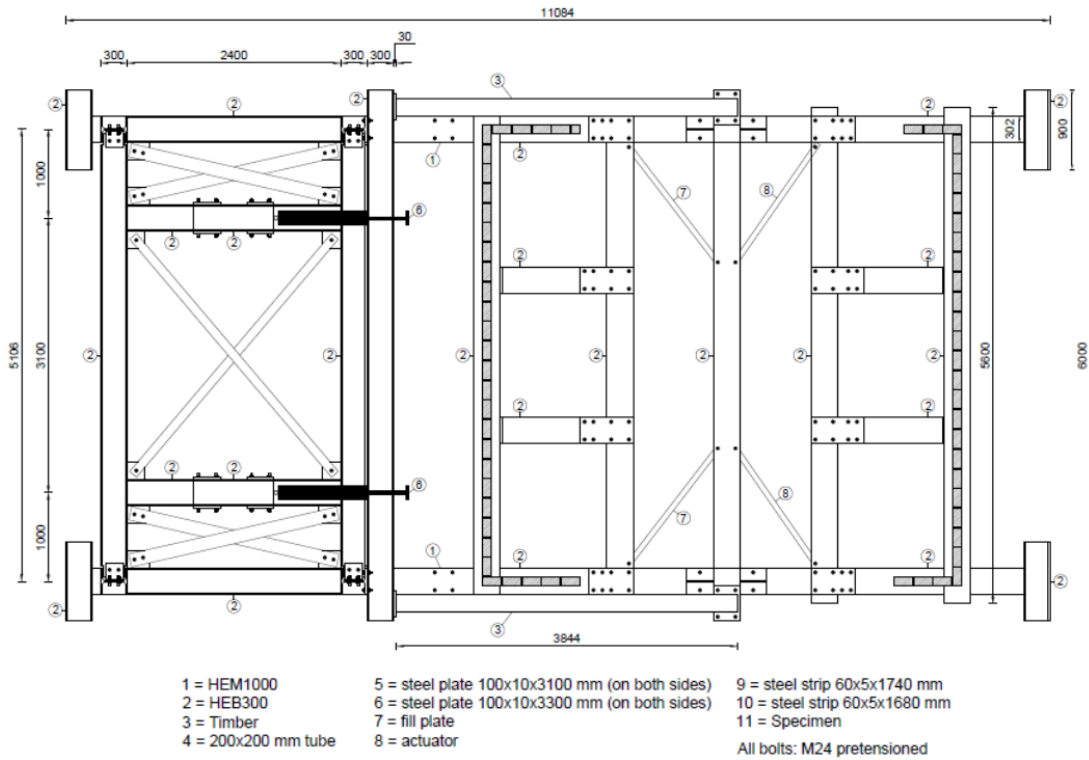
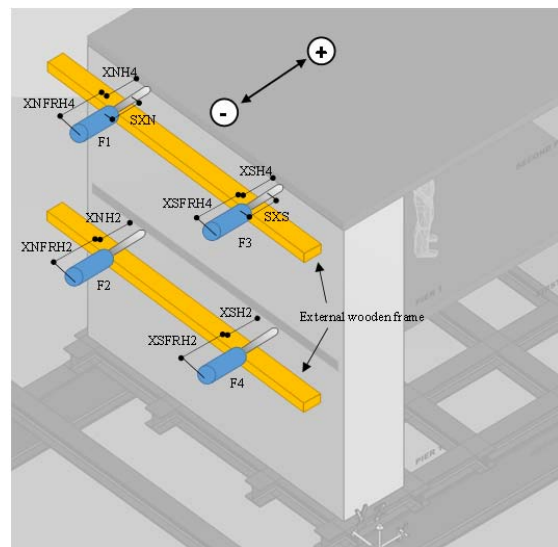


Figure 4.2 – Top view of the test set-up.



(a)

(b)

Figure 4.3 – 3D view of the assembled structures: (a) Nomenclature; (b) Location of actuators and sensors for displacement measurements.

Table 4.1 – Coordinates of the points where the forces and the X-displacement were measured (Origin of the coordinate system in the bottom corner between the west wall and pier P1).

	X	Y	Z
	mm	mm	mm
F1	0	1054	5357.5
F2	0	1054	2759
F3	0	4154	5357.5
F4	0	4154	2759
XSH4	0	770	5357.5
XNH4	0	4435	5357.5
XSH2	0	770	2759
XNH2	0	4435	2759

The assemblage was loaded in displacement control at the second floor level (H4) and simultaneously a ratio of 1:1 was imposed between the forces at the second (H4) and first floor (H2) level. Thanks to the rigid diaphragm, the loading was redistributed to the masonry walls. In order to apply the desired loading scheme four actuators, two per each floor, were used. The actuators were positioned at approximately 1.1 meter inwards from the façades (Figure 4.2, Table 4.1).

To impose the displacement at the second floor level, external potentiometers (SXS and SXN) were adopted for a stable and safe control system. Due to the small play in the hinges of the actuators and the possible limited deformation of the steel reaction frame, the lateral displacements imposed to the loading points at the second floor level, could not be equal to the displacements imposed to the cylinders of the actuators. Consequently, an external wooden frame was used to measure the absolute displacements of the assemblage (XSH4 and XNH4) and of the steel reaction frame (XFRSH4 and XFRSH4) at the location of the actuators. Figure 4.3 shows the overview of the various measurements in a 3D representation of the assemblage. Table 4.1 lists the coordinates of the measurement points.

To impose a relation between the forces at the first and second floor level ($F_1 + F_3 = F_2 + F_4$), the forces in the actuators No. 1 and 3, related to the same imposed displacement, were measured and were coupled with the one at the first floor level (actuators No. 2 and 4) by imposing that:

$$\begin{cases} F_1 = F_2 & \text{on the north side} \\ F_3 = F_4 & \text{on the south side} \end{cases} \quad (1)$$

Considering relative high stiffness of the assemblage with respect to the steel reaction frame, the introduced forces on the northern (F_1, F_2) and southern (F_3, F_4) side of the assembled structure could be different even if limited deformation of the steel reaction frame were measured. Thanks to the high torsional stiffness of the concrete floor and of the transversal walls in the assembled structure, the difference between the introduced forces on the two sides has a limited influence on the stress distribution in the assembled structure along the loading direction. Further details are reported in Appendix A.

The test was performed in three phases named:

- The initial phase (7 December 2015)
- The pre-peak phase (8 December 2015)
- The post-peak phase (15 December 2015)

A total of 21 cycles were applied, each of them composed by 3 runs (Figure 4.4, Table 4.2).

Additionally, at the end of the test a cycle composed by only half a run was applied; afterwards the test was stopped for safety reasons. A run is defined as the time needed to apply the maximum positive and negative target displacement starting and ending at zero. The speed of the imposed lateral deformations

was chosen for every cycle such that the cycle lasted 15 minutes. As a result of the increasing amplitude, the constant cycle time resulted in a deformation velocity increasing per cycle. Table 4.2 lists the maximum and minimum average displacement imposed at the second floor level d_2 for every cycle. They are calculated as the average of the measurements XSH4 and XNH4. Due to the adopted control procedure, the absolute amplitudes in the positive and negative loading direction might not be exactly the same.

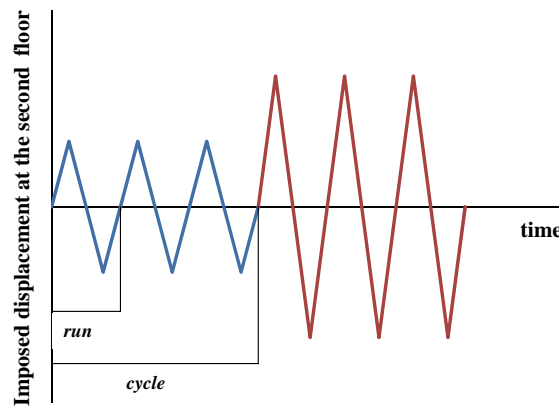


Figure 4.4 – Loading scheme.

Table 4.2 – Applied target displacements for every cycle in the initial, pre- and post-peak phase.

	Cycle	$d_{2,min}$	$d_{2,max}$		Cycle	$d_{2,min}$	$d_{2,max}$		Cycle	$d_{2,min}$	$d_{2,max}$
		mm	mm			mm	mm			mm	mm
Initial phase	1	-0.31	0.25	Pre-peak phase	9	-3.40	3.17	Post-peak phase	15	-21.30	22.16
	2	-0.70	0.61		10	-4.38	4.13		16	-26.89	27.91
	3	-1.14	0.94		11	-6.01	5.80		17	-38.15	39.13
	4	-1.57	1.33		12	-9.07	8.96		18	-49.31	50.62
	5	-2.01	1.73		13	-12.24	12.16		19	-60.13	61.82
	6	-2.45	2.14		14	-15.49	15.43		20	-70.97	73.04
	7	-2.89	2.58						21	-82.31	84.23
	8	-3.36	3.01						22	-92.3*	

*Cycle composed only by half a run

In order to monitor the deformation of the assembled structure during the test, a measuring system was design paying attention to the following points:

- Reaction force measurement for both floors during imposed lateral displacement cycles
- Possible differences in reaction forces in the actuators on north and south side
- Evaluation of the capacity curve in terms of:
 - Relation between imposed cyclic displacement and measured base shear force,
 - Stiffness degradation in the various phases
 - Softening behaviour
 - Hysteretic behaviour and energy dissipation
- Observe the interaction between the in-plane deformation of the piers and the out-of-plane behaviour of the transversal walls.
- Observe the influence of different pier sizes and investigate the mechanism of “active” and “passive” piers.
- Observe crack locations, crack width and crack pattern evolution
- Horizontal and vertical (in-plane) displacements and rotations in piers
- Horizontal and vertical (in-plane) displacements and rotations in transversal walls
- Out-of-plane displacements of both piers and transversal walls
- Deformation of the concrete floors

- Possible crushing of calcium silicate brick masonry near concrete floor support positions
- Behaviour of connection 1st floor - pier (the detail that only takes out-of-plane loads)
- Deformation of the steel frame (test tower and foundation beams)
- Recording of possible unforeseen behaviour for safety measurements

Appendix B reports a complete list of all the instruments. In this report, selected variables are reported that best capture the behaviour of the assembled structure.

4.2 Experimental results

In this section the main experimental results are presented. First, the global behaviour for the structure is presented in terms of capacity curve and crack pattern evolution. Second, considerations on the deformation capacity and drifts of the structure are made.

4.2.1 Global behaviour

The pushover test was performed in three phases named initial, pre-peak and post-peak phase. For each phase a visual inspection of the assemblage was carried out after every cycle to identify the development of the crack pattern. In this section, the results are presented for every phase in terms of capacity curve and description of crack pattern. The crack pattern is reported for every cycle indicating with black lines the existing cracks and with red lines the new observed cracks after the considered cycle. Due to the accessibility of the structure, the inspection were performed mainly in the inside part of the assembled structure; the reported cracks refer to observed cracks in both inside and outside. Please note that although the care taken during the visual inspection, a limitation in identifying the cracks is possible in the initial and pre-peak phase due to the small crack width. Further information can be found also in Appendix D and E.

Figure 4.5 shows the capacity curve of the assembled structure together with the corresponding backbone curve. Due to the different pier width, the behaviour in capacity and ductility are asymmetric. This asymmetric behaviour results directly correlated to the crack pattern evolution (Figure 4.6), as explained in the following paragraphs and in Section 6.2.

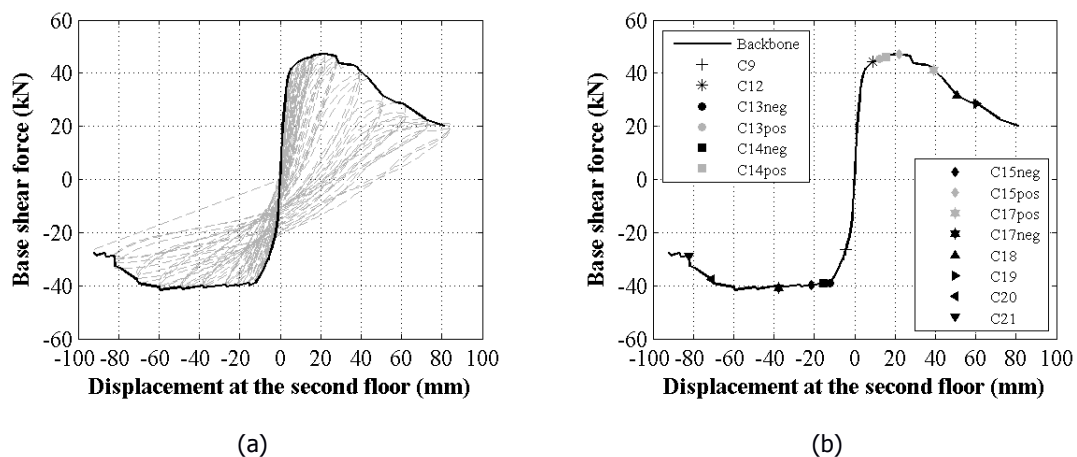


Figure 4.5 – Response of the assembled structure: (a) Capacity curve and corresponding backbone curve; (b) Cycle in correspondence of cracking observations (see also Figure 4.6)

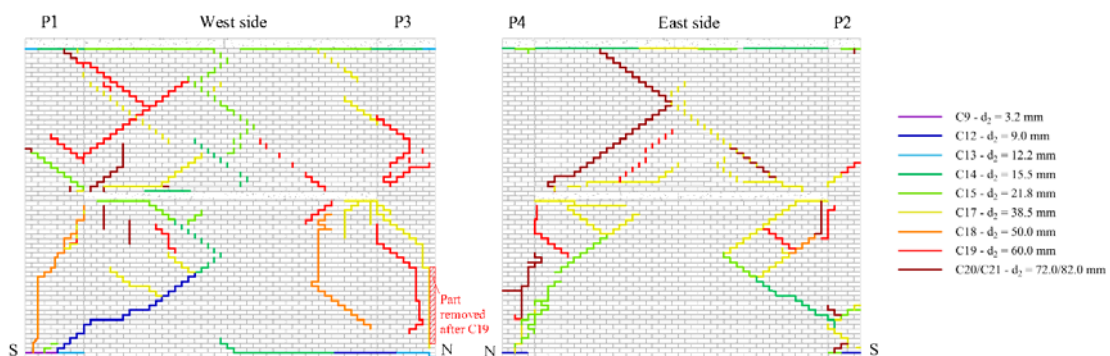


Figure 4.6 – Crack pattern defined on the base of visual inspection (see also Figure 4.5).

Initial phase

The initial phase consisted of the first 8 cycles, in which a maximum displacement of $d_2 = \pm 3.0$ mm is reached. In this phase, the structure primarily shows a linear elastic behaviour. Figure 4.7 shows capacity curve in terms of displacement at the second and first floor level.

By analysing the capacity curve for the first four cycles (Figure 4.8), the initial stiffness of the assembled structure could be estimated up to 15.7 kN/mm (Figure 4.8a). The degradation of the stiffness occurred from cycle 3 ($d_2 = \pm 1.0$ mm).

In this phase, horizontal cracks with a maximum opening of approximately 0.7 mm were measured at the level of the floors (Figure 4.9, Figure 4.10). These cracks could not be detected by the visual inspection until the pre-peak phase (Figure 4.6). Figure 4.9 shows in a schematic way the maximum crack opening measured at the floor-to-wall connections for the western wall and the pier P1, while Figure 4.10 shows the measured crack opening as a function of the displacement at the second floor for both the south-western and south-eastern corner. In both figures, the symmetry lines are used to indicate the geometrical symmetry of the structure. Please note that at the ground floor level the instrument is located between two courses of masonry, being the first one glued on the steel beam foundation. For both the western and eastern wall, the horizontal cracks developed mainly at the second floor level at the corner with the southern façade (WROTO2 and EROTO2 in Figure 4.10c and Figure 4.10d, respectively). Limited cracking was measured for the other wall-to-floor connections on the transversal walls. Horizontal cracks were measured also at the top and bottom of the southern piers P1 (western side) and P2 (eastern side), as reported in Figure 4.10c and Figure 4.10d, respectively. In both cases, the larger horizontal cracks at the floor-to-pier connection were recorded at the second floor level in correspondence of the corner with the transversal wall (SH4R01 and SH4R06) and at the ground floor level in correspondence of the free side of the pier (SH0R04 and SH0R07). Due to the different size of the piers, a larger opening was recorded for the western pier P1.

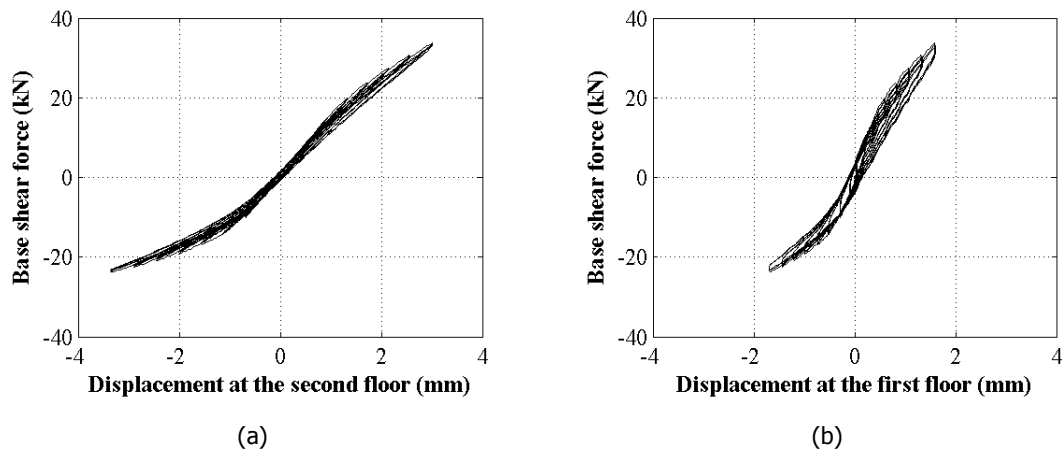


Figure 4.7 – Initial phase: Base shear force vs. displacement at the second (a) and at the first (b) floor level.

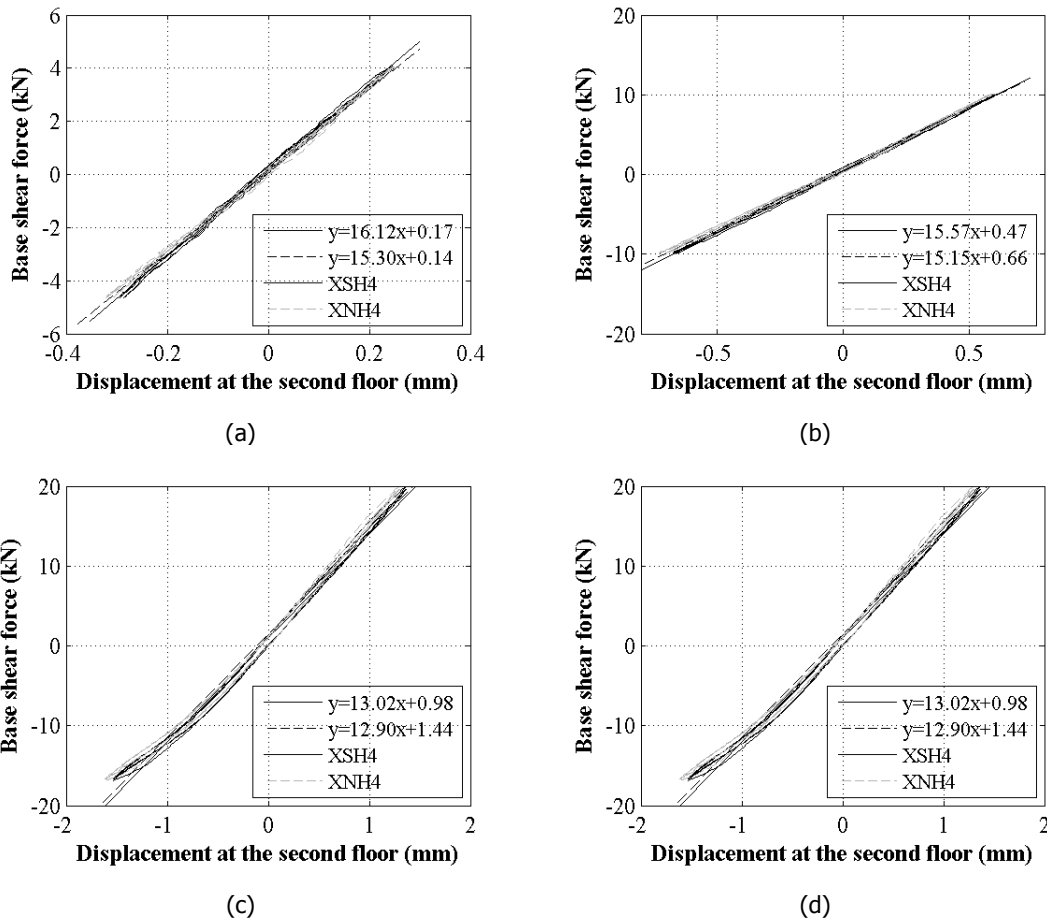


Figure 4.8 – Initial stiffness and its degradation: (a) Cycle 1; (b) Cycle 2; (c) Cycle 3; (d) Cycle 4.

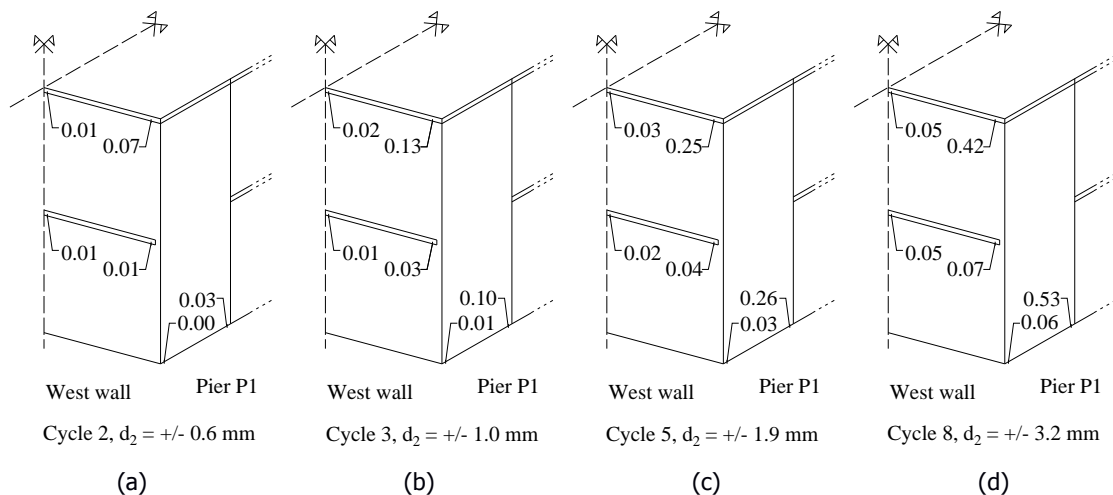


Figure 4.9 – Maximum opening of horizontal cracks at the floor-to-wall connection (western wall) and at the bottom of the pier P1, measured on the outside of the assemblage during the initial phase (unit: mm).

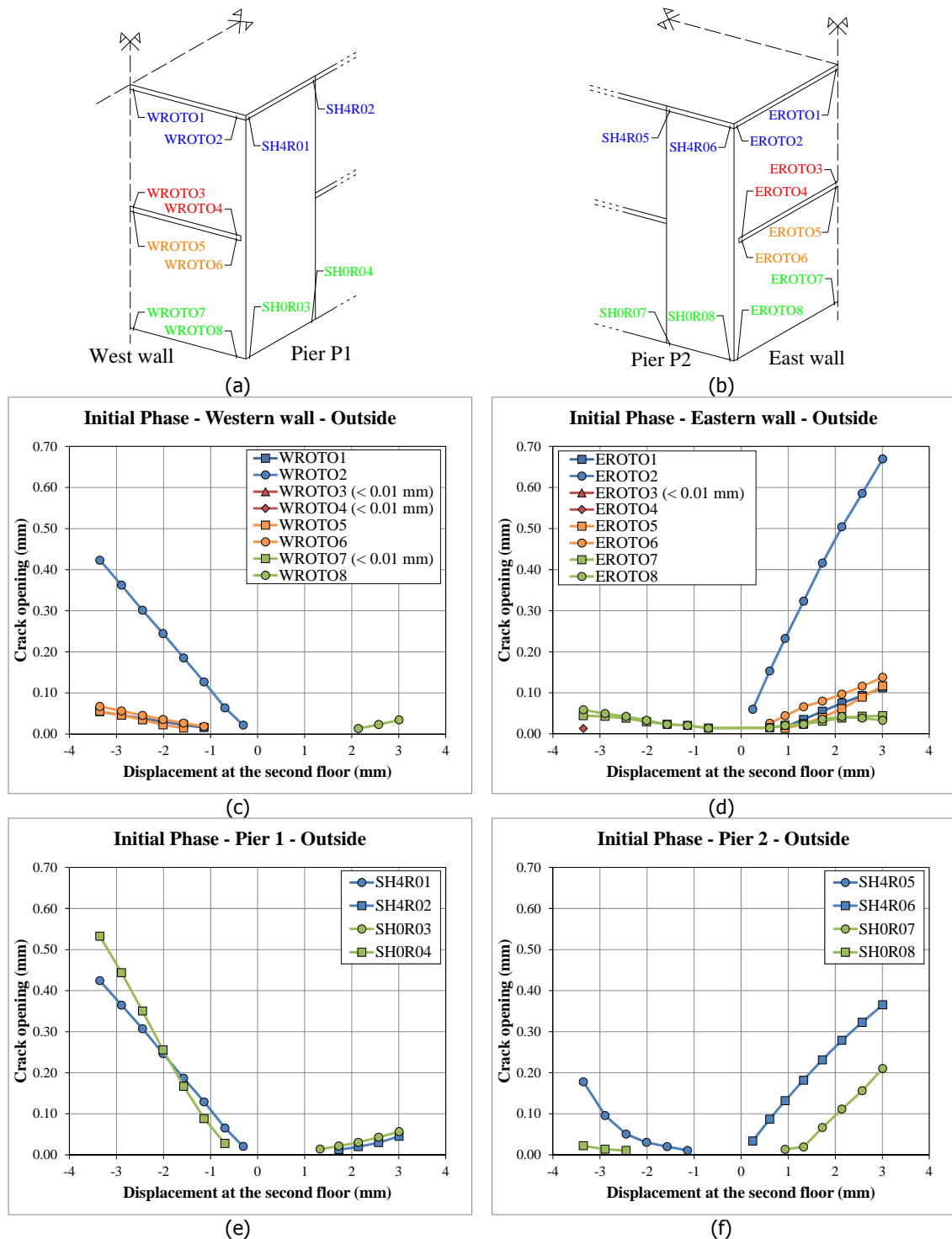


Figure 4.10 – Opening of horizontal cracks recorded during the initial phase: (a)-(b) Location of the sensors; (c)-(d) Cracks between floor and transversal wall on the western and eastern side; (e)-(f) Cracks at the bottom of the southern piers (P1 and 2). Crack opening lower than 0.01 mm have been not reported in the graphs for clarity sake.

Pre-peak phase

In the pre-peak phase, cycle 9 to 14 were executed to reach a maximum displacement of $d_2 = \pm 15.5$ mm. Figure 4.11 shows the capacity curve in terms of displacement at the second and first floor level. By observing the capacity curves, it is possible to note that the damage mechanism induces a dissipation of the energy. Additionally, an accumulation of inelastic deformation at zero force for positive loading is observed. This phenomenon might be related to the different sliding/friction behaviour in the cracks for the two loading direction.

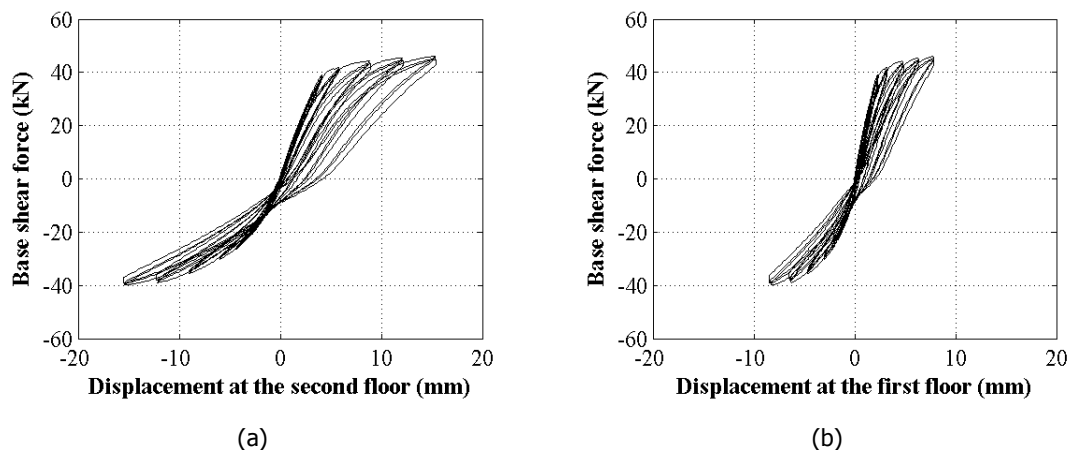


Figure 4.11 – Pre-peak phase: Base shear force vs. displacement at the second (a) and at the first (b) floor level.

In this phase, the horizontal cracks in the piers at the ground floor level, which were previously measured in the initial phase (Figure 4.10), were detected both by the measurements (Figure 4.12) and during the visual inspection. During cycle 9 ($d_2 = \pm 3.2$ mm), the first crack visible at necked eyed was observed at the bottom of pier P1 (Figure 4.13) on the free side of the pier. During cycle 12 ($d_2 = \pm 9.0$ mm), all the other piers showed a similar crack pattern (Figure 4.14). Due to the limited thickness of the glue at the free bottom side of pier P3, the horizontal crack undesirable occurred in the glue rather than in the first mortar joint (Figure 4.15d, Figure E.7). This crack only developed for a length of half a brick (Figure 4.15b), thus the mechanism can be considered locally and with a limited impact on the structural behaviour. Consequently the measurement of sensor NH0R15 have been excluded (Figure 4.12e) and an additional sensor (NH0R15A) has been mounted between the steel beam foundation and the first course of brick prior to the post-peak phase.

The horizontal cracks at the first and second floor level were detected during the visual inspection only after cycle 13 ($d_2 = \pm 12.2$ mm, Figure 4.15 and Figure 4.16) and cycle 14 ($d_2 = \pm 15.5$ mm, Figure 4.17 and Figure 4.18). However, by analysing the response of the sensors in Figure 4.12, it is possible to note that for the majority of the piers horizontal cracks with similar crack opening are observed both at the ground and second floor level. This difference can be input to the difference in accessibility of the two locations.

During the pre-peak phase the first diagonal cracks appeared on the transversal walls. After cycle 12 ($d_2 = \pm 9.0$ mm, Figure 4.14), a diagonal crack was observed on the western wall. This crack developed first at the bottom of pier P1, as an extension of the horizontal crack previously formed, and it run around the corner to finally develop as a diagonal stepwise crack on the southern side of the western wall. After cycle 14 ($d_2 = \pm 15.5$ mm, Figure 4.17), a similar crack was observed on the eastern wall at the corner with the southern pier P2. Cracks in some head joint were observed at the central part of the western wall at the first floor (Figure 4.17).

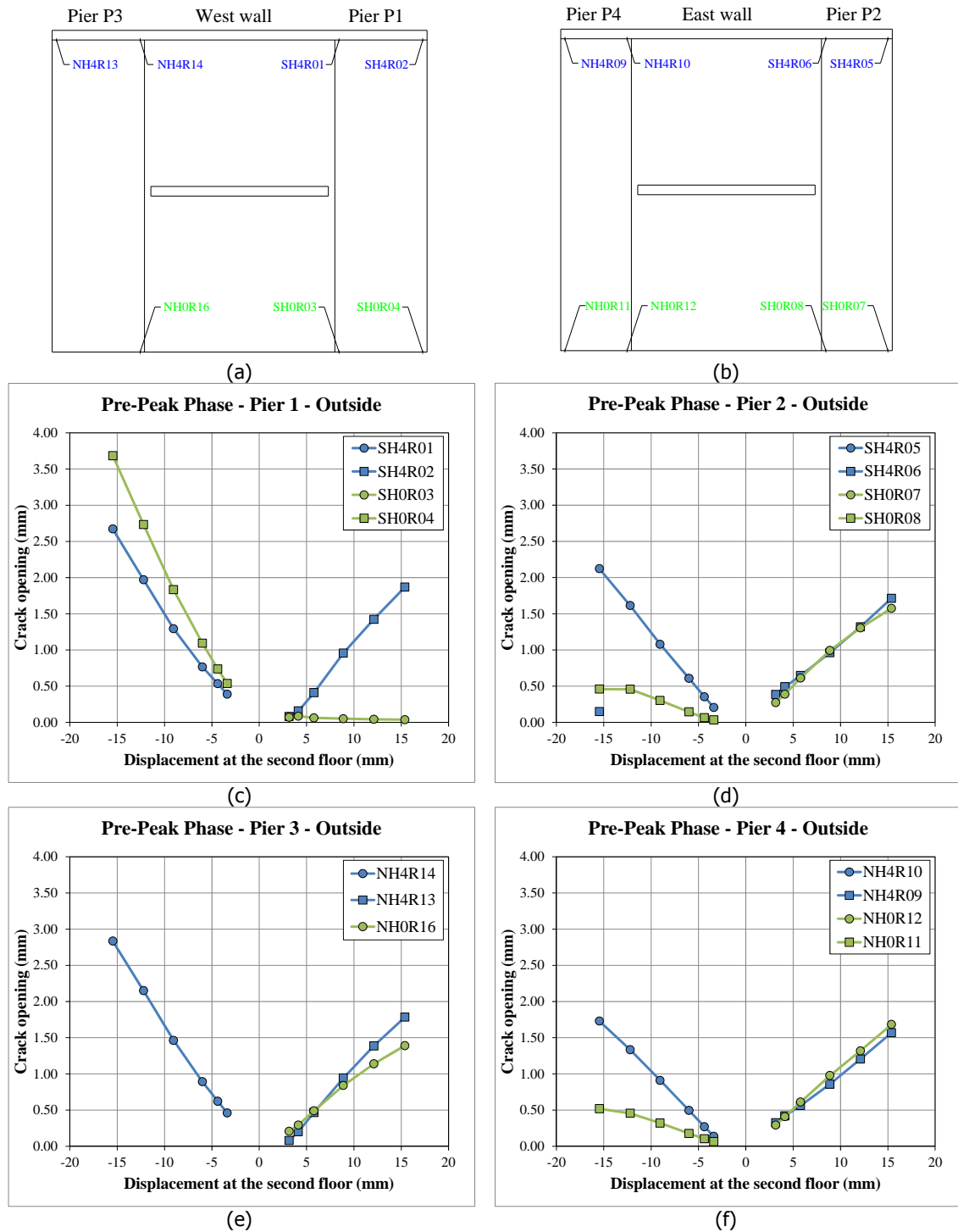
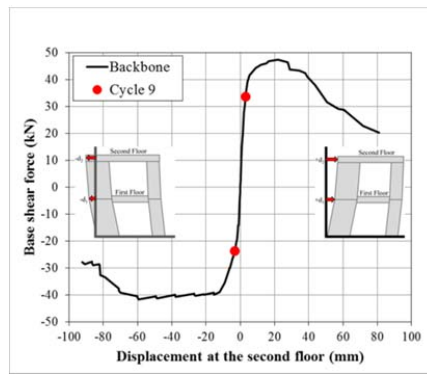
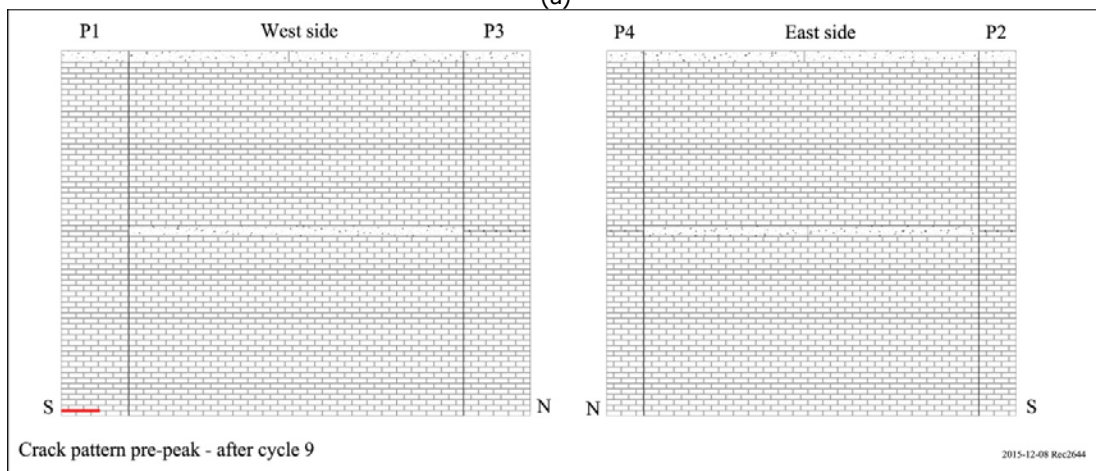


Figure 4.12 – Opening of horizontal cracks recorded during the pre-peak phase: (a)-(b) Location of the sensors; (c) Pier P1; (b) Pier P2; (e) Pier P3; (f) Pier P4. Crack opening lower than 0.01 mm have been not reported in the graphs for clarity sake.



(a)

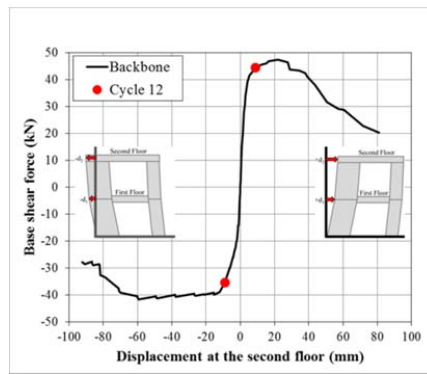


(b)

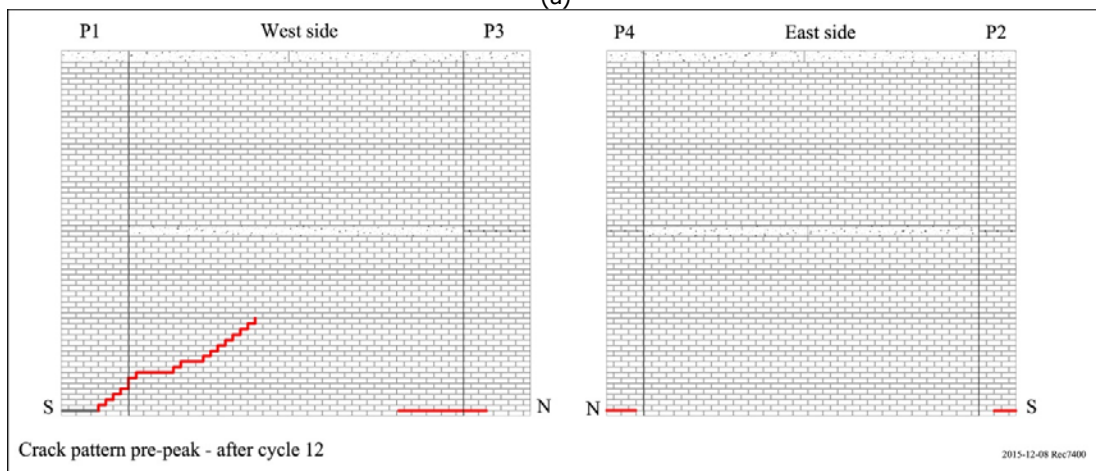


(c)

Figure 4.13 – Visual inspection after **cycle 9**: (a) Backbone curve; (b) Crack pattern (existing cracks in black, new cracks in red); (c) Crack at the bottom of pier P1 (1_C9-GF-P1). See also Figure E.2.



(a)



(b)

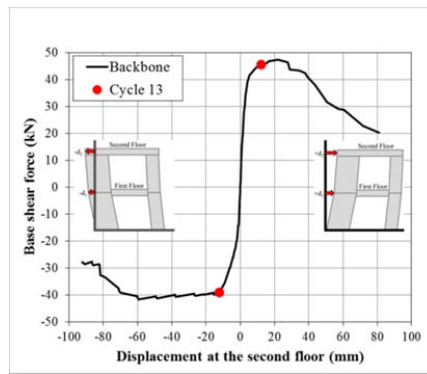


(c)

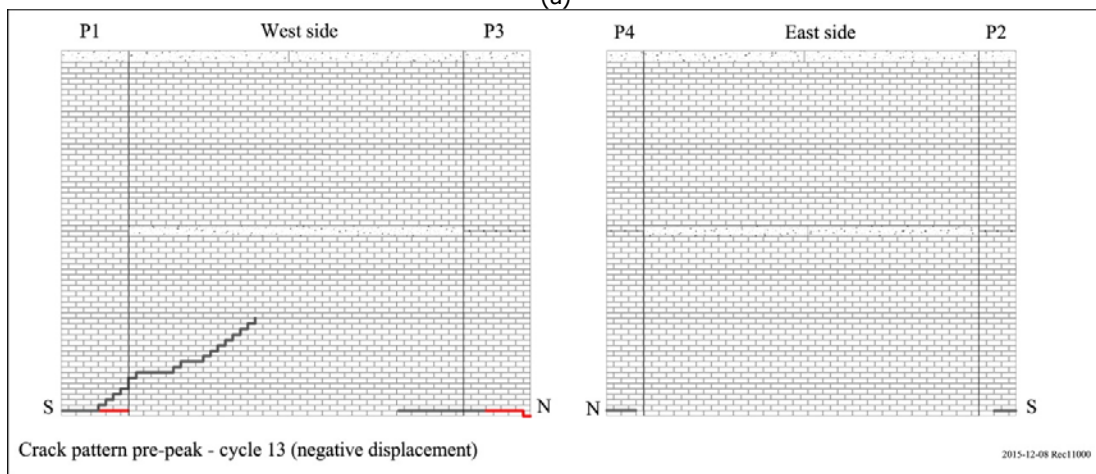


(d)

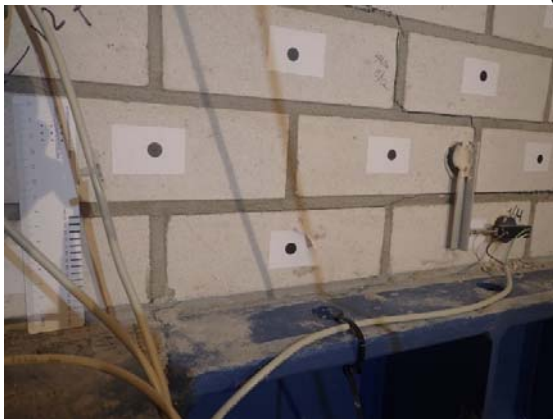
Figure 4.14 – Visual inspection after cycle 12: (a) Backbone curve; (b) Crack pattern (existing cracks in black, new cracks in red); (c) Crack at the bottom of pier P1 (2_C12-GF-P1); (d) Crack at the bottom of pier P2 (4_C12-GF-P1). See also from Figure E.3 to Figure E.5.



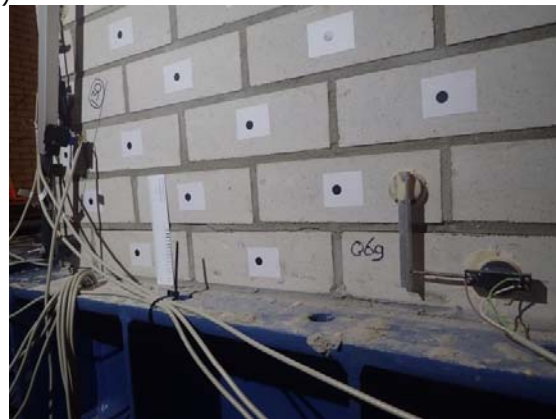
(a)



(b)

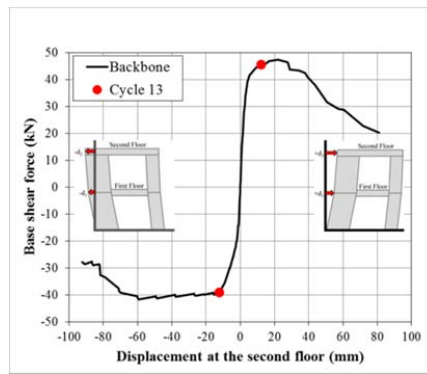


(c)

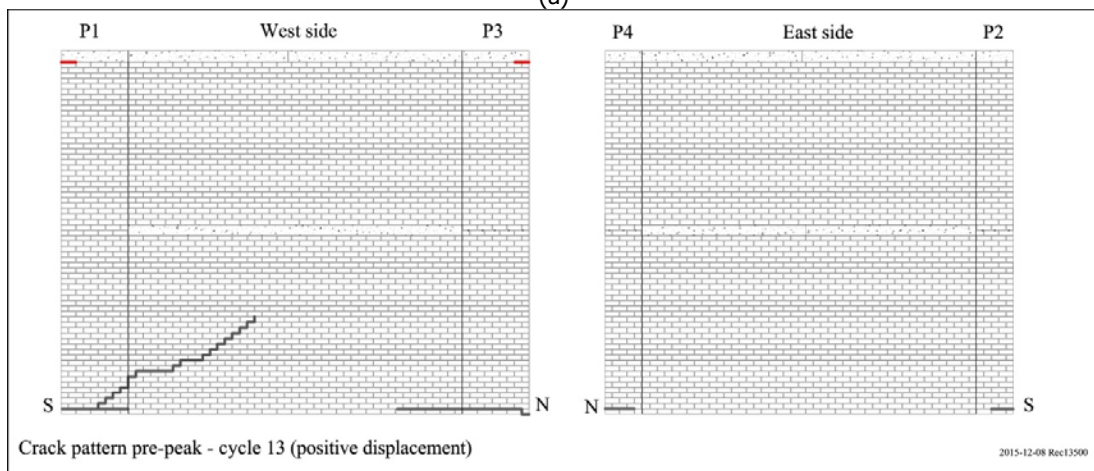


(d)

Figure 4.15 – Visual inspection after cycle 13 (last negative displacement): (a) Backbone curve; (b) Crack pattern (existing cracks in black, new cracks in red); (c) Crack at the bottom of pier P1 (7_C13-GF-P1); (d) Crack at the bottom of pier P3 (8_C13-GF-P3). See also Figure E.6.

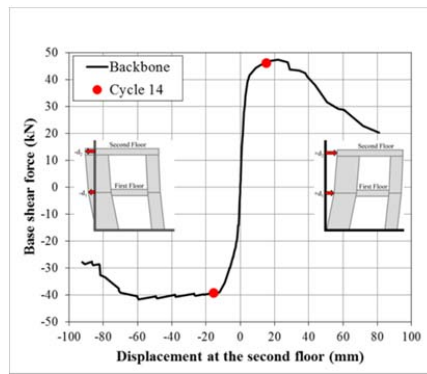


(a)

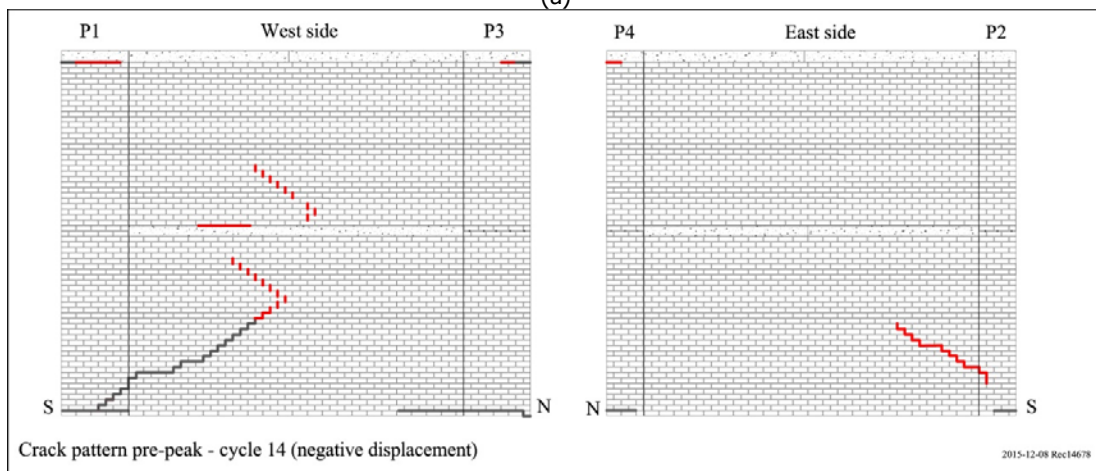


(b)

Figure 4.16 – Visual inspection after **cycle 13 (last positive displacement)**: (a) Backbone curve; (b) Crack pattern (existing cracks in black, new cracks in red)



(a)



(b)

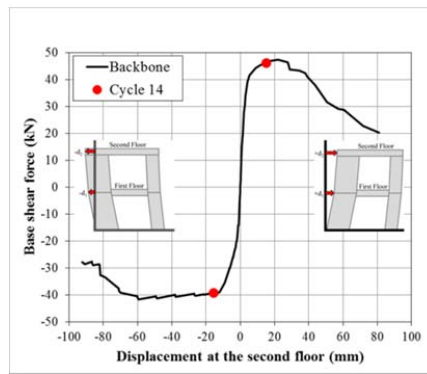


(c)

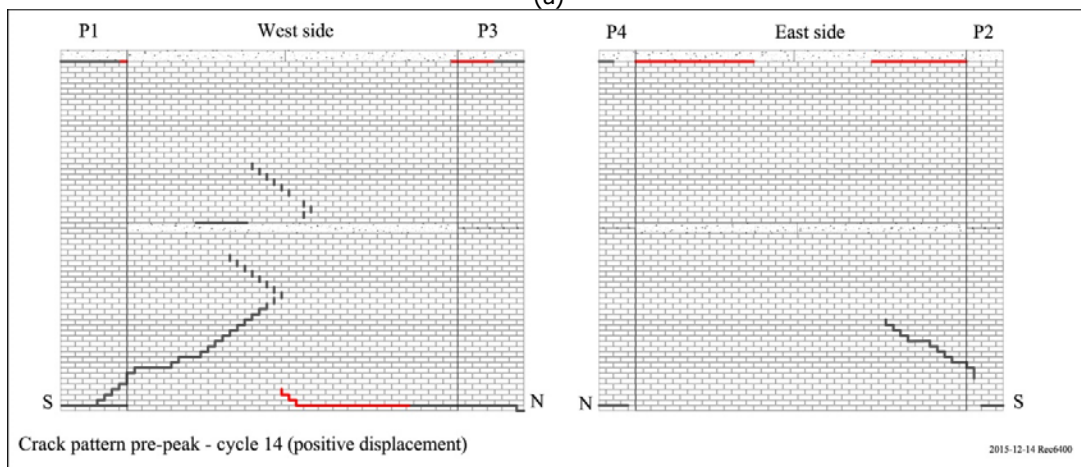


(d)

Figure 4.17 – Visual inspection after **cycle 14 (last negative displacement)**: (a) Backbone curve; (b) Crack pattern (existing cracks in black, new cracks in red); (c) Crack between second floor slab and pier P3 (15_C14-FF-P3); (d) Crack in pier P2 (12_C14-GF-P2). See also from Figure E.7 to Figure E.10.



(a)



(b)



(c)

Figure 4.18 – Visual inspection after **cycle 14 (last positive displacement)**: (a) Backbone curve; (b) Crack pattern (existing cracks in black, new cracks in red); (c) Diagonal cracks on west wall (outside) at the first floor (16_C14-FF-W). See also Figure E.11.

Post-peak phase

In the post-peak phase, cycle 15 to 21 were executed to reach a maximum displacement of $d_2 = \pm 82.0$ mm. Afterwards, the assemblage was subject to a half of a run imposing a negative displacement of $d_2 = -92.0$ mm; due to safety issue the test was stopped. Figure 4.19 shows the capacity curve in terms of displacement at the second and first floor level. By observing the capacity curves, it is possible to note that the damage mechanism induces a dissipation of the energy. Additionally, an accumulation of inelastic deformation at zero force for positive loading is observed. This phenomenon might be related to the different sliding/friction behaviour in the cracks for the two loading direction.

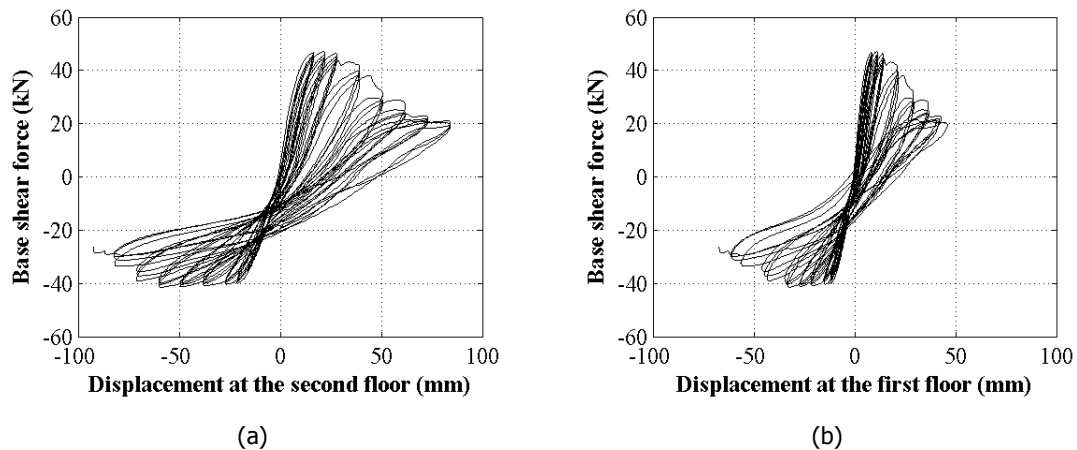


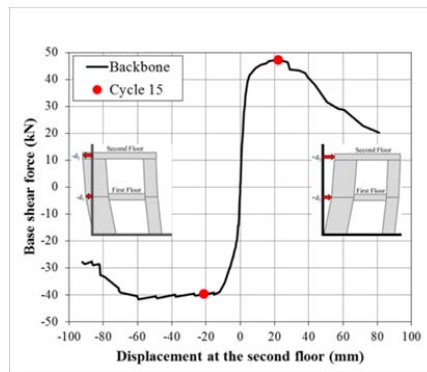
Figure 4.19 – Post-peak phase: Base shear force versus displacement at the second floor level (a) and at the first (b) floor level.

The structure presented an asymmetrical behaviour for loading in the positive (from west to east side) and negative (from east to west side) direction. The maximum capacity was first reached for positive displacements. During cycle 15 ($d_2 = \pm 21.8$ mm), the maximum base shear force of 47.3 kN was reached for positive displacement, while for negative displacement approximately 97% of the maximum capacity was reached. During this cycle, the previously observed horizontal and diagonal cracks on the transversal walls further extended (Figure 4.18, Figure 4.20, Figure 4.21).

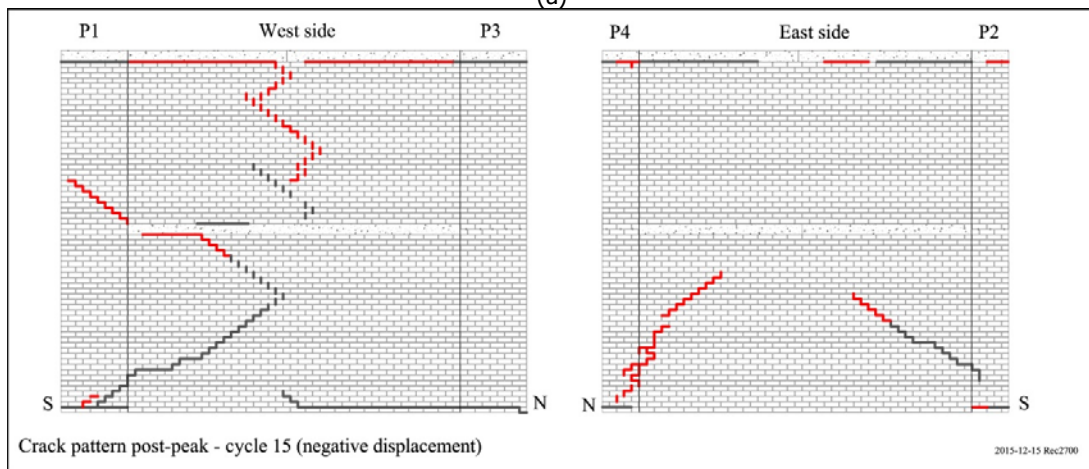
After the peak, the capacity and stiffness substantially reduced for positive displacements. This phenomenon was mainly governed by the diagonal/vertical cracks occurring first in pier P3 during cycle 17 ($d_2 = \pm 38.5$ mm, Figure 4.22) and subsequently in pier P1 during cycle 18 ($d_2 = \pm 50.0$ mm, Figure 4.24). Due to the extensive cracking of these piers, part of pier P3 was removed for safety reasons after cycle 19 ($d_2 = \pm 60.0$ mm, Figure 4.25). For negative displacements, the maximum base shear force of 41.6 kN was reached in cycle 19 for displacement of $d_2 = -60$ mm. This event corresponded to the formation of a secondary diagonal/vertical crack in pier P3 (Figure 4.25).

During this phase, the out-of-plane cracks on the transversal walls further developed, by forming the yield line envelope typical of the two-way out-of-plane bending mechanism. At the ground floor, the diagonal cracks, which are stepwise cracks, developed at the same time in the bed and head joints. On the contrary, at the first floor the stepwise cracks developed first in the head joints and subsequently in the bed joint (e.g. compare Figure 4.22 with Figure 4.26).

Extensive cracking in the narrow piers P2 and P4 only occurred during cycle 19 ($d_2 = \pm 60.0$ mm, Figure 4.25). Prior to this cycle, the narrow piers only presented limited damage at the bottom and in the floor-to-pier connection at the second floor level. During cycle 19, both pier P2 and P4 show vertical cracks at the ground floor in correspondence of the interlocked connection with the transversal wall. Its crack width reached 20 mm for the northern pier P4 during cycle 20 (GF-E in Table 4.3 and in Figure 4.27). After cycle 20 ($d_2 = \pm 72.0$ mm, Figure 4.26), a vertical crack formed within the central part of the northern pier P4 at the ground floor.



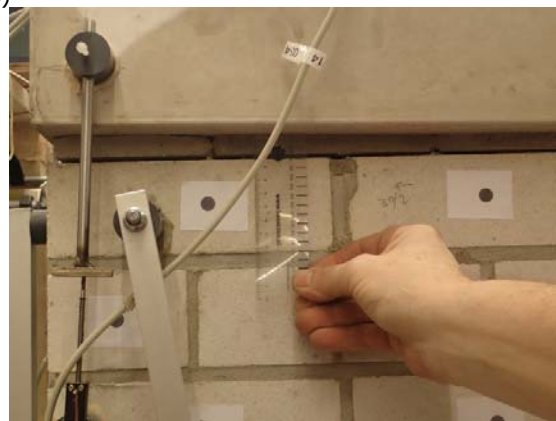
(a)



(b)

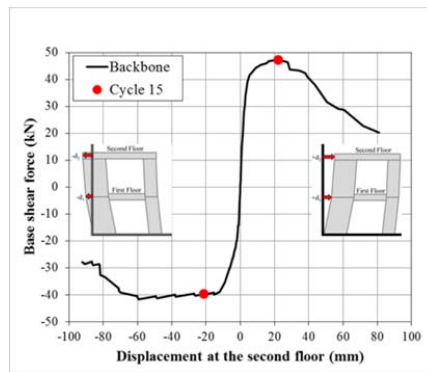


(c)

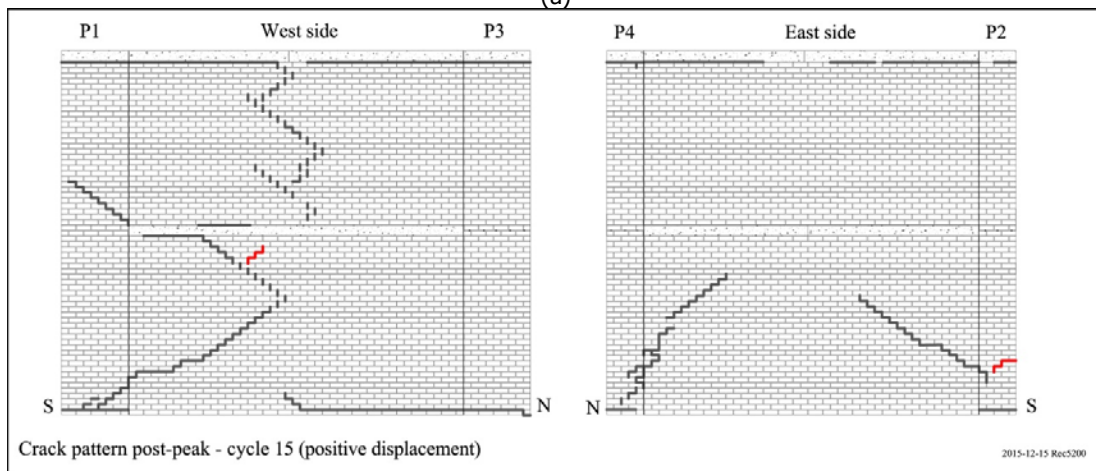


(d)

Figure 4.20 – Visual inspection after **cycle 15 (last negative displacement)**: (a) Backbone curve; (b) Crack pattern (existing cracks in black, new cracks in red); (c) Crack between first floor slab and west wall at corner with pier P1 (18_C15-GF-WP1); (d) Crack between second floor slab and pier P1 (outside) (23_C15-FF-P1). See also from Figure E.12 to Figure E.16.



(a)



(b)

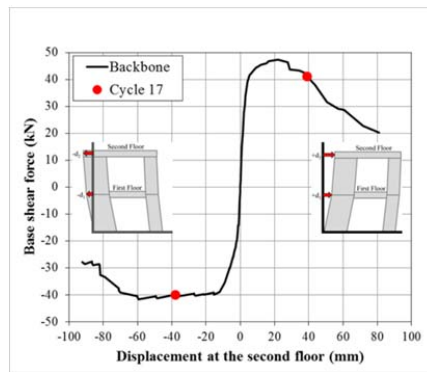


(c)

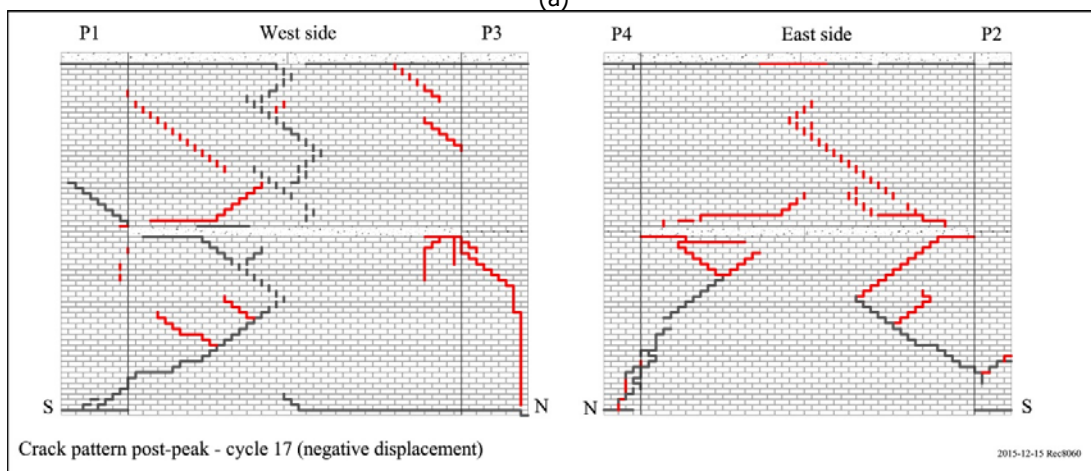


(d)

Figure 4.21 – Visual inspection after **cycle 15 (last positive displacement)**: (a) Backbone curve; (b) Crack pattern (existing cracks in black, new cracks in red); (c) Crack at the corner between west wall and pier P1 (30_C14-GF-P1W); (d) Crack between second floor slab pier P2 (28_C15-FF-P2). See also from Figure E.17 to Figure E.18.



(a)



(b)

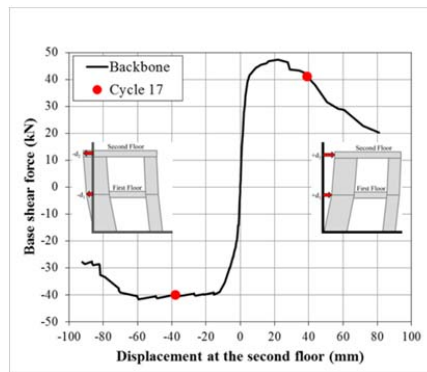


(c)

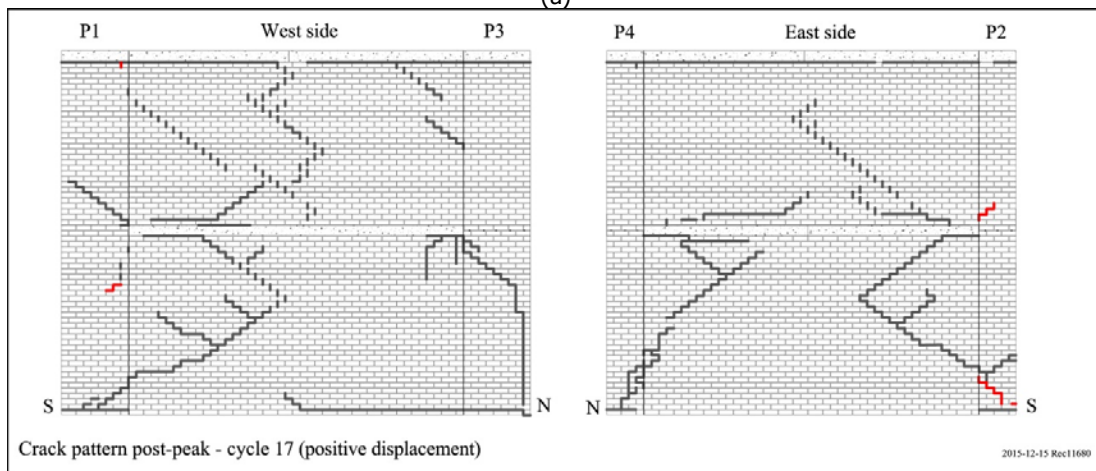


(d)

Figure 4.22 – Visual inspection after cycle 17 (last negative displacement): (a) Backbone curve; (b) Crack pattern (existing cracks in black, new cracks in red); (c) Crack on pier P3 at the ground floor (31_C17-GF-P3); (d) Cracks on pier P4 at the corner with east wall (35_C17_GF_P4E). See also from Figure E.19 to Figure E.24.



(a)



(b)

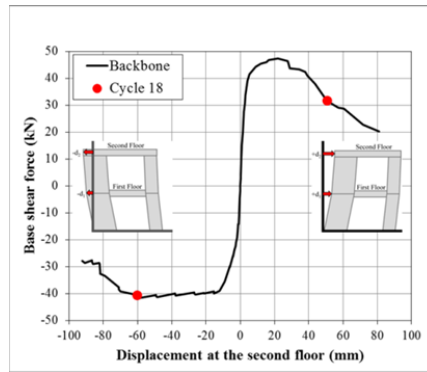


(c)

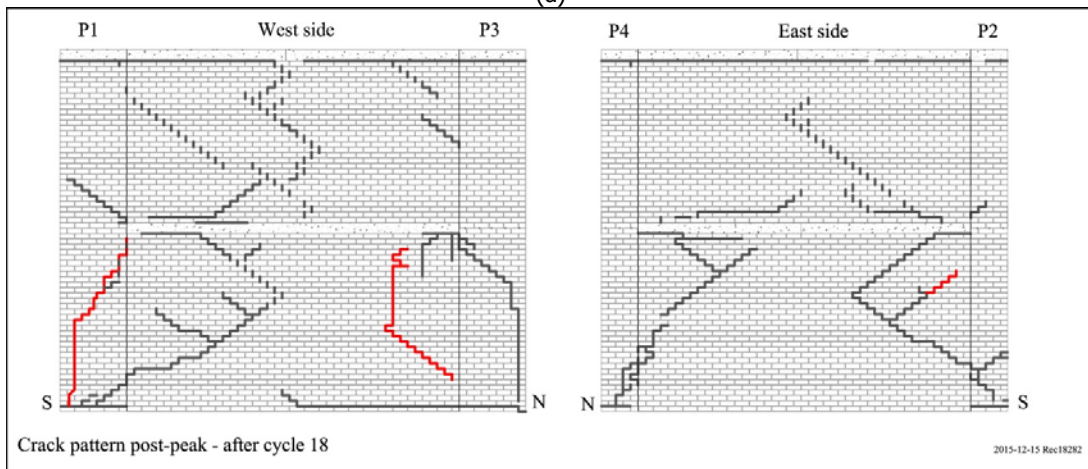


(d)

Figure 4.23 – Visual inspection after **cycle 17 (last positive displacement)**: (a) Backbone curve; (b) Crack pattern (existing cracks in black, new cracks in red); (c) Diagonal crack at the bottom of pier P2 at the ground floor (41_C17-GF-P2); (d) Crack on pier P3 at the side with west wall (42_C17-GF-P3). See also Figure E.25.



(a)



(b)

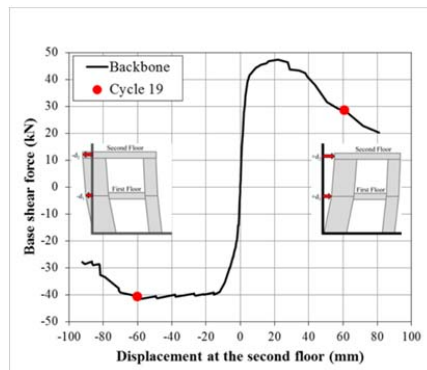


(c)

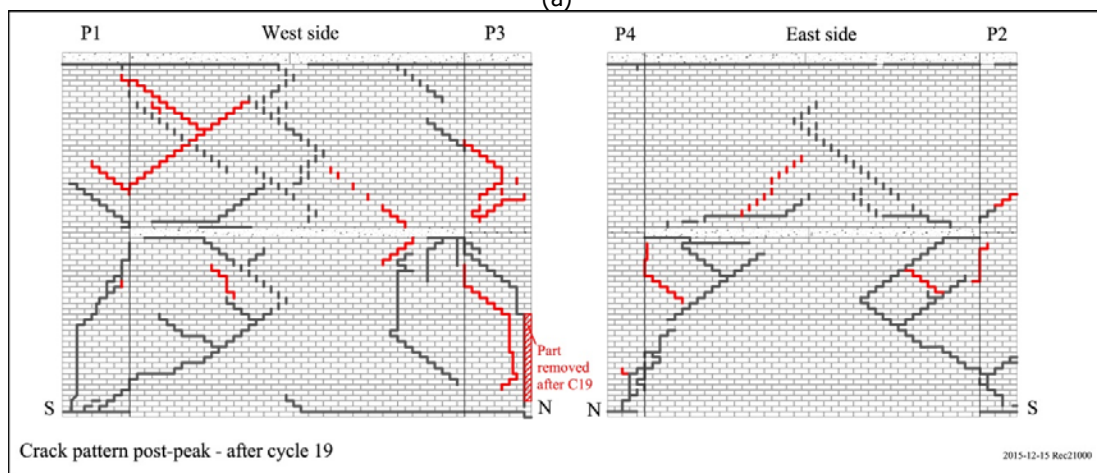


(d)

Figure 4.24 – Visual inspection after cycle 18: (a) Backbone curve; (b) Crack pattern (existing cracks in black, new cracks in red); (c) Diagonal crack on pier P1 at the ground floor (a): Outside (43_C18-GF-P1); (d) Diagonal crack on pier P3 at the ground floor (outside): (a) Bottom part (45_C18-GF-P3). See also from Figure E.27 to Figure E.29.



(a)



(b)

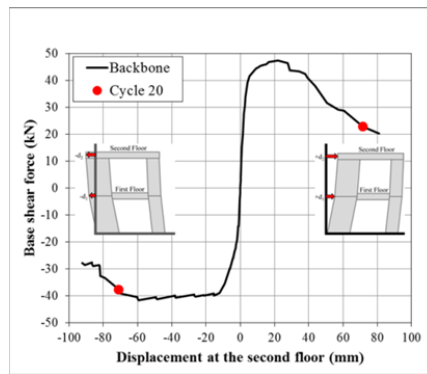


(c)

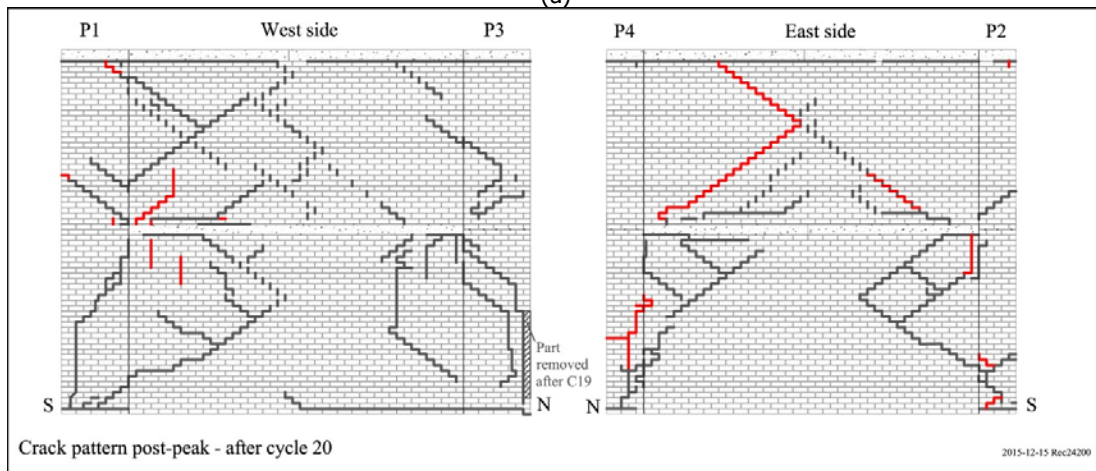


(d)

Figure 4.25 – Visual inspection after cycle 19: (a) Backbone curve; (b) Crack pattern (existing cracks in black, new cracks in red); (c) Upper part of the diagonal/vertical crack on pier P3 at the ground floor (54_C19-GF-P3); (d) Central part of the diagonal/vertical on pier P1 at ground floor (49_C19-GF-P1). See also from Figure E.31 to Figure E.34.



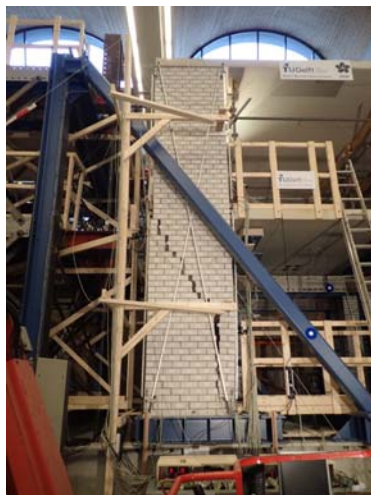
(a)



Crack pattern post-peak - after cycle 20

2015-12-15 Rec24200

(b)



(c)



(d)

Figure 4.26 – Visual inspection after cycle 20: (a) Backbone curve; (b) Crack pattern (existing cracks in black, new cracks in red); (c) Diagonal/vertical crack on pier P1 (57_C20-P1); (d) Crack on pier P4 (60_C20-GF-P4). See also from Figure E.36 to Figure E.39.

Table 4.3 lists the crack width measured at selected locations (Figure 4.27).

Table 4.3 – Crack width at selected locations measured at the ground floor.

No. cycle	Crack width (mm)						Figure
	GF-A	GF-B	GF-C	GF-D	GF-E	GF-F	
17	12	5	2	1	-	-	Figure E.26
18	21	6	5	2	-	-	Figure E.30
19	Part removed	6	12	-	-	-	Figure E.35
20	Part removed	6	15	8	20	20	Figure E.38

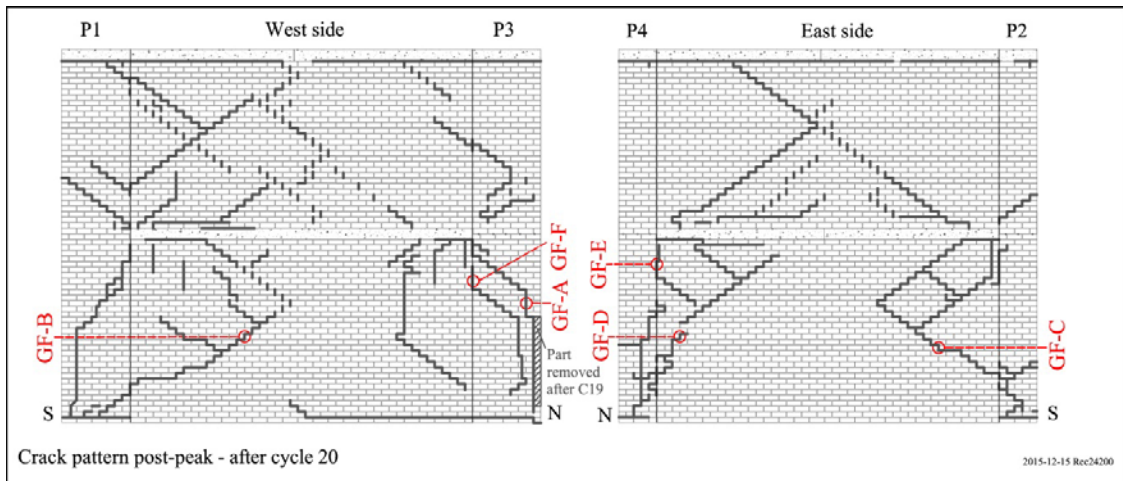


Figure 4.27 – Monitoring points for the crack width: (a) West wall; (b) East wall.

4.2.2 Deformations and drifts

In this section, the deformation of the assembled structure is analysed in terms of displacements and drifts of the two stories.

Figure 4.28a reports the behaviour of the structure in terms of floor displacements. The ratio of the floors' displacement was ranging between 0.2 and 0.5 in the initial phase; afterwards a constant trend was observed in the pre- and post-peak phase. Similar values of the ratio between the floor's displacements were observed for the loading in the positive and negative direction, with the exception of the last two cycles. In these cycles, the first floor level showed larger displacement for negative loading than for positive loading (Figure 4.28d). This can be correlated to the opening/closing mechanism of the cracks in the western piers P1 and P3 (Figure 4.25c, Figure 4.25d and Figure 4.26). These cracks are only located at the ground floor and they developed around the connection of the piers with the western wall. If the assemblage is subjected to negative displacements, these cracks are open and allow for large displacement of the transversal walls, thus of the first floor level. On the contrary, if positive displacement is applied to the assemblage, these cracks are closed limiting the displacement of the floor.

Figure 4.29 reports the behaviour of the structure in terms of drifts. They are calculated as the ratio between the relative floor displacement and the interstorey height, which is 2.7 and 2.6 m for the first and second floor level, respectively. In the initial and pre-peak phase, both the first and second floor show similar drift values. At the end of the post-peak phase, a difference is observed, for both floor levels, between the drifts values obtained for negative and positive loading. This difference can be correlated to the extensive damage within the western piers (P1 and P3). A maximum drift of +1.6/-2.4 % was reached at the first floor level, while the second floor showed a drift of +1.6/-1.0 %.

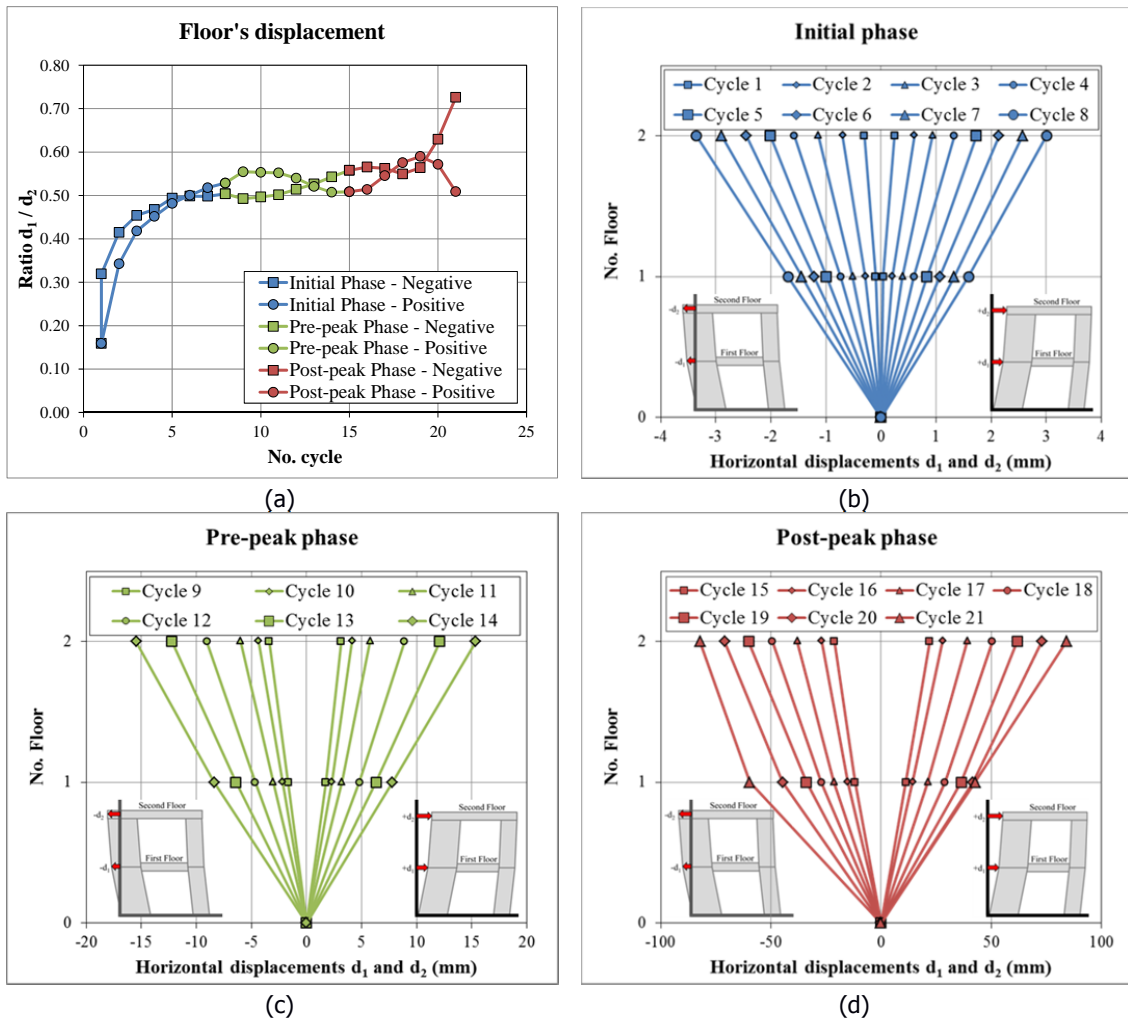


Figure 4.28 – (a) Ratio between first and second floor displacement; (b)-(d) Minimum and maximum horizontal displacements per cycle.

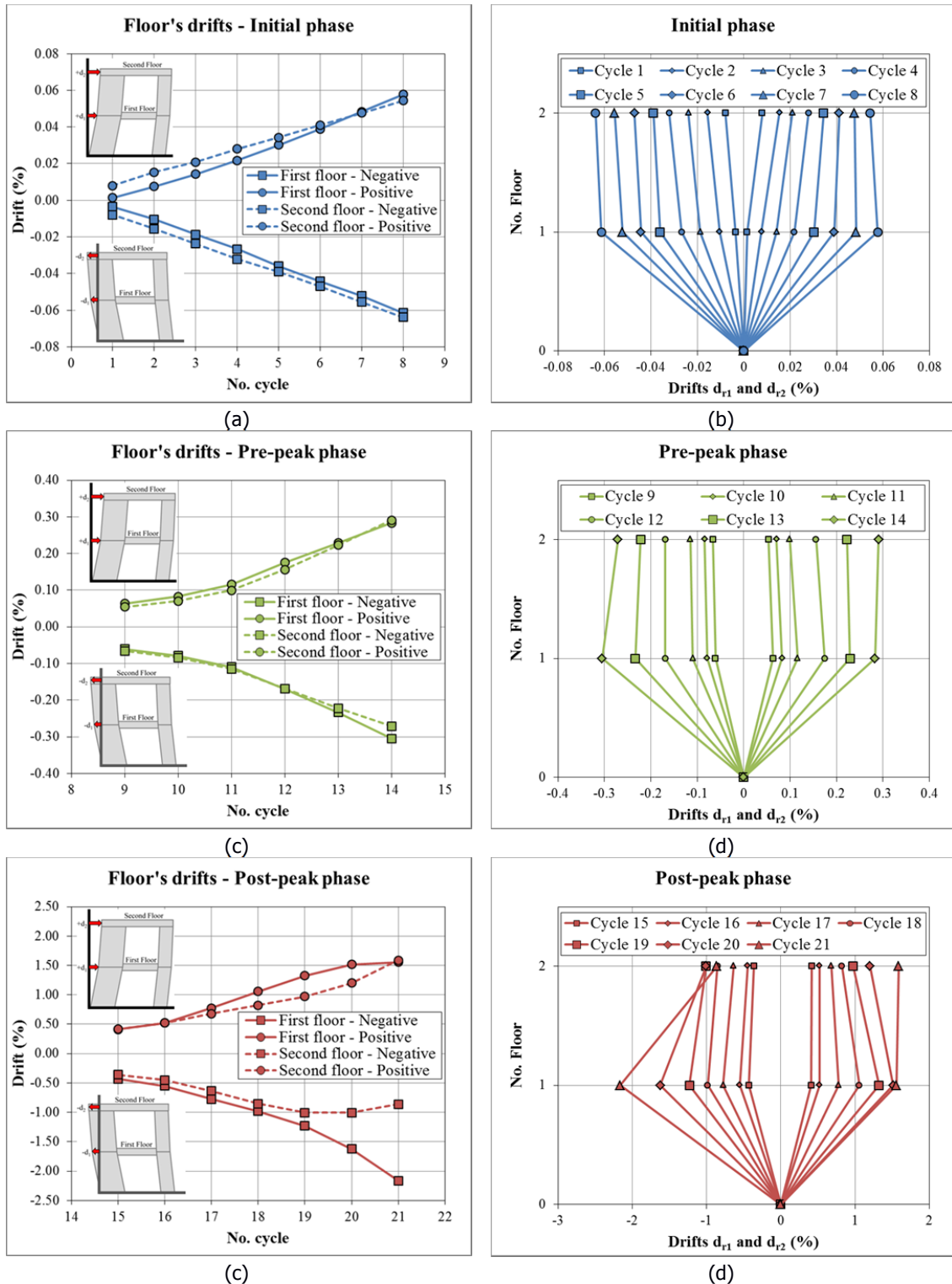


Figure 4.29 – Floors' drifts (calculated with $H_{1st\ floor} = 2753\ mm$, $H_{2nd\ floor} = 2605\ mm$): (a)–(b) Initial phase; (c)–(d) Pre-peak phase; (e)–(f) Post-peak phase.

5 Dynamic identification test

5.1 Testing protocol

The dynamic identification is based on the hammer impact method which is a non-destructive identification method. This method works with relatively low input energy of the impact hammer compared to other conventional techniques, i.e. the use of the shaking table. Despite the fact that the energy input is relatively low, the structure can be excited globally provided that the connections between the various parts of the structure are monolithic, i.e. the connections are such that the energy flow between the various parts can be ensured. In fact, the hammer impact generates waves which are guided through the structure. The reflection of those waves at the various boundaries of the structure forms a standing wave pattern; the latter being the modal shapes (the formed standing wave patterns) of the system under investigation.

The dynamic properties normally identified are the natural frequencies, the modal shapes and the modal damping; here the focus was on the first and second elements only. The main advantages of using impact techniques for dynamic identification can be summarized as follows. First, the exerted force is analogous to an impulse, meaning that the energy input into the system is spread over a wide range of frequencies. This, generally, simplifies the identification process since it excludes the identification of spurious modes related to the excitation only. Second, the experiment itself provides great flexibility due to the fact that the resources required can be mobilized and demobilized with minimal effort, i.e. the source can easily be moved to various locations of interest.

At three different stages of the quasi-static cyclic pushover test, thus at the different damage states of the assembled structure, a dynamic identification test was executed. Prior to each dynamic identification test, the assembled structure was unloaded and the actuators were disconnected. The impact tests were performed at the following moments of the pushover test:

- **Test 1:** Before the cyclic pushover test started. The assembled structure was undamaged.
- **Test 2:** At the end of the initial phase (after cycle 8), at which a reduction of the stiffness was observed from the capacity curve, but almost no cracks could visually be observed.
- **Test 3:** At the end of the pre-peak phase (after cycle 14), at which a reduction of the stiffness was observed from the capacity curve and also significant cracking could be visually observed.

Figure 5.1 show the backbone curve and the positions of each dynamic identification test.

During each impact tests 5 measurements to determine a specific eigenmode were made. Of the studied modes the following first natural frequencies were determined:

- The first natural frequency in the X-direction of the structure. This is the direction in which the structure is loaded in the quasi-static cyclic test. The position of impact is in the middle of second floor on the east wall as indicated as X2 in Figure 5.2.
- The first natural frequency in the Z-direction (vertical direction) of the first floor. The position of impact is in the centre of the first floor as indicated as Z1 in Figure 5.2.
- The first natural frequency in the Z-direction (vertical direction) of the second floor. The position of impact is in the centre of the second floor as indicated as Z2 in Figure 5.2.

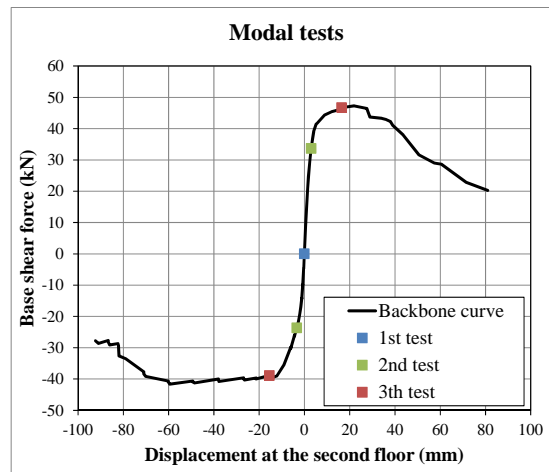


Figure 5.1 – Capacity curve obtained during the cyclic pushover test. The coloured squares indicate to which point the structure was loaded in the pushover test when the dynamic identification tests were executed after unloading from this point.

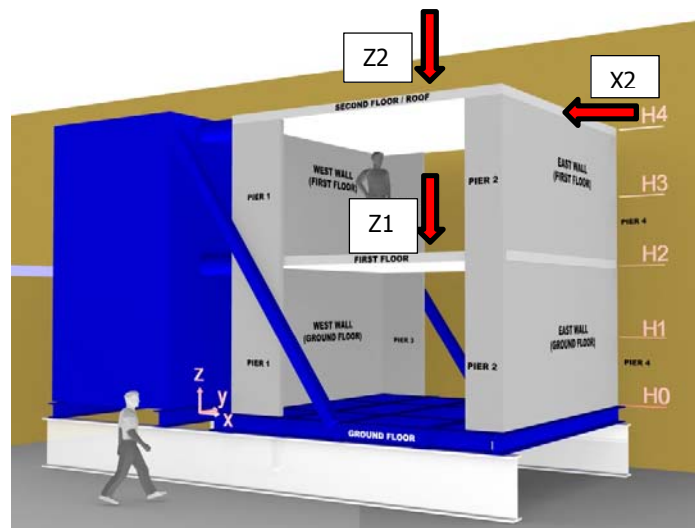


Figure 5.2 – Loading procedure for the dynamic identification test.

5.2 Experimental results

The impact tests were repeated 3 times when the assembled structure was in different damaged stages. During each impact tests 5 measurements to determine a specific eigenmode were made. Based on analysis of these 5 measurements the eigenmode could be determined. Of the studied modes the following first natural frequencies were determined.

- The first natural frequency in the X-direction of the structure. This is the direction in which the structure is loaded in the quasi-static cyclic test. See Figure 5.3a for a representation of this mode in a FE model.
- The first natural frequency in the Z-direction (vertical direction) of the first floor. See Figure 5.3b for a representation of this mode in a FE model.
- The first natural frequency in the Z-direction (vertical direction) of the second floor. See Figure 5.3c for a representation of this mode in a FE model.

A description of the FE model is presented in [3] (model "1").

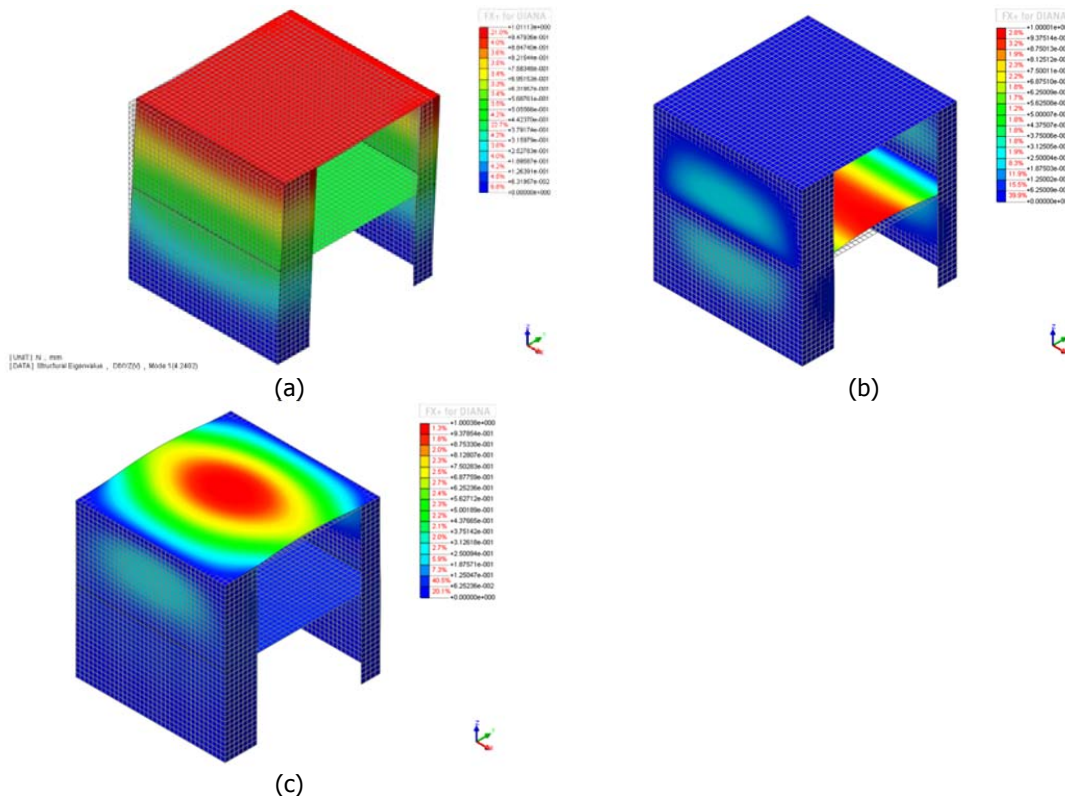


Figure 5.3 – Dynamic test: (a) First eigenmode of the structure in X-direction; (b) First eigenmode of the first floor in Z-direction; (c) First eigenmode of the second floor in Z-direction.

For the data analysis, the choice was to focus only on the first global bending mode of the assembled structure along the X-direction and the first bending mode of both floors. These modes resemble the ones that were identified in the preliminary numerical simulations of the assembled structure (Figure 5.3). Since it was clear from the modal shapes obtained with the finite element model that the global bending and local floor modes behave independently, data from both horizontal and vertical impacts of the hammer were selected for the test.

The natural frequencies that were determined through the measurements from the dynamic tests are given in Table 5.1. The natural frequency in the X-direction of the assembled structure reduces significantly in tests 2 and 3 compared with the initial natural frequency of the structure before the pushover test. This can be explained by the reduction in stiffness that is also observed in the pushover test for the relevant cycles. There is only a slight reduction of the natural frequencies of the first and second floor in Z-direction. This is because the floors are concrete floors to which no damage was observed during the pushover test. The slight reduction might be caused by the changing boundary conditions of the floors on the masonry walls.

Table 5.1 – A comparison between the identified natural frequencies in test 1 (before the start of the pushover test), test 2 (after the initial phase of the pushover test) and test 3 (after the pre-peak phase of the pushover test).

Mode	Test 1	Test 2	Test 3
	(Hz)	(Hz)	(Hz)
First mode in the X-direction of the structure	4.05	3.74	2.50
First mode in the Z-direction of the first floor	11.75	11.10	10.93
First mode in the Z-direction of the second floor	14.34	13.61	13.38

6 Interpretation of the results

In this section a further interpretation of the results is provided. First, an analytical evaluation of the capacity, in terms of maximum based shear force is presented. Second, considerations on the asymmetrical behaviour of the structure are provided. Eventually, a comparison between the obtained floors' drift values and the drift limits provided by Eurocode 8 [6] are illustrated.

6.1 Capacity

In this section a further interpretation of the results is provided by adopting an analytical calculation for the estimation of the capacity in terms of the maximum base shear force. The following assumptions are made:

1. It is conservatively assumed that the connection between the masonry walls and the concrete floor is an hinged connection. This assumption is justified by the horizontal cracks developed at the second and at the ground floor level after cycle 15 (Figure 4.20 and Figure 4.21), in which the maximum base shear force is reached for positive loading.
2. It is considered that the capacity of the structure is governed by the behaviour of the piers, by summing up the capacities of all piers in one loading direction. Consequently it is assumed that, independently on the loading direction, both piers are "active", thus they can take up lateral loading.
3. It is considered that part of the transversal wall, which is loaded out-of-plane, is moving together with the pier. This phenomenon, which is triggered by the running bond, is called "flange effect". Additionally, it is assumed that the transversal load can withstand large out-of-plane deformation with a limited loss in stability, as observed in the quasi-static cyclic out-of-plane tests on components [4]
4. It is assumed that the entire weight of the floor is equally transferred to the four piers.

Considering the aforementioned assumptions, the capacity of the structure, in terms of the maximum base shear force, is calculated from the force equilibrium in the piers assuming that only horizontal forces can be transferred between them, as shown in Figure 6.1. The piers are subjected to vertical forces due to the weight of the floors, of the transversal walls and their own weight. Due to the horizontal cracking at the floor-to-wall interface, the normal force due to the second floor changes its position on the base of the applied lateral loading direction, thus of the vertical movement of the piers. Considering the effect of the wall-to-pier interlocked connection and the initial crack pattern, a trapezoidal part of the transversal wall is assumed cooperating with the piers [5] (Figure 6.1a). Considering the piers equilibrium, the estimated capacity results approximatively equal to 49 and -42 kN for the positive and negative direction, respectively. This estimation results in line with the observed capacity as shown in Figure 6.1b.

Considering the good agreement between the experimental results and the analytical calculation, it can be concluded that the behaviour of the structure is primarily governed by the behaviour of the piers, considering that part of the transversal wall cooperates within the flange effect and that the entire weight of the floor is equally redistributed to the piers. Additionally, independently on the loading direction, both the wide and the narrow piers can be considered as "active", thus able to take up lateral load. However, having the wide piers a stiffness approximatively 4 times higher than the one of the narrow piers, they govern the overall response of the structure.

The capacity of the assembled structure can be mainly attribute to the piers, thanks to the development of the two-way out-of-plane mechanism in the transversal walls. This mechanism, which is triggered by the running bond between the transversal walls and the piers, allows the wall to withstand large deformation with a limited reduction of the capacity [4].

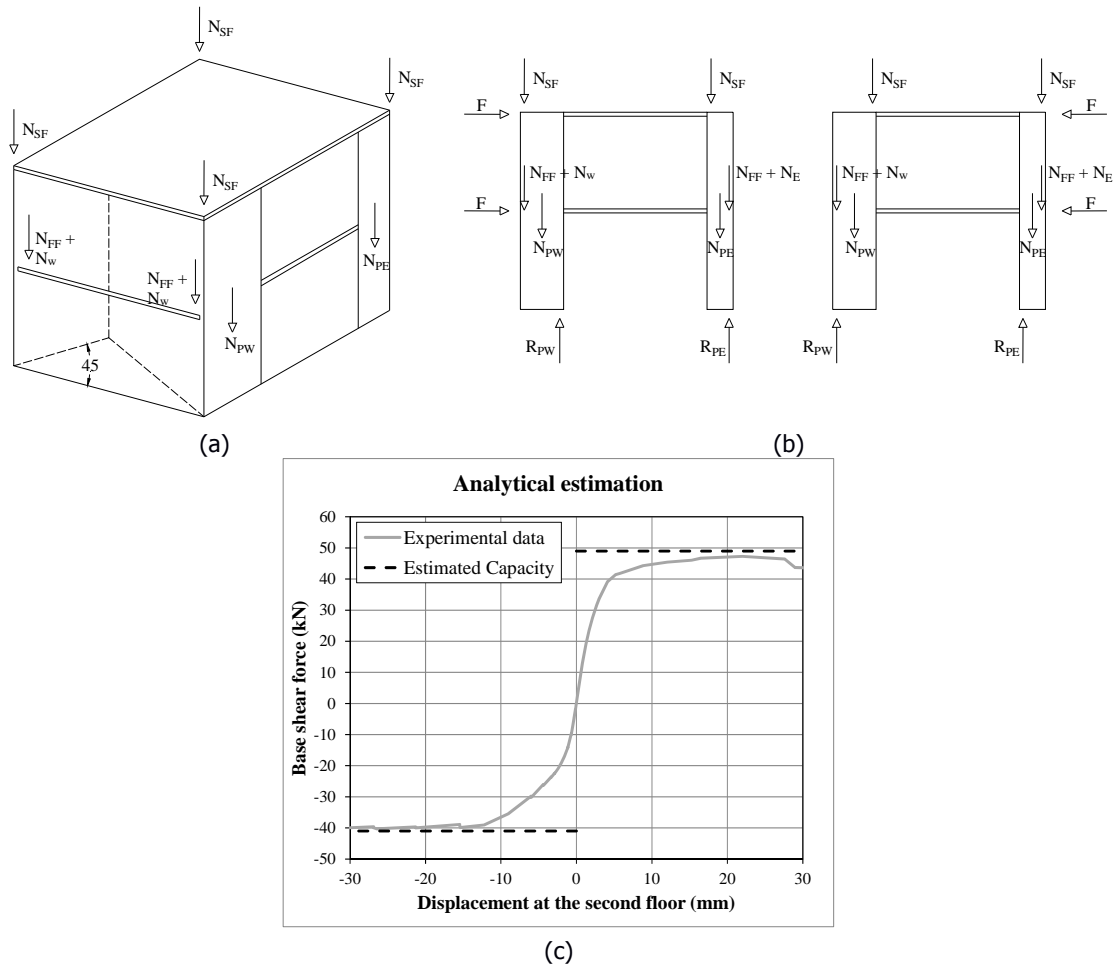


Figure 6.1 – Schematization adopted in the analytical estimate of the capacity: (a) Volume partition of the floors and of the transversal walls loading the piers; (b) Forces loading the piers for positive and negative loading; (c) Comparison between experimental results and analytical estimate.

6.2 Asymmetric behaviour

As already presented in Section 4, the asymmetric behaviour of the structure in terms of capacity and ductility response can be related to the crack pattern evolution. In this section a further analysis is provided as summary of the previous presented observations.

The initial stiffness degradation can be correlated to the rocking mechanism of the wider piers (P1 and P3). Although a similar mechanism is also triggered in the narrow piers, this has a lower impact to the overall stiffness degradation, because the moment of inertia of the undamaged narrow piers is approximately 4 times lower than the one of the undamaged wide piers.

In order to show this correlation, the development of the horizontal cracks at the bottom and top of the wide pier P1 for the pre-peak phase is compared with the capacity curve (Figure 6.2); a similar trend in terms of crack width was observed for pier P3. The sensors at the bottom corner (SH0R03) and at the top free side of the pier (SH4R02) are activated for positive displacement of the assembled structure, while the sensors on the bottom free side (SH4R01) and at the top corner (SH0R04) are activated for negative displacement of the assembled structure (Figure 6.2b). The dashed line indicates the displacement at which the horizontal cracks reach approximately 0.1 mm (the exact data of each sensor is reported in the dedicated labels). Comparing the positive and negative loading direction, it is possible to correlate the asymmetric behaviour of the structure in the pre-peak phase to the crack opening. A crack opening of approximately 0.1 mm is first reached for negative loading at a displacement $d_2 = -1.2$ mm (cycle 4) corresponding to a base shear force of approximately -17 kN. Subsequently, the same crack opening is reached for positive loading at displacement $d_2 = +4.3$ mm (cycle 10) corresponding to a base shear force of approximately +39 kN.

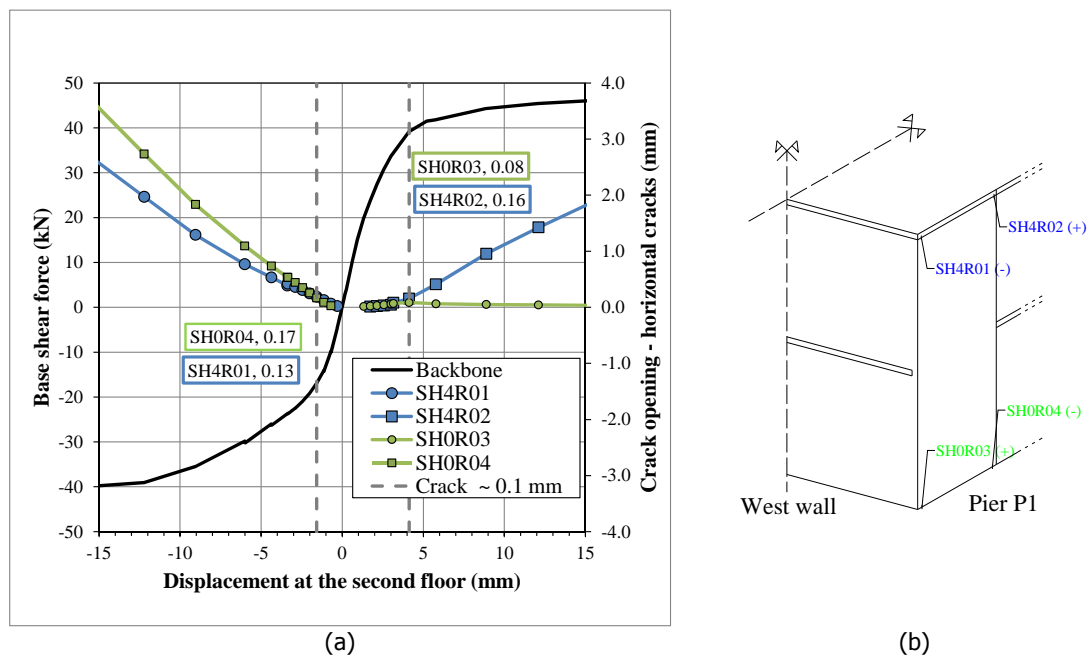


Figure 6.2 – Analysis of pre-peak behaviour: (a) Comparison between the capacity curve and the development of the horizontal cracks at the bottom and top of pier P1; (b) Location of the sensor with indication of loading direction (+ or -) which activate them. Crack opening lower than 0.01 mm have been not reported in the graph for clarity sake. See also Figure 4.10 and Figure 4.12.

The softening behaviour observed during the post peak phase can be correlated to the formation of diagonal/vertical cracks within the wide piers (P1 and P3). Figure 6.3 shows this analysis for the post-peak. A degradation in base shear force is first observed in the positive loading direction during cycle 17 ($d_2 = \pm 38.5$ mm), which corresponds to the formation of the first vertical/diagonal crack in the wide pier P3. Immediately afterwards, the same failure mechanism is observed for the wide pier P1 during cycle 18 ($d_2 = \pm 50$ mm). During this cycles the capacity of the structure for negative displacement remains nearly constant until cycle 19 ($d_2 = \pm 60$ mm). During cycle 19, the formation of a secondary diagonal/vertical crack in the

wide pier P3 leads to the degradation in base shear force for negative loading. Considering that an extensive crack of the narrow pier P2 and P4 only occurs during cycle 20 ($d_2 = \pm 72$ mm), it is possible to establish the correlation between the diagonal/vertical cracks in the wide piers (P1 and P3) and the softening behaviour.

The formation of the diagonal/vertical cracks within the wide piers influences the orientation of the compressive stress within the masonry. Considering the schematization in Figure 6.1, the vertical compressive loading of the second floor N_{SF} and the reaction forces at the bottom of the pier R_{PW} determine the orientation of the diagonal compressive stress in the pier. Considering that the vertical load induced by the second floor N_{SF} is changing position due to the rocking behaviour of the pier, the diagonal cracks have a different influence for positive and negative loading. For positive loading, a reduction in cross-section of the pier directly redistributes the compressive diagonal reducing the lever arm. On the contrary, for negative loading, an extensive reduction of the cross-section is necessary to induce a reorientation of the compressive stress diagonal. Furthermore, for negative loading the compressive side is supported by the interlocking with the transversal wall, while for positive loading there is no transversal support for the compressive side.

In conclusion, the asymmetric behaviour of the capacity curve can be correlated with the damage of the wide piers. The stiffness degradation in the pre-peak phase can be associated with the rocking mechanism in the wide piers and results strongly affected by the mechanical interlocking connecting the transversal walls and the piers. The softening behaviour of the capacity curve can be associated to the development of primary and secondary diagonal/vertical cracks in the wide piers, thus to the distribution of the diagonal compression stresses in the piers. Following the aforementioned analysis, it is also possible to conclude that the wide piers can be consider as "active" piers for both negative and positive loading.

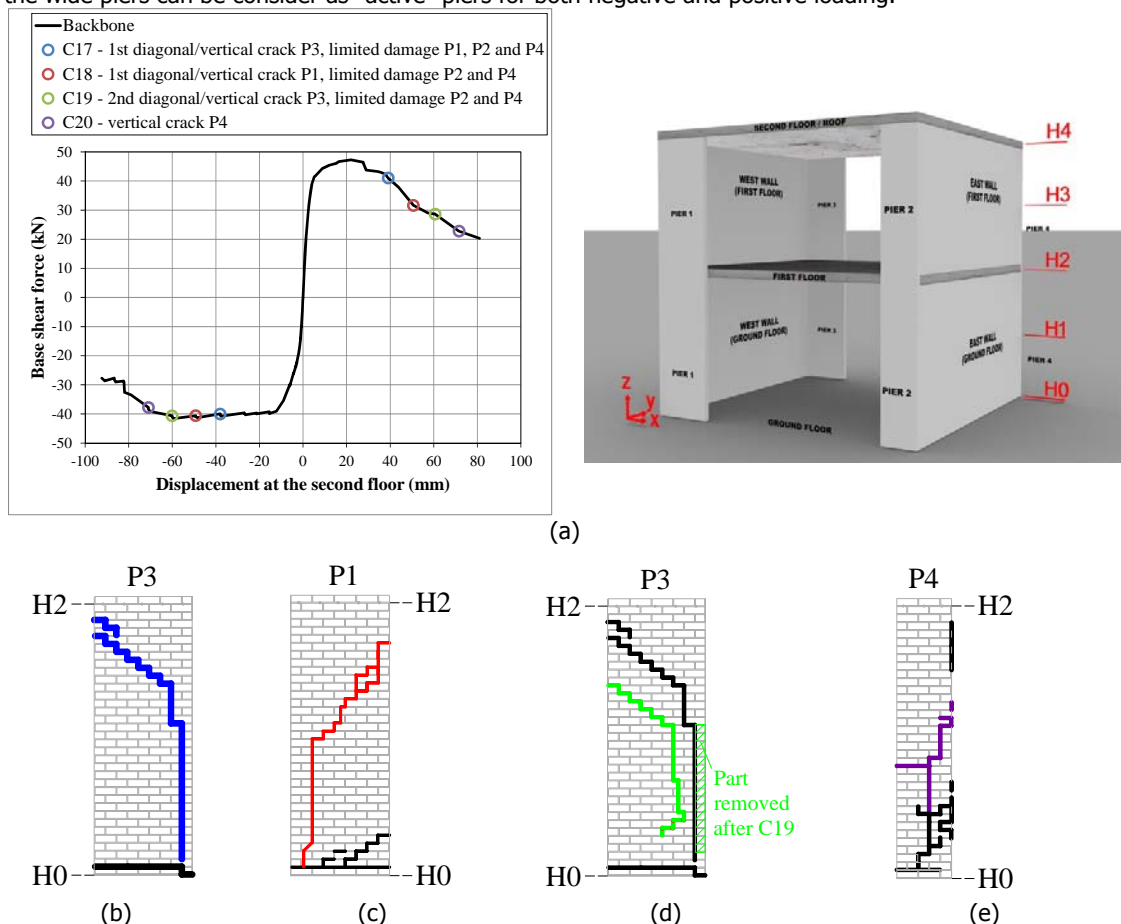


Figure 6.3 – Analysis of post-peak behaviour: (a) Backbone curve with indication of main cracks; (b) First diagonal/vertical crack in the wide pier P3; (c) Second diagonal/vertical crack in the wide pier P1; (d) First diagonal/vertical crack in the wide pier P1; (e) Vertical crack in the narrow pier P4. For complete crack

pattern please refer to Figure 4.22, Figure 4.24, Figure 4.25 and Figure 4.26.

6.3 Drifts

In this section a comparison between the drifts value observed during the test and the drift limits proposed by Eurocode 8 [6] is reported.

According to the Annex C of Eurocode 8, the maximum capacity of the primary seismic unreinforced masonry wall controlled by flexure may be expressed in terms of drift, which can be taken equal to:

$$d_{r,SD} = 0.008 \frac{H_0}{D} \quad (2)$$

$$d_{r,NC} = \frac{4}{3} 0.008 \frac{H_0}{D} \quad (3)$$

where $d_{r,SD}$ is the drift value for limit state of significant damage and $d_{r,ND}$ is the drift value for limit state of near collapse, H_0 is the height of the section where the flexural capacity is attained and the contraflexural point and D is the in-plane horizontal dimension of the wall.

Table 6.1 compares the drifts evaluated as in Eqs. (2) and (3) with the experimental values. The latter results lower than the one proposed by the standard. However, they result closer to the drift values estimated for the wide piers.

Considering the positive loading direction, a drift of approximately 1.5% was observed for both the first and second floor. This value corresponds to 80% and 60% of the estimated value for limit state of significant damage and for limit state of near collapse, respectively.

For negative loading, the first floor presented a lower drift with respect to the second floor. For the second floor, a drift value of 1% was measured, which resulted 50% and 60% of the estimated value for limit state of significant damage and for limit state of near collapse, respectively. For the first floor a drift value of 2.2% was measured, which resulted 110% and 80% of the estimated value for limit state of significant damage and for limit state of near collapse, respectively.

Following the estimate of the drifts value in agreement with Eurocode 8, it can be concluded that:

- The limit state of significant damage was reached during the test for negative displacements
- The limit state of near collapse was not reached during the test (this was expected because of safety issue the maximum possible drift was limited)
- The comparison for the drift limits is confirming that the wide piers are governing the structural response

Table 6.1 – Comparison between experimental results and analytical formulations proposed by Eurocode 8 in terms of drifts.

Case		Drift (%)	
		Wide piers	Narrow piers
Experiments (Cycle 21)	Positive displacement – both floors	1.5	
	Negative displacement - second floor	1.0	
	Negative displacement – first floor	2.2	
Eurocode 8	Limit state of significant damage	1.9	3.6
	Limit state of near collapse	2.6	4.8

6.4 First natural frequency

In this section, the first natural eigenfrequency of the assembled structure determined via the dynamic identification test is compared with the one calculated from the quasi-static cyclic test. T

Considering the assembled structure as a two-degree of freedom system, its natural frequencies can be calculated as:

$$K - \omega M = 0 \quad (4)$$

where K is the stiffness matrix, M the mass matrix and ω the eigenvalue matrix from which the natural frequencies can be determined.

The stiffness matrix K can be determined on the basis of the stiffness of the first and second floor as measured during the quasi-static cyclic pushover tests. The stiffness of the assembled structure can be evaluated via linear regression of the capacity curves in terms of displacement at the second and first floor level. The following cycles, which have been performed immediately after the dynamic identification test, are adopted for the estimation of the stiffness of the assembled structure:

- Undamaged state of the assembled structure: **Cycle 1** (Figure 6.4a,b) of the quasi-static test to be compared with **Test 1** of the dynamic identification test.
- Slightly damaged state of the assembled structure, including reduction in stiffness but no visible cracks: **Cycle 2b** (Figure 6.4c,d) of the quasi-static test to be compared with **Test 2** of the dynamic identification test.
- Significant damaged state of the assembled structure including stiffness reduction and visible cracking: **Cycle 2c** (Figure 6.4e,f) of the quasi-static test to be compared with **Test 3** of the dynamic identification test.

It can be observed that for the cycles 2b (first cycle of the pre-peak phase) and the 2c (first cycle of the post-peak phase) a linear response of the structure is found at small displacements, even if in the cycles before a non-linear behaviour at larger displacements occurred.

Comparing the first natural eigenfrequency determined with the dynamic identification tests and the one calculated based on the quasi-static cyclic pushover test, a good agreement can be found (Table 6.2). Consequently, the dynamic identification test, performed adopting the impact method, results a valuable testing method to assess the stiffness of a (un)damaged structure.

Table 6.2 – A comparison between the identified natural frequencies by the dynamic tests and calculated with the stiffness's obtained in the quasi static pushover test.

First mode in the X-direction of the structure	Test 1	Test 2	Test 3
	(Hz)	(Hz)	(Hz)
Experimental results of the dynamic identification test	4.05	3.74	2.50
Calculated based on the stiffness obtained in the quasi-static pushover test	4.07	3.58	2.29

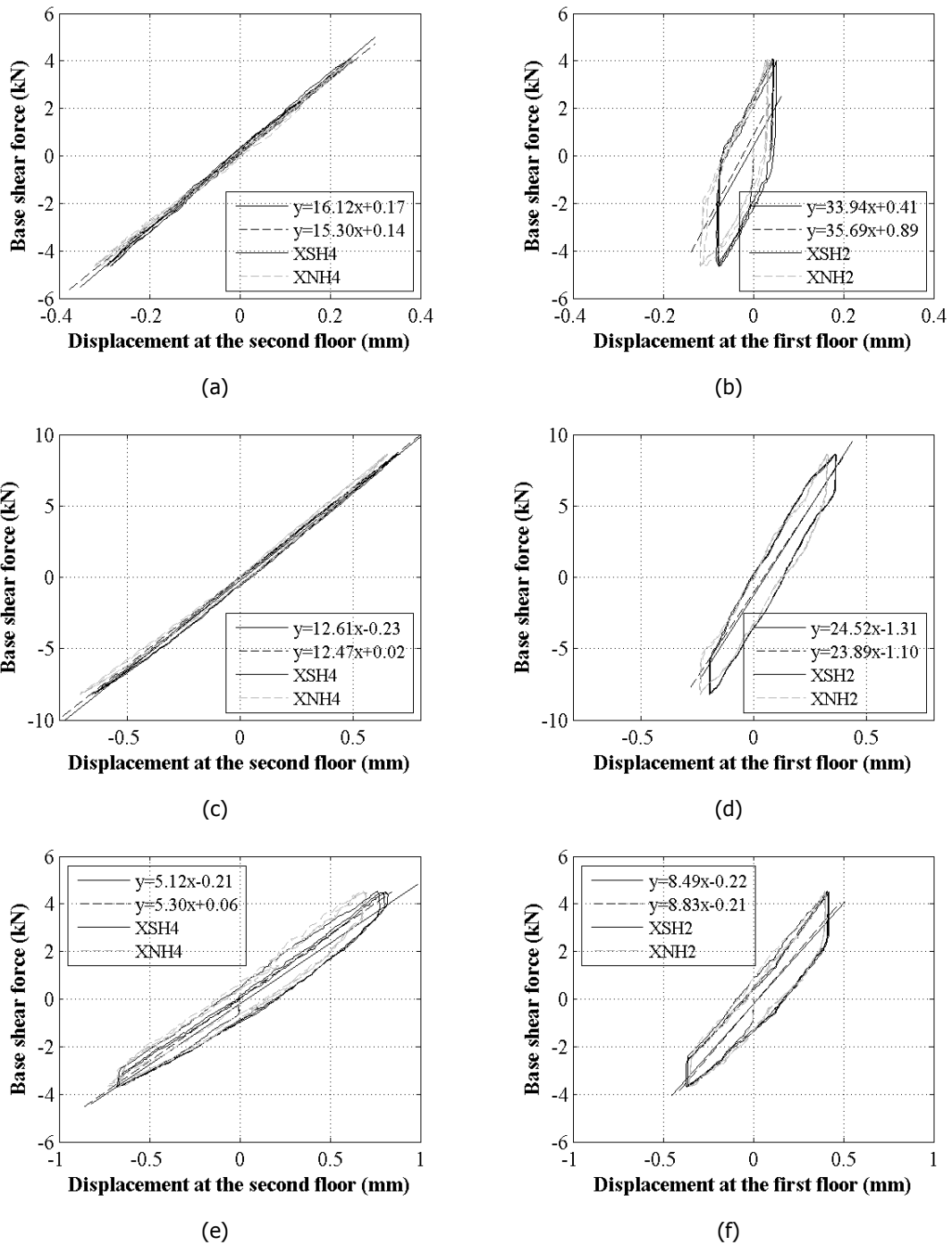


Figure 6.4 - Base shear force versus displacement at the second and at the first floor level: (a)-(b) Cycle 1; (c)-(d) Cycle 2b; (e)-(f) Cycle 2c.

7 Conclusions and recommendations

A quasi-static cyclic pushover test and dynamic identification test were performed on an two-story high assembled structure made of calcium silicate brick masonry. The assembled structure is representative of a typical terraced house built in the period between 1960 and 1980 in the Groningen area. The geometry of the assemblage has been designed to investigate the influence of the following buildings' characteristics:

- Presence of slender piers, due to the presence of large openings in the facades
- Presence of long transversal walls that are connected to the facades by the running bond
- Limited connection between concrete floor and masonry wall

The structure was composed of two loadbearing walls on the western and eastern side and two identical facades on the northern and southern side. Both façade were composed of a wide pier with a width of 1100 mm and a narrow pier with a width of 660 mm.

The main object of the tests was to characterise the structural response of the assemblage to provide a benchmark for the validation of numerical and analytical models to be used for the assessment of existing buildings subjected to seismic loading. For this purpose, the test on the assembled structure was part of a larger project including quasi-static cyclic tests on large scale walls, destructive material tests and test on connections.

The quasi-static cyclic pushover test allowed determining the capacity curve of the assembled structure in terms of base shear force versus displacement at the top floor level. Thanks to the displacement control system adopted, both the pre-peak and post-peak phase, where softening occurred, could be investigated including the hysteretic response.

Following the interpretation analysis in Section 6, the shape of the capacity curve (Figure 4.5) could be correlated with the observed crack pattern:

- The first observed stiffness degradation is caused by the formation of cracks at the floor-to-wall connection along the transversal walls (Figure 4.9, Figure 4.10). Because part of the transversal walls act as a flange for the piers in the loading direction, this cracking gives a stiffness reduction in the loading direction. Subsequently, the rocking mechanism of the wide piers plays an important role on the stiffness degradation in the pre-peak phase (Figure 6.2).
- The asymmetric behaviour of the assembled structure for positive and negative loading can be explained:
 - in the initial and pre-peak phase, by the formation of horizontal cracks at the top and bottom of the wide piers, thus to their rocking mechanism (Figure 6.2)
 - in the post-peak phase, by the formation of primary and secondary diagonal/vertical crack in the wide piers (Figure 6.3)
- The damage evolution within the wide piers determines the behaviour of the overall structure, in terms of degradation of both the stiffness and the capacity, for both the negative and the positive loading.
- In the pre- and post-peak phase an accumulation of inelastic deformation (at zero forces) is observed for positive loading, as shown in the capacity curve in Figure 4.11 and Figure 4.19. This phenomenon might be related to the different sliding/friction behaviour in the cracks for the two loading direction. Further investigations to map the phenomenon are needed.
- The running bond between the piers and the transversals walls has a twofold effect:
 - allows part of the transversal wall to act as a flange for the piers in the loading direction (flange effect)
 - triggers the two-way out-of-plane mechanism in the transversal walls, which allows withstanding large deformation without loss of stability. This is in line with the findings of the quasi-static cyclic out-of-plane tests on components [4].
- Considering the good agreement between the experimental results and the analytical calculation (Section 6.1), it can be concluded that the maximum base shear force can be calculated by analysing the behaviour of the piers, considering that part of the transversal wall cooperates within the flange effect and that the entire weight of the floor is equally redistributed to the piers. Independently on the loading direction, both the wide and the narrow piers can be considered as "active", thus able to take up lateral load. However, having the wide piers a stiffness approximately 4 times higher than the one of the narrow piers, they govern the overall response of the structure.

The dynamic identification test, performed adopting the impact method, results a valuable testing method to assess the stiffness of a (un)damaged structure. Thanks to the dynamic identification tests, the eigenfrequency at different damage stages could be determined. The test allowed determining the first global bending mode of the assembled structure along the X-axis and the first bending mode of both floors along the Z-axis. Comparing the first natural eigenfrequency (first mode along X-axis,) determined with the dynamic identification tests and the one calculated based on the quasi-static cyclic pushover test, a good agreement can be found in the determination of the eigenfrequency reduction (Table 6.2).

On the basis of the presented conclusions, the following variations are considered of interest for further quasi-static cyclic pushover tests on assembled structures:

- Variation masonry type, including variation of masonry unit size (e.g. elements or block masonry)
- Variation in construction techniques adopted for the masonry (e.g. double wythe walls)
- Variation in the connection between transversal walls and facades piers (e.g. glued or dry connection, Figure 7.1a)
- Variation in the connection between the facades piers and the floor (e.g. piers being constrained vertically by the floor, at each story level, Figure 7.1b)
- Different type of rigid diaphragms with orthotropic behaviour (e.g. hollow core slabs, Figure 7.1b);
- Flexible diaphragms (e.g. timber floors, Figure 7.1c);
- Evaluation of strengthening measures for different intervention levels.

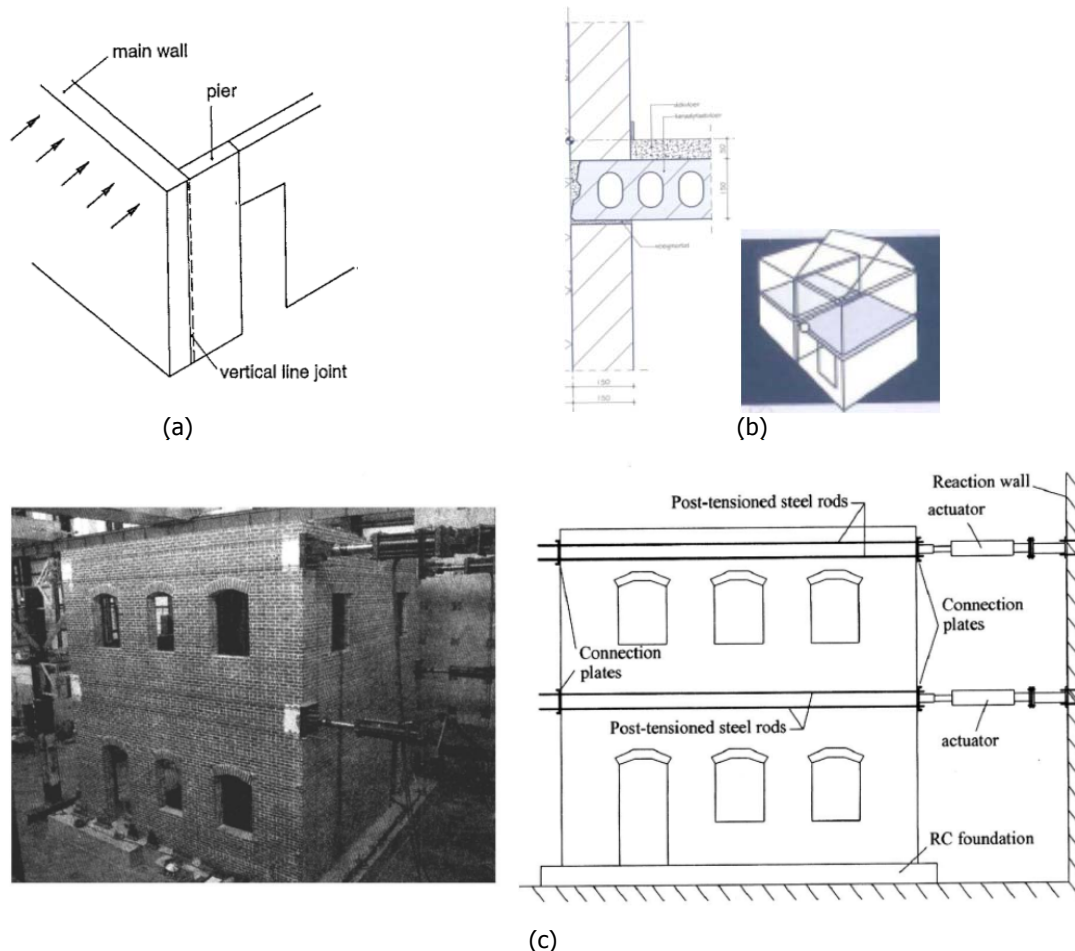


Figure 7.1 – Variations for quasi-static cyclic tests on assembled structure: (a) Glued or dry connection between transversal walls and facades piers [7]; (b) Variation in the connection between the facades piers and the floor and in the type of rigid floor [8]; (c) Example of a pushover test on assembled structure having timber diaphragms (timber diaphragms not visible on the picture) [5].

References

- [1] Esposito R., Messali F. and Rots J.G. Material characterisation of replicated masonry and wall ties. Delft University of Technology. Final report 18 April 2016.
- [2] Terwel, K., Esposito, R. and Badri, S. Construction Report of the Full-Scale Assemblage, Delft University of Technology, Dept. Structural Engineering, 6 October 2015.
- [3] Messali, F. Blind predictions of the pushover test on an assembled structure, Delft University of Technology, Report version 1 25 December 2015.
- [4] Ravenshorst, G. and Messali, F. Out-of-plane test on replicated masonry walls. Delft University of Technology. Final report 29 April 2016.
- [5] Yi, T. Experimental investigation and numerical simulation of an unreinforced masonry structure with flexible diaphragms. 2014. Ph.D. thesis. Georgia Institute of Technology.
- [6] NEN-EN 1998-3:2005. Eurocode 8: Design of structures for earthquake resistance - Part 3: Assessment and retrofitting of buildings. Nederlands Normalisatie-instituut.
- [7] J.G. Rots, (1997) Structural masonry: An Experimental/Numerical Basis for Practical Design Rules. A. A.Balkema, Rotterdam.
- [8] SBR Referentie Details Woningbouw (2007). Student edition, ThiemeMeulenhoff (in Dutch).

Appendixes

A. Explanation of the load distribution on the assemblage during the test

As described in Section 4.1, the assemblage was loaded in displacement control at the second floor level (H4) and, simultaneously, a ratio of 1:1 was imposed between the forces at the second (H4) and first floor (H2) level. To impose the displacement at the second floor level, external potentiometers placed between the plates of the actuators (SXS and SXN) were adopted for a stable and safe control system. Due to the small play in the hinges of the actuators and the deformation of the steel reaction frame, the lateral displacements imposed to the loading points at the second floor level could not be equal to the displacements imposed to the cylinders of the actuators. Consequently, an external wooden frame was used to measure the absolute displacements of the assemblage (XSH4 and XNH4) and of the steel reaction frame (XFRSH4 and XFRSH4) at the location of the actuators. The external wooden frame can be considered as an absolute reference, because it was connected neither to the steel reaction frame nor to the assembled structure, thus was not subject to loading. The wooden frame was kept stable both by internal bracing with diagonals and by posttensioned steel cables and anchors attached to various static points around (but not in contact with) the test setup.

To impose the relation between the forces at the first and second floor level (1:1 ratio), the forces in the actuators No. 1 and 3, related to the imposed displacement, were not only measured, but also hydraulically coupled with the actuators No. 2 and 4, respectively, at the first floor level. The hydraulic coupling would offer a physical guarantee that each pair (norther and southern side) of one upper and one lower identical actuator always were controlled to the same oil pressure = force. Figure A.1 shows the overview of the loading points and of the measured quantities.

Although the desired ratio 1:1 between the actuators' forces at the second (F_3+F_1) and first (F_4+F_2) floor level was achieved in all three phases of the test (Figure A.2), a variation of the actuators' forces between the southern and northern side was observed. Figure A.3 shows the variation of the imposed force at the southern (F_3) and northern (F_1) side at the second floor level. Being each actuator on the second floor coupled to the one right below it at the first floor, the same difference between actuators' forces on the southern and northern side at the first floor level was observed.

This difference in actuators' forces was not desired, because it was not a requirement of the loading scheme and it can be correlated to the behaviour of the steel reaction frame. Figure A.4 shows the difference in displacements between southern and northern side of both the assemblage and the steel reaction frame. Both measurements were taken from the external wooden frame. Although the difference in deformation of the steel reaction frame does not exceed 0.25 mm, it has an influence of the difference between the actuators' forces, as highlighted in Figure A.5. Consequently, the asymmetric response of the reaction frame induces a difference in the actuators' force, which results in a play in the hinges of the actuators with consequent application of a displacement difference on the assembled structure.

For undamaged state of the structure, the difference between the actuators' forces on the northern and southern side is caused by the stiffness of the reaction frame, but for damaged state of the assembled structure this asymmetry force distribution is also caused by the cracking in the structure. Thanks to the adopted control system (two actuators at each floor level), the undesired torsional failure of the assembled structure is prevented once extensive (asymmetric) cracking occurs. In fact, the ratio between absolute displacement in loading direction and the difference in the absolute displacement between northern and southern is only 1.6 % for the largest displacement.

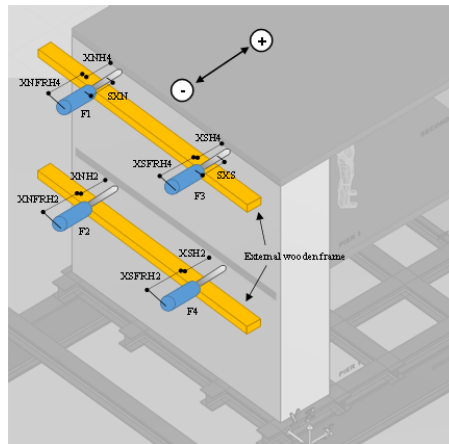


Figure A.1 – Location of actuators and sensors for displacement measurements.

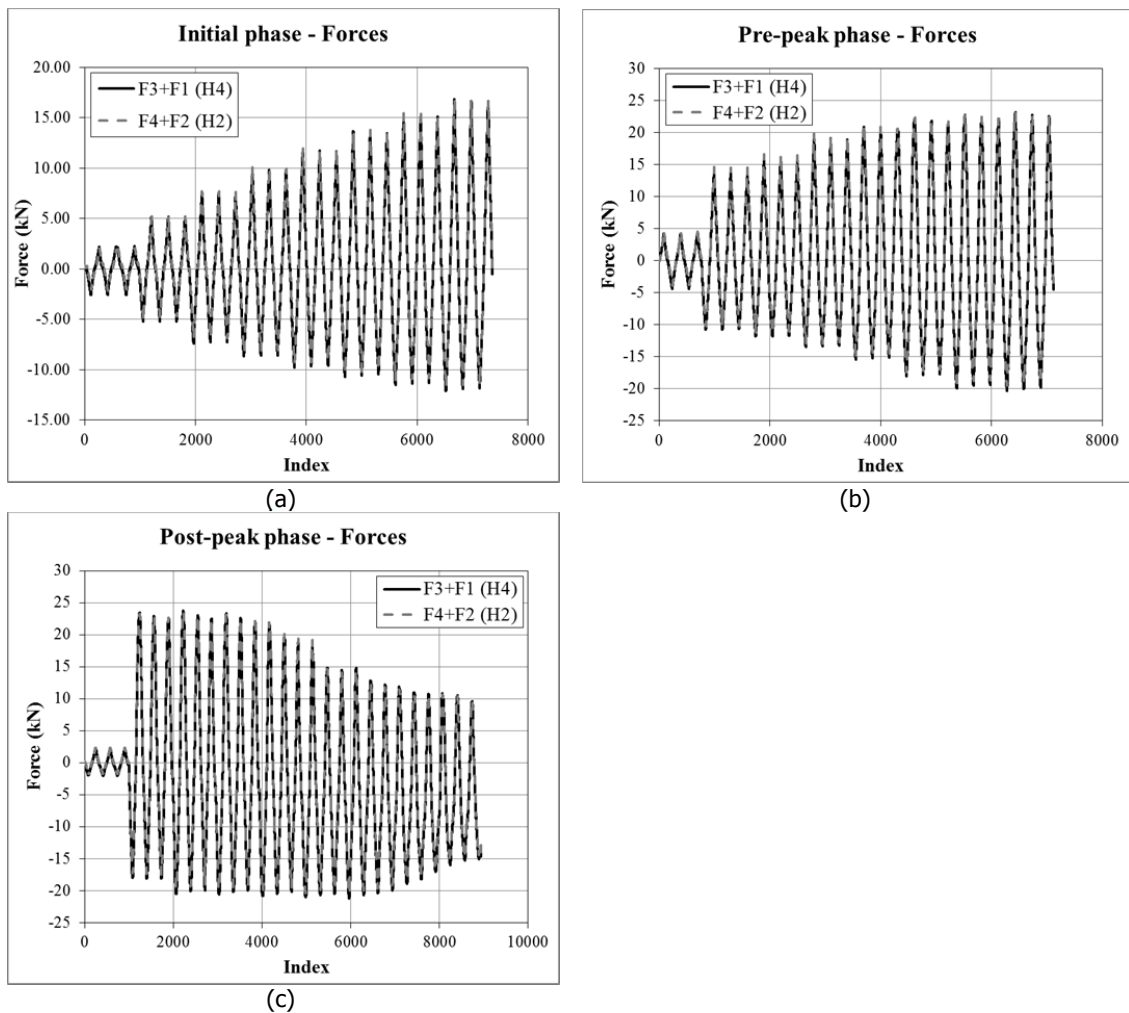


Figure A.2 – Comparison between forces at the second (F_3+F_1) and first (F_4+F_2) floor level: (a) Initial phase; (b) Pre-peak phase; (c) Post-peak phase.

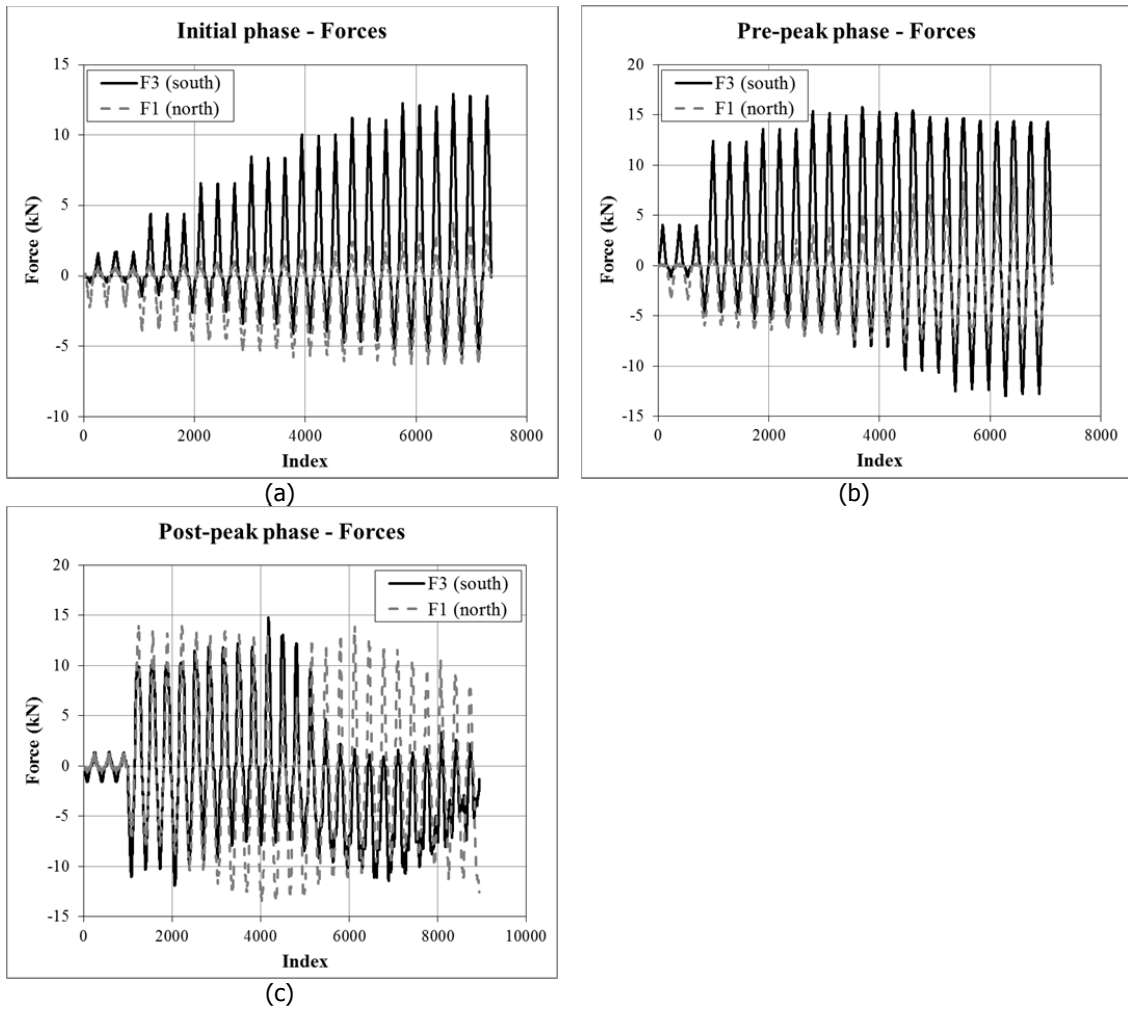


Figure A.3 – Comparison between actuators' force at the southern (F_3) and northern (F_1) side at the second floor level: (a) Initial phase; (b) Pre-peak phase; (c) Post-peak phase.

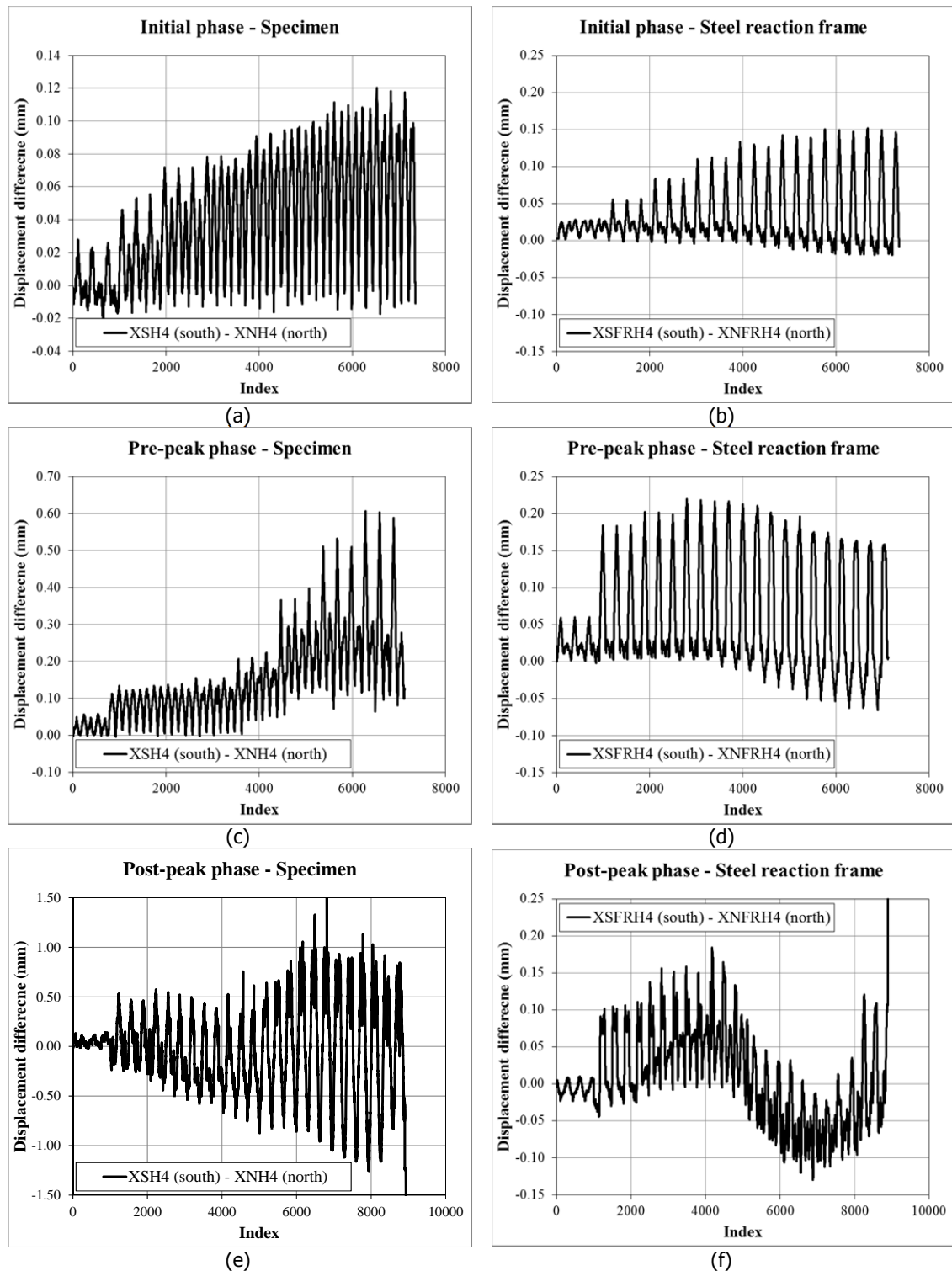


Figure A.4 – Displacement difference measured on the assemblage and on the steel reaction frame: (a)-(b) Initial phase; (c)-(d) Pre-peak phase; (e)-(f) post-peak phase.

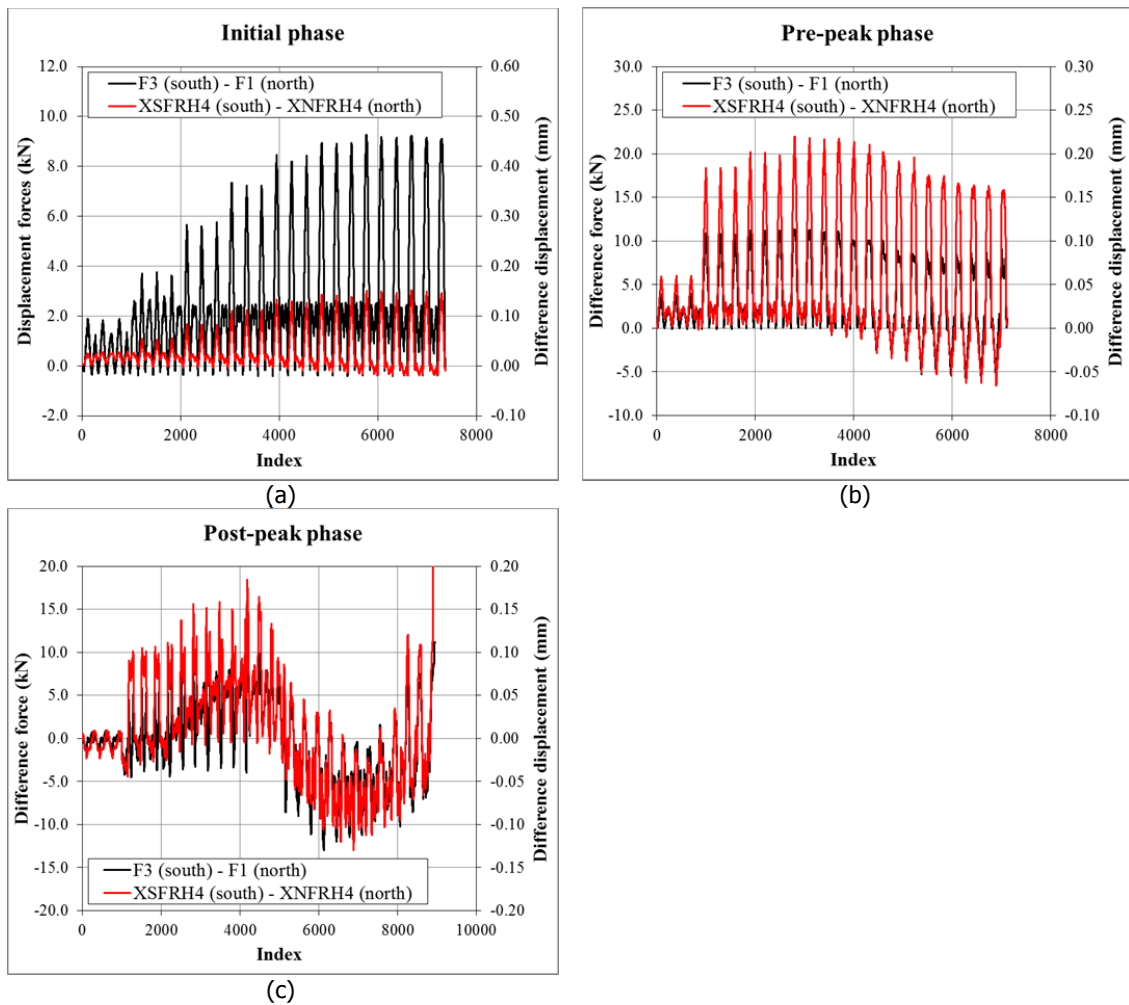


Figure A.5 – Comparison between the difference in forces ($F_3 - F_1$) and the difference in displacement of the steel reaction frame (XSFRH4-XNFRH4): (a) Initial phase; (b) Pre-peak phase; (c) post-peak phase.

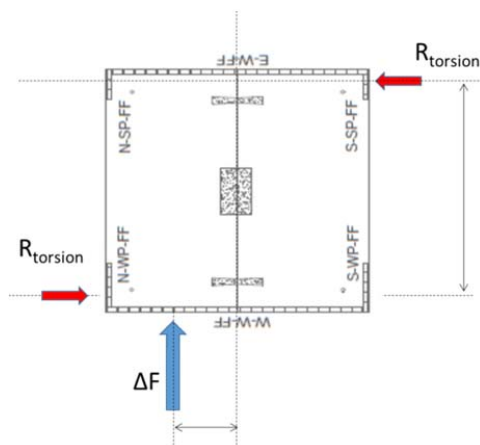


Figure A.6 – Torsion on the long walls caused by the difference of the forces between the north and the south side.

Even if the difference between the southern and the northern side in actuator's forces was observed, its impact on the initial stress state of the assembled structure can be considered limited. The torsional moment caused by the force difference is redistributed by the stiff concrete floor to the transversal walls on the eastern western side, as shown in Figure A.6. Considering the maximum force difference of 23.5 kN, a shear stress in the transversal wall of 0.015 MPa can be calculated analytically. Being the initial shear strength of the masonry ($f_{v0} = 0.14$ MPa) approximately ten times higher than the induced shear stress, it can be concluded that the asymmetric loading has a negligible influence on the capacity of the assemblage along the loading direction (X-axis).

In order to further assess the influence of the difference between the actuator's forces on the southern and northern side of the assembled structure, a finite element analysis has been performed for the initial phase. The main goals of the performed analysis are:

- to assess that the displacement difference of the assembled structure are consistent with the force difference measured in the actuators.
- to assess that the stiff floors and transversal walls are able to redistribute the torsional moment, generating a limited variation of the stresses in the transversal wall.
- To assess that the redistribution of the torsional moment provokes a limited difference in the stress state of the piers.

The numerical model is described in the Ref. [3] (model "1"). Since the interest is devoted to the initial phase, a linear elastic analysis was performed. In order to reproduce the experimental conditions, the loads were applied according to the following procedure:

- First, the gravity load is applied
- Second, a difference between the applied displacements at the second floor level on the southern and northern side is applied by linearly increasing the displacements XSH4 and XNH4 up to an absolute maximum displacement of 3 mm and 2.9 mm, respectively. It is obtained a final displacement difference of 0.1 mm, which is approximately equal to the measured difference during the test at the end of the initial phase (Figure A.4a).
- Additionally, the ratio between the forces in the coupled actuators on the same side (F_1/F_2 and F_3/F_4) is kept constant and equal to 1 throughout the analysis.

The outcomes of the analysis show a difference between the reactions forces equal to $(F_1+F_2) - (F_3+F_4) = 22.3$ kN, for displacement difference of XSH4 - XNH4 = 0.1 mm, which is approximately 10% larger than the measured force difference measured during the test (compare Figure A.7 with Figure A.5a).

The sum of the reactions measured at the nodes on the base line of the piers is reported in Figure A.5: the difference is about 2 kN, which is about 10% of the difference measured in the actuators. Moreover, very small differences can be detected in the stress distribution in the piers of the northern and southern side of the assembled structure. As an example, Figure A.8a shows the distribution of the positive principal stresses in the piers for imposed displacements XSH4 = 3 mm and XNH4 = 2.9 mm.

The force difference between the northern and southern side causes a torsional moment on the structure that determines shear forces in the transversal wall. The stresses generated by those forces are small, in line with the values that can be estimated if a uniform stress distribution on the panels is assumed. As an example, Figure A.8b shows the distribution of the shear stresses in the eastern transverse wall for an imposed displacements XSH4 = 3.0 mm and XNH4 = 2.9 mm. A stress localisation is observed at the corner between the transversal wall and the piers in correspondence of the floor. This localisation was already present after the gravity load was imposed prior to the application of any lateral load; consequently it can be related to the deflection of the floors due to self-weight and not to the induced torsional moment.

The main outcomes obtained by the performed finite element analysis are the following:

- the difference of forces in the actuators is consistent with the difference in displacements XSH4 and XNH4.
- the difference between the actuator's forces on the southern and northern side is substantially larger than the difference in base shear force in the northern and southern piers (Figure A.7).
- the stiff floors and the transversal walls are able to redistribute the forces generated by the asymmetric loading conditions, consequently the loading conditions of the piers on the northern and the southern side of the assembled structure are close to similar.
- the forces required to redistribute the asymmetric loading to the piers are small and do not alter significantly the stress distribution on the transversal walls.

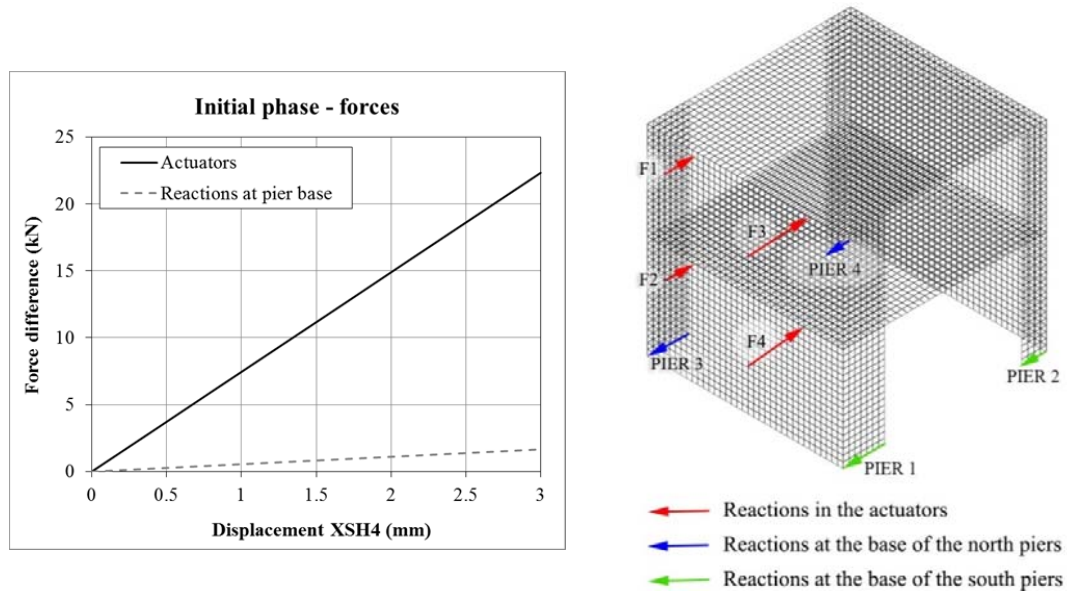


Figure A.7 – Comparison between the force difference in the actuators ($F_1+F_3-F_2-F_4$) and at the base of the piers (south – north).

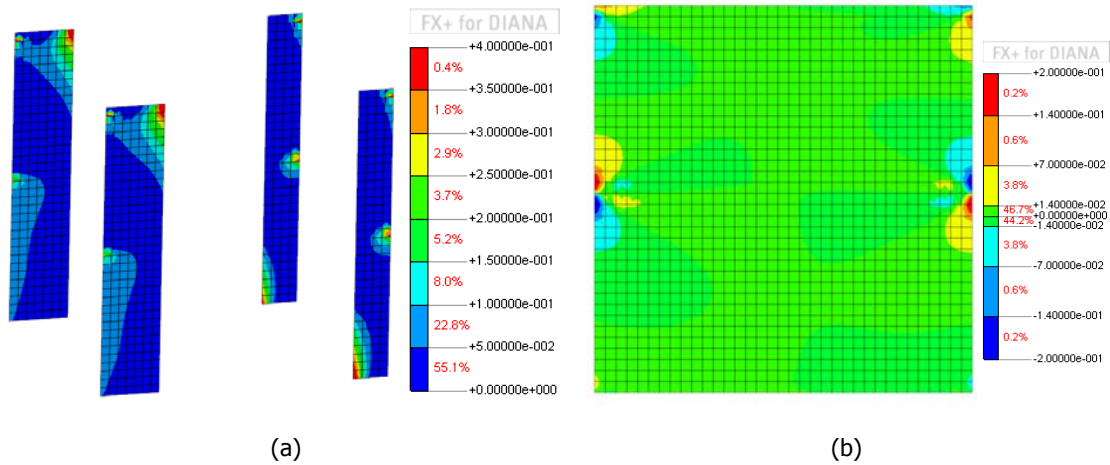


Figure A.8 – Stress distribution in the house for an imposed displacement of 3 mm at point XSH4: (a) Positive principal stresses in the piers; (b) Shear stresses in the transversal wall.

Considering the aforementioned analysis of the loading conditions and the results of the analytical and numerical models, the following conclusions can be drawn:

- The adopted control system allowed imposing a ratio 1:1 between the forces at the first and second floor level, while performing a displacement control test along the X-axis (Figure A.2).
- The difference in actuators' forces on the southern and northern side was not restricted during loading and it can be correlated to a slightly asymmetric behaviour of the steel reaction frame (Figure A.5) for undamaged state of the assembled structure.
- The forces in the actuators cannot directly be compared with the base shear forces in the piers, because the high torsional stiffness of the floor and of the transversal wall allows redistributing the asymmetric loading. As a result, in the undamaged state the difference between base shear force in the piers on the northern and southern side can be estimated as no more than 10% of the difference between the actuators' forces on the two sides, as shown by the numerical analysis (Figure A.7).
- Thanks to the adopted control system (two actuators at each floor level), the undesired torsional failure of the assembled structure is prevented once extensive (asymmetric) cracking occurs.
- Limiting the difference in applied displacements at the second floor level is very difficult to achieve and it does not guarantee a symmetric deformation of the entire structure.

The following recommendations can be given:

- The influence of the initial asymmetric loading on the global behaviour of the assembled structure can be studied by performing nonlinear finite element analysis imposing the measured displacement/loading history. However, the variability of other parameters, such as the distribution of material properties in the structure, should also be object of this investigation.
- To experimentally determine the torsional stiffness of the assembled structure, in the elastic phase cycles in force control can be applied by imposing the same force in each actuator and measuring the corresponding displacement difference on the southern and northern side along the loading direction.

B. Instrumentation list

The measurement system has been designed to record as thorough as possible a description of the assembled structures' deformation behaviour under quasi-static cyclic imposed lateral deformation. The following aspects received attention:

- Reaction force measurement for both floors during imposed lateral displacement cycles
- Possible differences in reaction forces in the actuators on north and south side
- Evaluation of the capacity curve in terms of:
 - Relation between imposed cyclic displacement and measured base shear force,
 - Stiffness degradation in the various phases
 - Softening behaviour
 - Hysteretic behaviour and energy dissipation
- Observe the interaction between the in-plane deformation of the piers and the out-of-plane behaviour of the transversal walls.
- Observe the influence of different pier sizes and investigate the mechanism of "active" and "passive" piers.
- Observe crack locations, crack width and crack pattern evolution
- Horizontal and vertical (in-plane) displacements and rotations in piers
- Horizontal and vertical (in-plane) displacements and rotations in transversal walls
- Out-of-plane displacements of both piers and transversal walls
- Deformation of the concrete floors
- Possible crushing of calcium silicate brick masonry near concrete floor support positions
- Behaviour of connection 1st floor - pier (the detail that only takes out-of-plane loads)
- Deformation of the steel frame (test tower and foundation beams)
- Recording of possible unforeseen behaviour for safety measurements

Table B.1 lists the sensors used with indication of type and maximum stroke. Figure B.1 to Figure B.4 show the sensors' location.

Table B.1 – Overview of used sensors with indication of sensors type and maximum stroke.

No. channel	Label	Sensor type	Stroke from zero position
000	F1	load cell	
001	F2	load cell	
002	F3	load cell	
003	F4	load cell	
012	XSH4	Linear Potentiometer on timber strip	-100 to +100 mm
013	XNH4	Linear Potentiometer on timber strip	-100 to +100 mm
018	XSH0	Linear Potentiometer on timber strip	-10 to +10 mm
019	XNH0	Linear Potentiometer on timber strip	-10 to +10 mm
020	XSH1	Linear Potentiometer on timber strip	-50 to +50 mm
021	XNH1	Linear Potentiometer on timber strip	-50 to +50 mm
022	XSH2	Linear Potentiometer on timber strip	-50 to +50 mm
023	XNH2	Linear Potentiometer on timber strip	-50 to +50 mm
024	XSH3	Linear Potentiometer on timber strip	-100 to +100 mm
025	XNH3	Linear Potentiometer on timber strip	-100 to +100 mm
026	XCWSH1	DW	-100 to +100 mm
027	XCWNH1	DW	-100 to +100 mm
028	XCESH1	DW	-100 to +100 mm
029	XCENH1	DW	-100 to +100 mm
030	XCWSH3	DW	-100 to +100 mm
031	XCWNH3	DW	-100 to +100 mm
032	XCESH3	DW	-100 to +100 mm
033	XCENH3	DW	-100 to +100 mm

Table B.1 – Overview of used sensors with indication of sensors type and maximum stroke. (Cont.)

No. channel	Label	Sensor type	Stroke from zero position
034	SH4R1	Linear Potentiometer	-25 to +25 mm
035	SH4R2	Linear Potentiometer	-25 to +25 mm
036	SH0R3	Linear Potentiometer	-25 to +25 mm
037	SH0R4	Linear Potentiometer	-25 to +25 mm
038	SH4R5	Linear Potentiometer	-25 to +25 mm
039	SH4R6	Linear Potentiometer	-25 to +25 mm
040	SH0R7	Linear Potentiometer	-25 to +25 mm
041	SH0R8	Linear Potentiometer	-25 to +25 mm
042	NH4R9	Linear Potentiometer	-25 to +25 mm
043	NH4R10	Linear Potentiometer	-25 to +25 mm
044	NH0R11	Linear Potentiometer	-25 to +25 mm
045	NH0R12	Linear Potentiometer	-25 to +25 mm
046	NH4R13	Linear Potentiometer	-25 to +25 mm
047	NH4R14	Linear Potentiometer	-25 to +25 mm
048	NH0R15	Linear Potentiometer	-25 to +25 mm
049	NH0R16	Linear Potentiometer	-25 to +25 mm
050	NP01	Linear Potentiometer	-25 to +25 mm
051	NP02	Linear Potentiometer	-25 to +25 mm
052	NP03	Linear Potentiometer	-25 to +25 mm
053	NP04	Linear Potentiometer	-25 to +25 mm
054	NP05	Linear Potentiometer	-25 to +25 mm
055	NP06	Linear Potentiometer	-25 to +25 mm
056	NP07	Linear Potentiometer	-25 to +25 mm
057	NP08	Linear Potentiometer	-25 to +25 mm
058	NP09	Linear Potentiometer	-25 to +25 mm
059	NP10	Linear Potentiometer	-25 to +25 mm
060	NP11	Linear Potentiometer	-25 to +25 mm
061	NP12	Linear Potentiometer	-25 to +25 mm
062	SH4SH1	Linear Potentiometer	-25 to +25 mm
063	SH4SH2	Linear Potentiometer	-25 to +25 mm
064	SH0SH3	Linear Potentiometer	-25 to +25 mm
065	SH0SH4	Linear Potentiometer	-25 to +25 mm
066	NH4SH5	Linear Potentiometer	-25 to +25 mm
067	NH4SH6	Linear Potentiometer	-25 to +25 mm
068	NH0SH7	Linear Potentiometer	-25 to +25 mm
069	NH0SH8	Linear Potentiometer	-25 to +25 mm
070	WROTO1	Linear Potentiometer	-10 to +10 mm
071	WROTI1	Linear Potentiometer	-10 to +10 mm
072	WROTO2	Linear Potentiometer	-10 to +10 mm
073	WROTI2	Linear Potentiometer	-10 to +10 mm
074	WROTO3	Linear Potentiometer	-10 to +10 mm
075	WROTI3	Linear Potentiometer	-10 to +10 mm
076	WROTO4	Linear Potentiometer	-10 to +10 mm
077	WROTI4	Linear Potentiometer	-10 to +10 mm
078	WROTO5	Linear Potentiometer	-10 to +10 mm
079	WROTI5	Linear Potentiometer	-10 to +10 mm
080	WROTO6	Linear Potentiometer	-10 to +10 mm
081	WROTI6	Linear Potentiometer	-10 to +10 mm
082	WROTO7	Linear Potentiometer	-10 to +10 mm
083	WROTI7	Linear Potentiometer	-10 to +10 mm
084	WROTO8	Linear Potentiometer	-10 to +10 mm
085	WROTI8	Linear Potentiometer	-10 to +10 mm

Table B.1 – Overview of used sensors with indication of sensors type and maximum stroke. (Cont.)

No. channel	Label	Sensor type	Stroke from zero position
086	EROTO1	Linear Potentiometer	-10 to +10 mm
087	EROTI1	Linear Potentiometer	-10 to +10 mm
088	EROTO2	Linear Potentiometer	-10 to +10 mm
089	EROTI2	Linear Potentiometer	-10 to +10 mm
090	EROTO3	Linear Potentiometer	-10 to +10 mm
091	EROTI3	Linear Potentiometer	-10 to +10 mm
092	EROTO4	Linear Potentiometer	-10 to +10 mm
093	EROTI4	Linear Potentiometer	-10 to +10 mm
094	EROTO5	Linear Potentiometer	-10 to +10 mm
095	EROTI5	Linear Potentiometer	-10 to +10 mm
096	EROTO6	Linear Potentiometer	-10 to +10 mm
097	EROTI6	Linear Potentiometer	-10 to +10 mm
098	EROTO7	Linear Potentiometer	-10 to +10 mm
099	EROTI7	Linear Potentiometer	-10 to +10 mm
100	EROTO8	Linear Potentiometer	-10 to +10 mm
101	EROTI8	Linear Potentiometer	-10 to +10 mm
110	SK01	Extendable bar with Draw Wire	-25 to +25 mm
111	SK02	Extendable bar with Draw Wire	-25 to +25 mm
112	SK03	Extendable bar with Draw Wire	-25 to +25 mm
113	SK04	Extendable bar with Draw Wire	-25 to +25 mm
114	SK05	Extendable bar with Draw Wire	-25 to +25 mm
115	SK06	Extendable bar with Draw Wire	-25 to +25 mm
116	SK07	Extendable bar with Draw Wire	-25 to +25 mm
117	SK08	Extendable bar with Draw Wire	-25 to +25 mm
118	NK01	Extendable bar with Draw Wire	-25 to +25 mm
119	NK02	Extendable bar with Draw Wire	-25 to +25 mm
120	NK03	Extendable bar with Draw Wire	-25 to +25 mm
121	NK04	Extendable bar with Draw Wire	-25 to +25 mm
122	NK05	Extendable bar with Draw Wire	-25 to +25 mm
123	NK06	Extendable bar with Draw Wire	-25 to +25 mm
124	NK07	Extendable bar with Draw Wire	-25 to +25 mm
125	NK08	Extendable bar with Draw Wire	-25 to +25 mm
126	SBK01	Extendable bar with Draw Wire	-25 to +25 mm
127	SBK02	Extendable bar with Draw Wire	-25 to +25 mm
128	SBK03	Extendable bar with Draw Wire	-25 to +25 mm
129	SBK04	Extendable bar with Draw Wire	-25 to +25 mm
130	NBK01	Extendable bar with Draw Wire	-25 to +25 mm
131	NBK02	Extendable bar with Draw Wire	-25 to +25 mm
132	NBK03	Extendable bar with Draw Wire	-25 to +25 mm
133	NBK04	Extendable bar with Draw Wire	-25 to +25 mm
134	SH01	Linear Potentiometer on steel bar	-25 to +25 mm
135	SH02	Linear Potentiometer on steel bar	-25 to +25 mm
136	SH03	Linear Potentiometer on steel bar	-25 to +25 mm
137	SH04	Linear Potentiometer on steel bar	-25 to +25 mm
138	SH05	Linear Potentiometer on steel bar	-25 to +25 mm
139	SH06	Linear Potentiometer on steel bar	-25 to +25 mm
140	SH07	Linear Potentiometer on steel bar	-25 to +25 mm
141	SH08	Linear Potentiometer on steel bar	-25 to +25 mm
142	NH01	Linear Potentiometer on steel bar	-25 to +25 mm
143	NH02	Linear Potentiometer on steel bar	-25 to +25 mm
144	NH03	Linear Potentiometer on steel bar	-25 to +25 mm
145	NH04	Linear Potentiometer on steel bar	-25 to +25 mm
146	NH05	Linear Potentiometer on steel bar	-25 to +25 mm
147	NH06	Linear Potentiometer on steel bar	-25 to +25 mm
148	NH07	Linear Potentiometer on steel bar	-25 to +25 mm
149	NH08	Linear Potentiometer on steel bar	-25 to +25 mm

Table B.1 – Overview of used sensors with indication of sensors type and maximum stroke. (Cont.)

No. channel	Label	Sensor type	Stroke from zero position
150	SF01	Linear Potentiometer on steel bar	-25 to +25 mm
151	SF02	Linear Potentiometer on steel bar	-25 to +25 mm
152	SF03	Linear Potentiometer on steel bar	-25 to +25 mm
153	SF04	Linear Potentiometer on steel bar	-25 to +25 mm
154	SF05	Linear Potentiometer on steel bar	-25 to +25 mm
155	SF06	Linear Potentiometer on steel bar	-25 to +25 mm
156	SF07	Linear Potentiometer on steel bar	-25 to +25 mm
157	NF01	Linear Potentiometer on steel bar	-25 to +25 mm
158	NF02	Linear Potentiometer on steel bar	-25 to +25 mm
159	NF03	Linear Potentiometer on steel bar	-25 to +25 mm
160	NF04	Linear Potentiometer on steel bar	-25 to +25 mm
161	NF05	Linear Potentiometer on steel bar	-25 to +25 mm
162	NF06	Linear Potentiometer on steel bar	-25 to +25 mm
163	NF07	Linear Potentiometer on steel bar	-25 to +25 mm
164	XNFRH4	Linear Potentiometer on timber strip	-25 to +25 mm
165	XSFRH4	Linear Potentiometer on timber strip	-25 to +25 mm
166	XSFRH2	Linear Potentiometer on timber strip	-10 to +10 mm
167	XNFRH2	Linear Potentiometer on timber strip	-10 to +10 mm
168	YFRH4	Linear Potentiometer on timber strip	-10 to +10 mm
169	YFRH2	Linear Potentiometer on timber strip	-10 to +10 mm
176	SXS	Linear Potentiometer (control)	-100 to +100 mm
177	SXN	Linear Potentiometer (control)	-100 to +100 mm
178	YSWH3	laser with 'reflector'	-25 to +25 mm
179	YSEH3	laser with 'reflector'	-25 to +25 mm
180	YSEH1	laser with 'reflector'	-25 to +25 mm
181	YSWH1	laser with 'reflector'	-25 to +25 mm
182	YNWH3	laser with 'reflector'	-25 to +25 mm
183	YNEH3	laser with 'reflector'	-25 to +25 mm
184	YNWH1	laser with 'reflector'	-25 to +25 mm
185	YNEH1	laser with 'reflector'	-25 to +25 mm
186	YNWH4	laser with 'reflector'	-50 to +50 mm
187	YNEH4	laser with 'reflector'	-50 to +50 mm
188	YNWH2	laser with 'reflector'	-50 to +50 mm
189	YNEH2	laser with 'reflector'	-50 to +50 mm

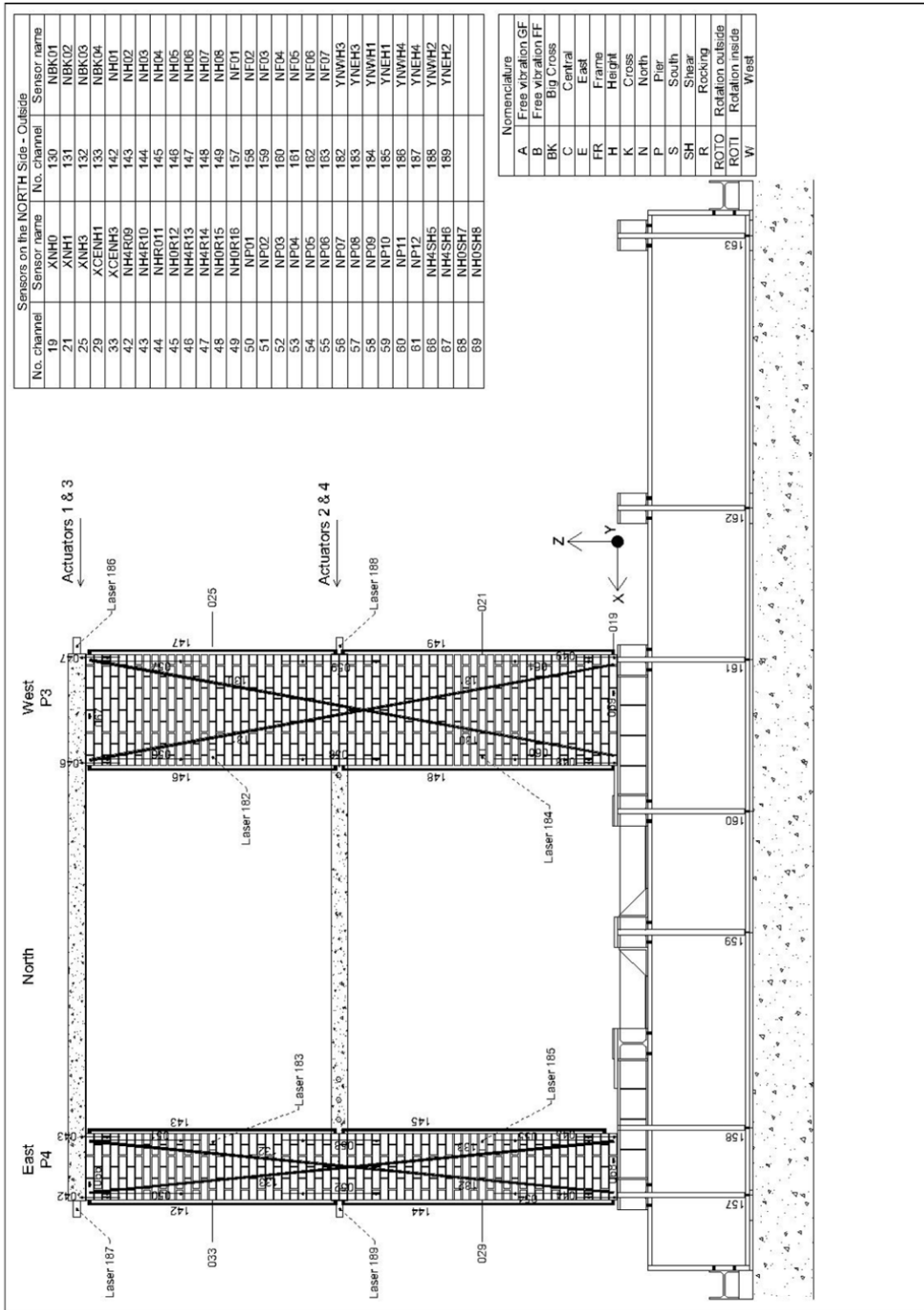


Figure B.1 – Measurement system on the north side, outside view.

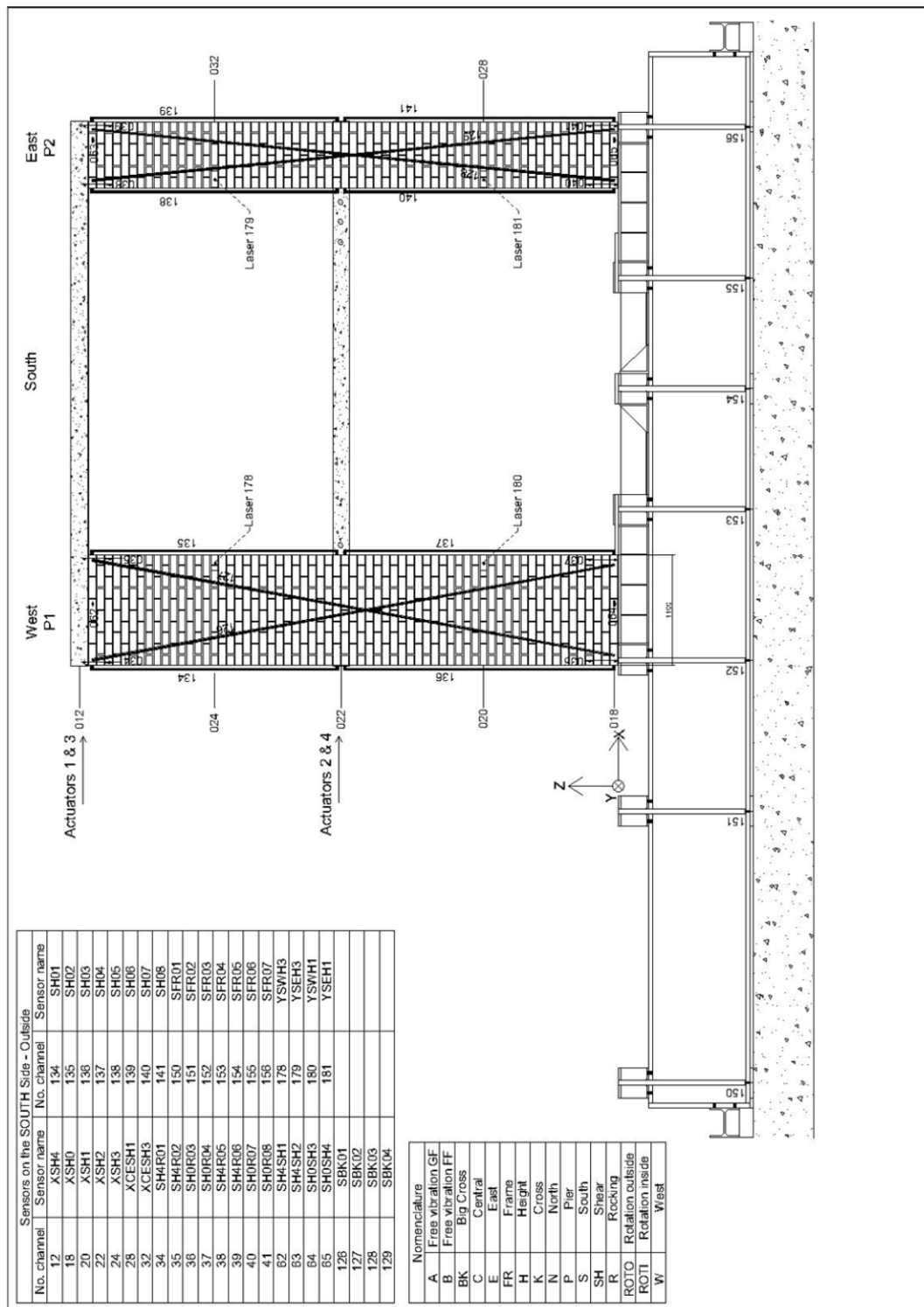


Figure B.2 – Measurement system on the south side, outside view.

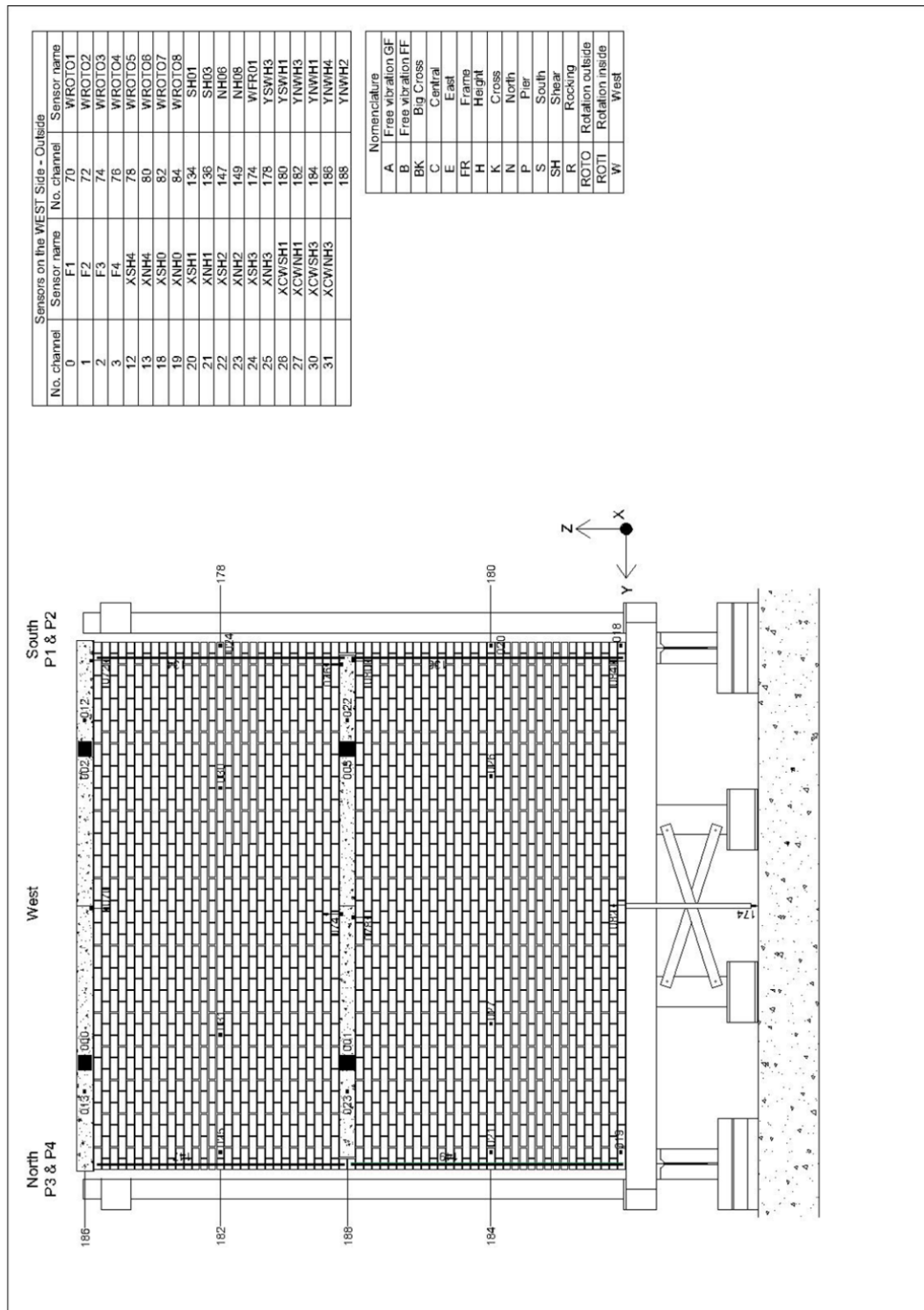


Figure B.3 – Measurement system on the west side, outside view.

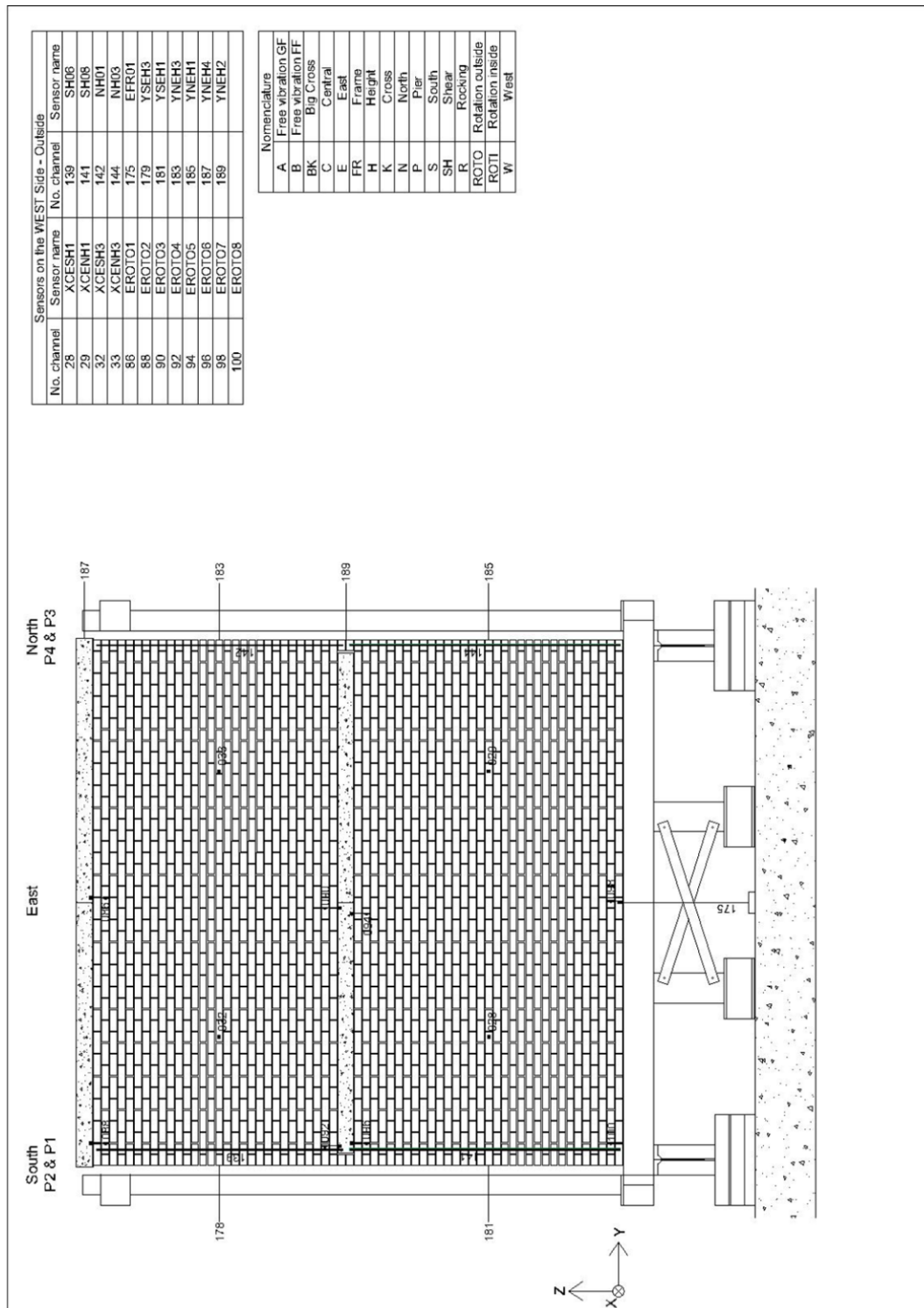


Figure B.4 – Measurement system on the east side, outside view.

C. Material Properties

The material properties of calcium silicate masonry have been determined in two periods [1]. During the first period small-scale samples for material tests (TUD_MAT) and large-scale walls for component tests (TUD_COMP) have been tested. During the second period, the assembled structure (TUD_BUILD) was tested and a limited number of material tests were repeated.

Table C.1 lists the material properties of the calcium silicate masonry for both the first and the second period. Table C.2 lists the properties of the floor-to-wall connection.

Table C.1 – Material properties of calcium silicate masonry tested during the first and second period [1].

Property	Symbol	Unit	First period (MAT/COMP)			Second period (BUILD)			All results		
			Average	St. dev.	C.o.V.	Average	St. dev.	C.o.V.	Average	St. dev.	C.o.V.
Compressive strength of mortar	f_m	MPa	6.59	0.66	0.10	7.24	0.60	0.08	6.69	0.69	0.10
Flexural strength of mortar	f_{mt}	MPa	2.79	0.22	0.08	3.56	0.18	0.05	2.91	0.36	0.12
Flexural strength of masonry unit	f_{bt}	MPa	2.74	0.16	0.06						
Elastic modulus of masonry unit	E_b	MPa	8990	3202	0.36						
Compressive strength of masonry in the direction perpendicular to bed joints	f'_m	MPa	5.93	0.52	0.09	5.76	0.59	0.10	5.84	0.54	0.09
Elastic modulus of masonry in the direction perpendicular to bed joints	E_1	MPa	3174	467	0.15	3340	800	0.24	3264	644	0.20
	E_2	MPa	5091	1774	0.35	4536	1888	0.42	4788	1768	0.37
	E_3	MPa	2746	282	0.10	3005	568	0.19	2887	460	0.16
Poisson ratio of masonry in the direction perpendicular to bed joints	ν		0.14	0.01	0.07	0.18	0.07	0.41	0.16	0.06	0.36
Fracture energy in compression for loading perpendicular to bed joints	G_{fc}	N/m m	31.5	5.1	0.16	21.8	3.6	0.17	26.2	6.6	0.25
Compressive strength of masonry in the direction parallel to bed joints	$f'_{m,h}$	MPa	7.55	0.17	0.02						
Elastic modulus of masonry in the direction parallel to bed joints	$E_{1,h}$	MPa	2212	660	0.30						
	$E_{2,h}$	MPa	3583	1668	0.47						
	$E_{3,h}$	MPa	2081	864	0.42						
Fracture energy in compression for loading parallel to bed joints	$G_{fc,h}$	N/m m	43.4	7.2	0.17						

Table C.1 – Material properties of calcium silicate masonry tested during the first and second period [1].
 (Cont.)

Property	Symbol	Unit	First period (MAT/COMP)			Second period (BUILD)			All results		
			Average	St. dev.	C.o.V.	Average	St. dev.	C.o.V.	Average	St. dev.	C.o.V.
Masonry flexural strength with the moment vector parallel to the bed joints and in the plane of the wall	f_{x1}	MPa	0.21	0.05	0.25						
Masonry flexural strength with the moment vector orthogonal to the bed joint and in the plane of the wall	f_{x2}	MPa	0.76	0.36	0.47						
Masonry flexural strength with the moment vector orthogonal to the plane of the wall	f_{x3}	MPa	0.40	0.09	0.23						
Flexural bond strength	f_w	MPa	0.27	0.12	0.43	0.28	0.08	0.29	0.28	0.10	0.36
Masonry (bed joint) initial shear strength	f_{v0}	MPa	0.14								
Masonry (bed joint) shear friction coefficient	μ		0.43								
Residual masonry (bed joint) initial shear strength	$f_{v0,res}$	MPa	0.03								
Residual masonry (bed joint) shear friction coefficient	μ_{res}		0.54								

Table C.2 – Property of floor-to-wall connection (second period) [1].

Property	Symbol	Unit	Avg.	St. dev.	C.o.V.
Compressive strength of mortar	f_m	MPa	7.24	0.60	0.08
Flexural strength of mortar	f_{mt}	MPa	3.56	0.18	0.05
Cubic compressive strength of concrete	f_{cc}	MPa	74.7	1.7	0.02
Initial shear strength of bed joint between concrete and CS brick	f_{v0}^*	MPa	0.09		
Shear friction coefficient of bed joint between concrete and CS brick	μ^*		0.52		
Residual initial shear strength of bed joint between concrete and CS brick	$f_{v0,res}^*$	MPa	0.00		
Residual shear friction coefficient of bed joint between concrete and CS brick	μ_{res}^*		0.59		

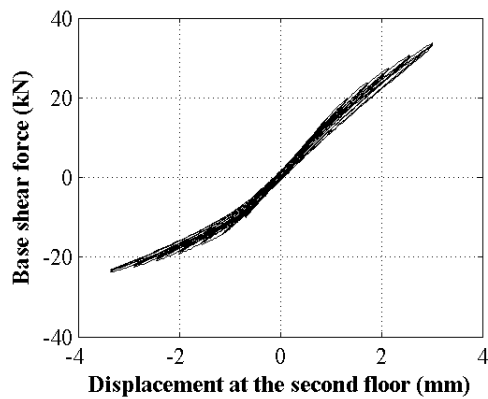
D. Capacity curve per cycle

In this appendix the base shear force-displacement curve are reported for every cycle. In order to compare the overall behaviour of the structure between the cycles, a linear interpolation line is also reported. Only in the elastic phase, the linear interpolation line provides information on the stiffness of the structure.

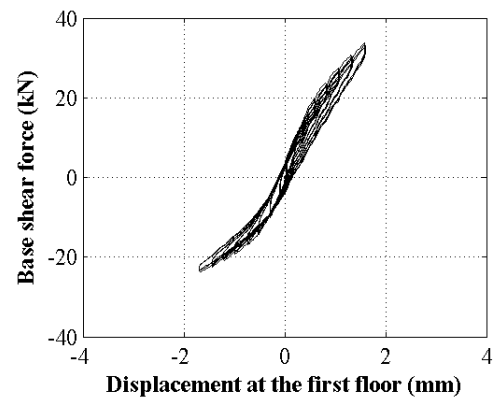
In the initial phase, eight cycles were performed with a minimum displacement of ± 0.3 mm up to a maximum displacement of ± 3.2 mm on average (Table D.1). Figure D.1 shows the force-displacement curve for the entire phase. From Figure D.2 to Figure D.9 the force-displacement curves are reported for every cycle.

Table D.1 – Amplitude of the cycles in the elastic phase.

No. cycle	$d_{2,min}$ (mm)	$d_{2,max}$ (mm)	d_2 (mm)
1	-0.31	0.25	± 0.3
2	-0.70	0.61	± 0.7
3	-1.14	0.94	± 1.0
4	-1.57	1.33	± 1.2
5	-2.01	1.73	± 1.9
6	-2.45	2.14	± 2.3
7	-2.89	2.58	± 2.7
8	-3.36	3.01	± 3.2

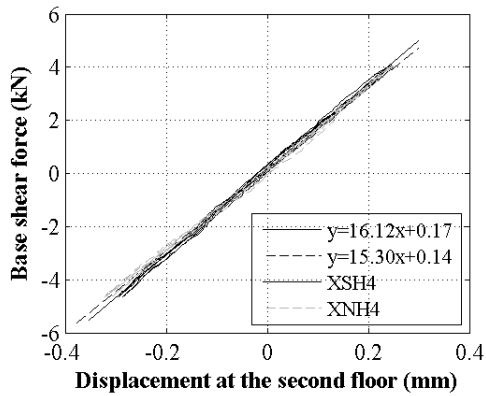


(a)

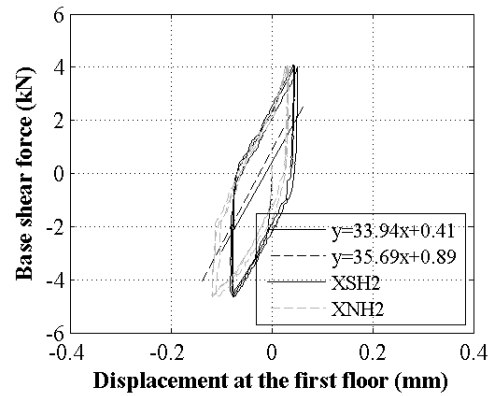


(b)

Figure D.1 – Initial phase: Base shear force vs. displacement at the second (a) and at the first floor level (b).

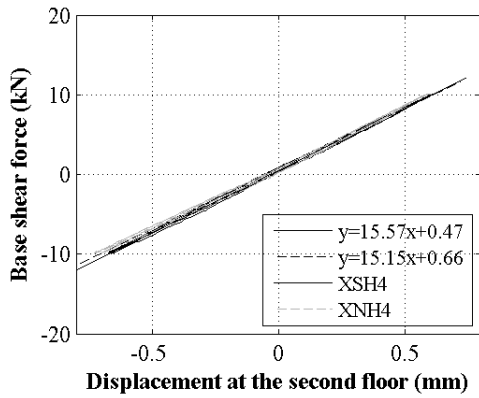


(a)

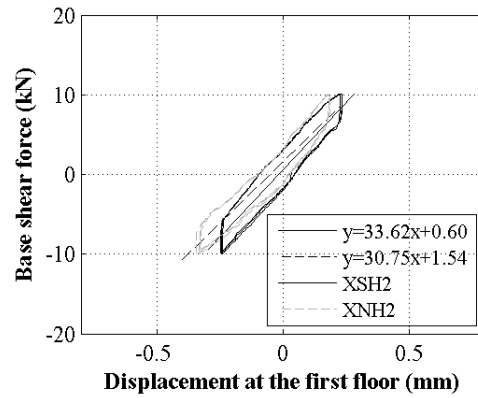


(b)

Figure D.2 – Cycle 1: Base shear force versus displacement at the second (a) and at the first floor level (b).

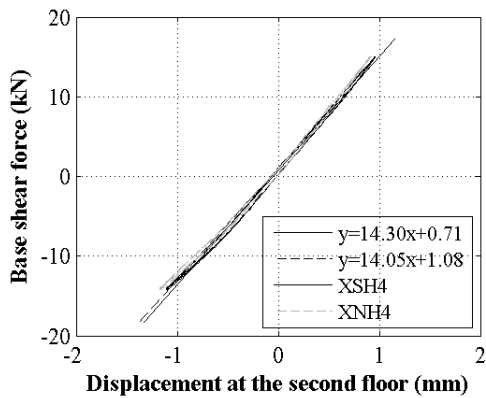


(a)

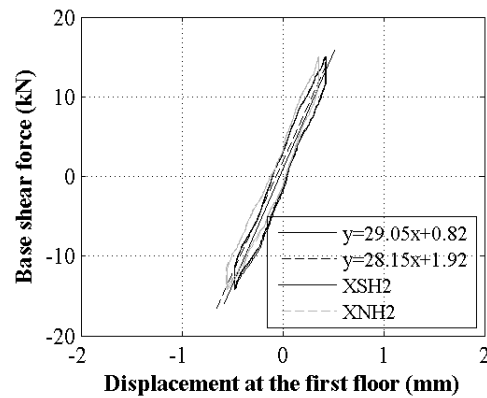


(b)

Figure D.3 – Cycle 2: Base shear force versus displacement at the second (a) and at the first floor level (b).



(a)



(b)

Figure D.4 – Cycle 3: Base shear force versus displacement at the second (a) and at the first floor level (b).

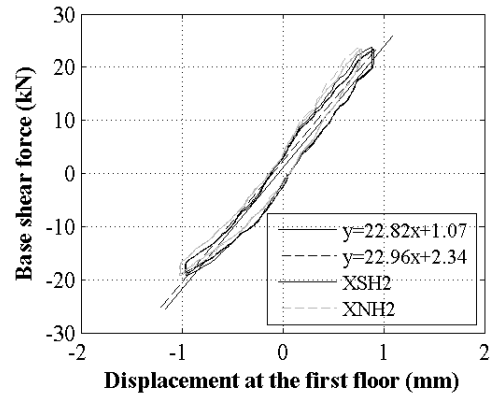
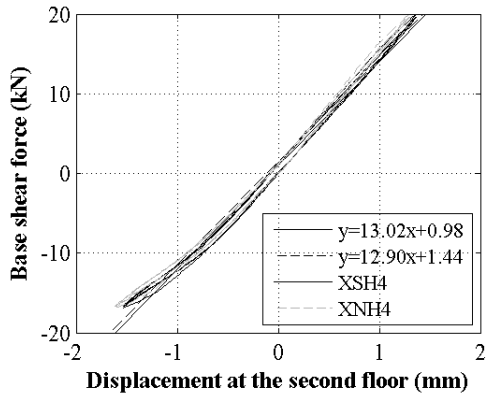


Figure D.5 – Cycle 4: Base shear force versus displacement at the second (a) and at the first floor level (b).

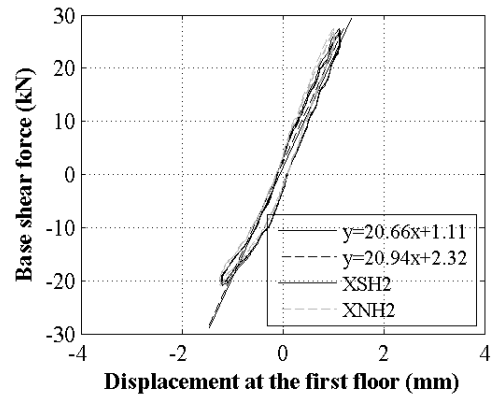
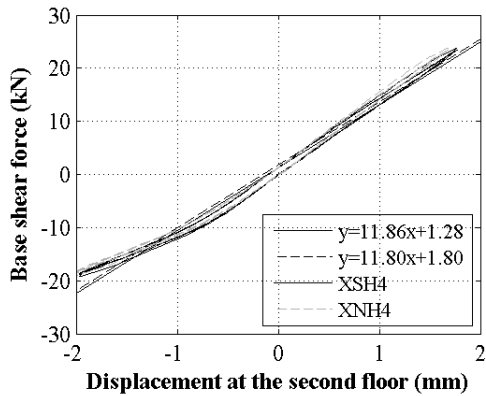


Figure D.6 – Cycle 5: Base shear force versus displacement at the second (a) and at the first floor level (b).

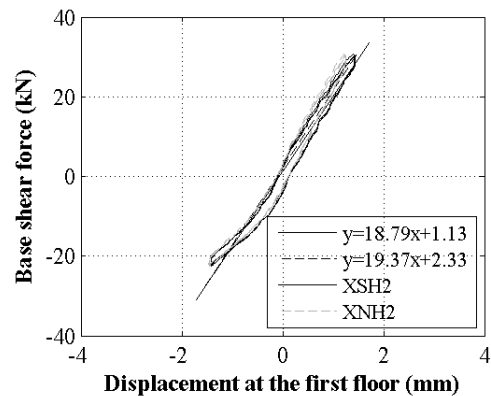
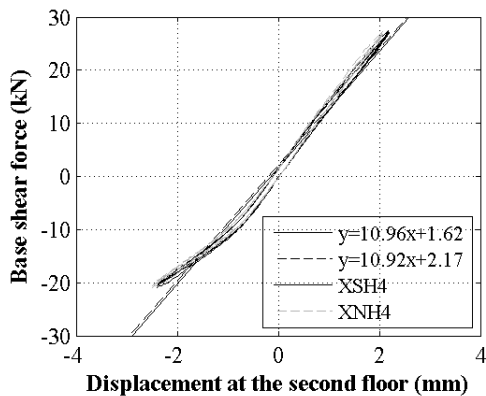
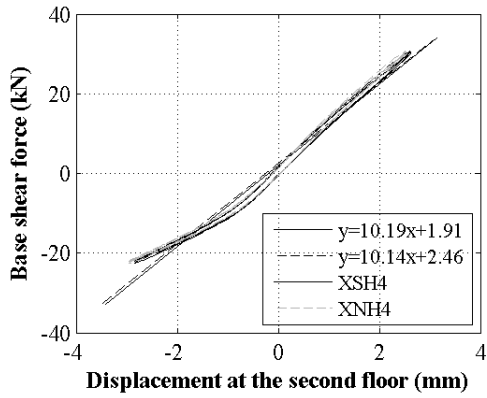
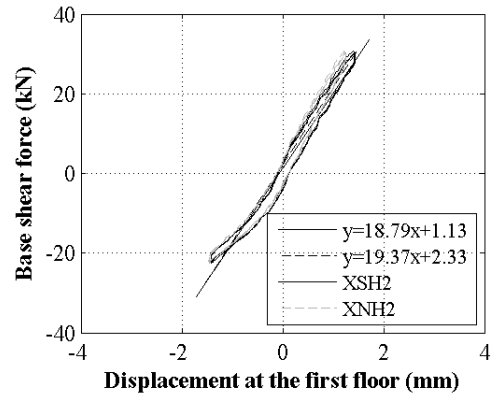


Figure D.7 – Cycle 6: Base shear force versus displacement at the second (a) and at the first floor level (b).

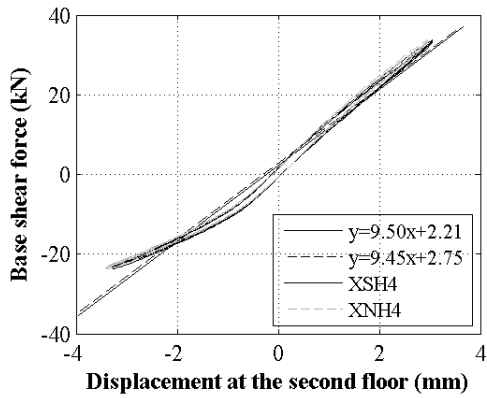


(a)

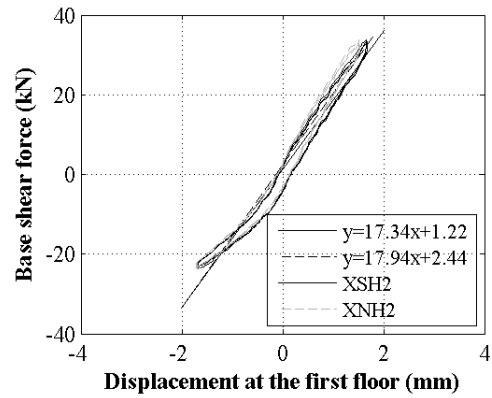


(b)

Figure D.8 – Cycle 7: Base shear force versus displacement at the second (a) and at the first floor level (b).



(a)



(b)

Figure D.9 – Cycle 8: Base shear force versus displacement at the second (a) and at the first floor level (b).

In the pre-peak phase, eight cycles were performed with a minimum displacement of ± 0.7 mm up to a maximum displacement of ± 15.4 mm on average (Table D.2). The first two cycles were a repetition of the second and last cycle performed in the elastic phase. Figure D.10 shows the force displacement curve for the entire phase. From Figure D.11 to Figure D.18 the force-displacement curves are reported for every cycle.

Table D.2 – Amplitude of the cycles in the Pre-peak phase.

No. cycle	$d_{2,min}$ (mm)	$d_{2,max}$ (mm)	d_2 (mm)
2b	-0.68	0.69	± 0.7
7b	-2.85	2.65	± 2.7
9	-3.40	3.17	± 3.2
10	-4.38	4.13	± 4.3
11	-6.01	5.80	± 5.9
12	-9.07	8.96	± 9.0
13	-12.24	12.16	± 12.2
14	-15.49	15.43	± 15.5

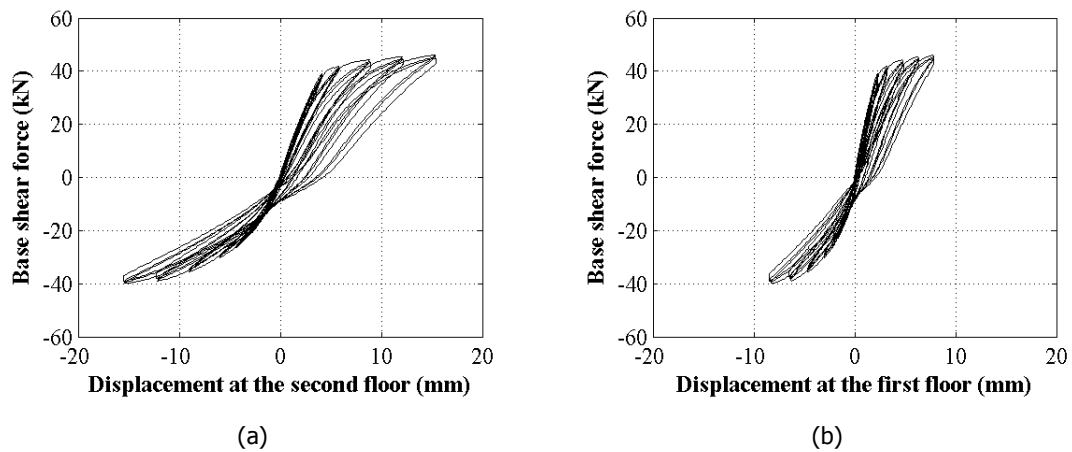
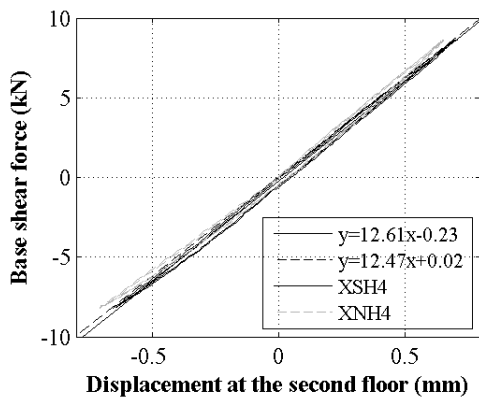
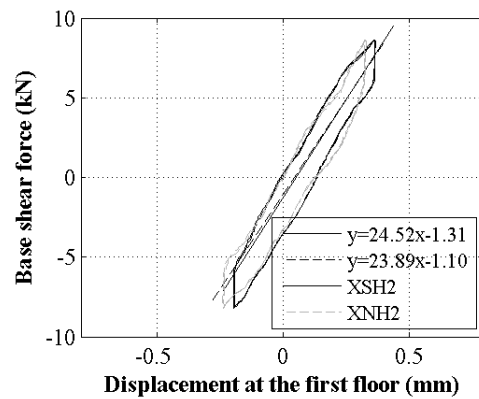


Figure D.10 – Pre-peak phase: Base shear force vs. displacement at the second (a) and at the first floor level (b).

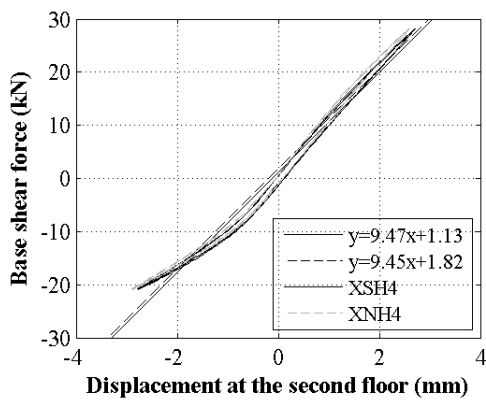


(a)

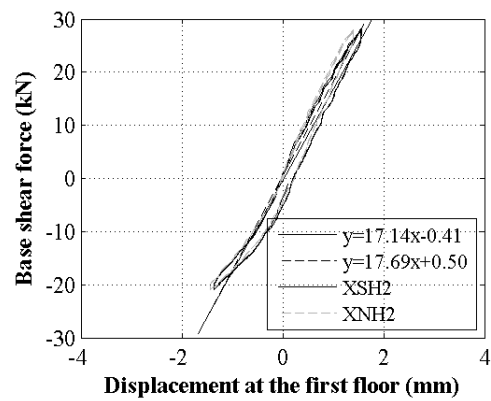


(b)

Figure D.11 – Cycle 2b: Base shear force vs. displacement at the second (a) and at the first floor level (b).

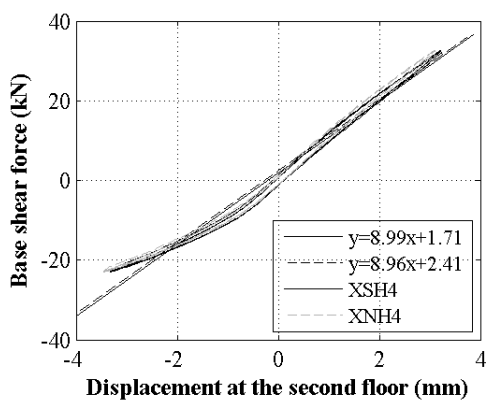


(a)

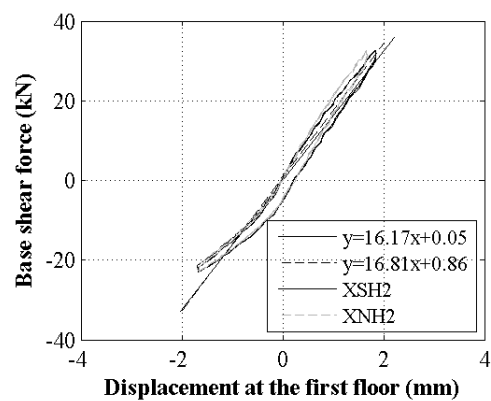


(b)

Figure D.12 – Cycle 7b: Base shear force vs. displacement at the second (a) and at the first floor level (b).

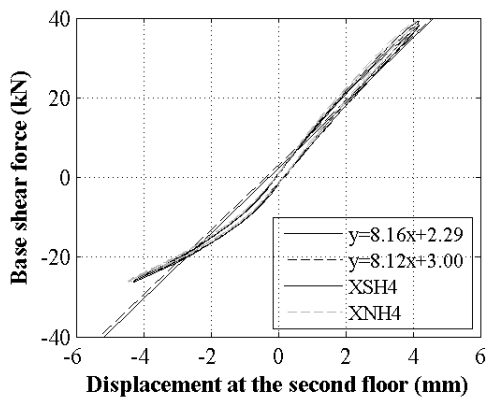


(a)

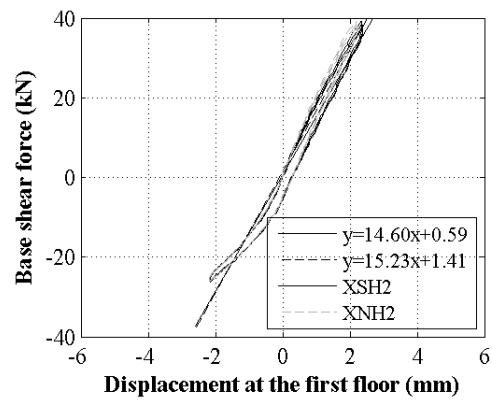


(b)

Figure D.13 – Cycle 9: Base shear force vs. displacement at the second (a) and at the first floor level (b).

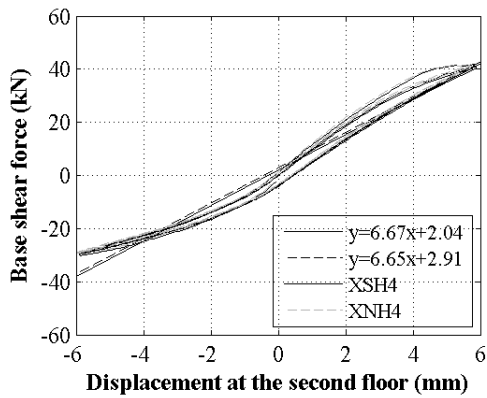


(a)

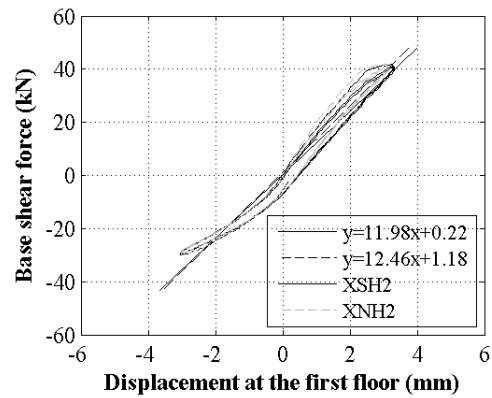


(b)

Figure D.14 – Cycle 10: Base shear force vs. displacement at the second (a) and at the first floor level (b).

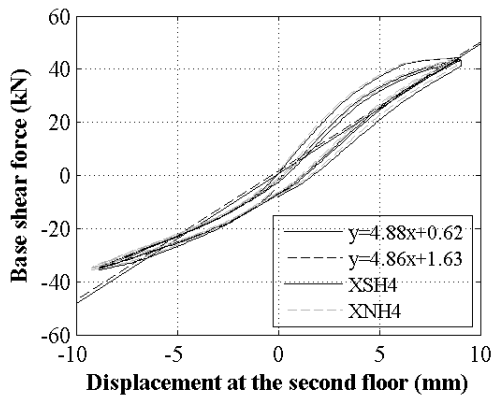


(a)

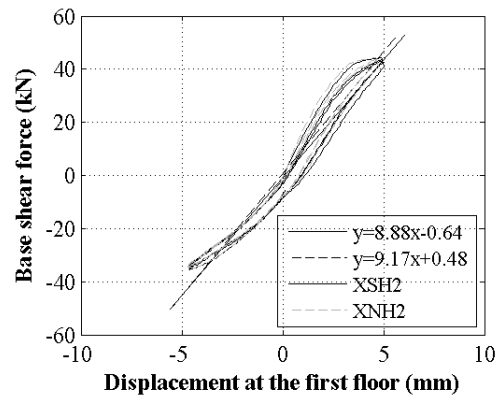


(b)

Figure D.15 – Cycle 11: Base shear force vs. displacement at the second (a) and at the first floor level (b).

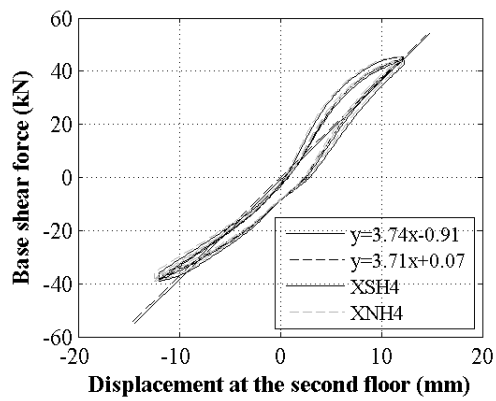


(a)

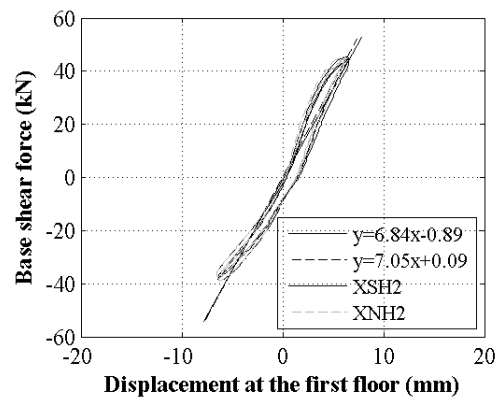


(b)

Figure D.16 – Cycle 12: Base shear force vs. displacement at the second (a) and at the first floor level (b).

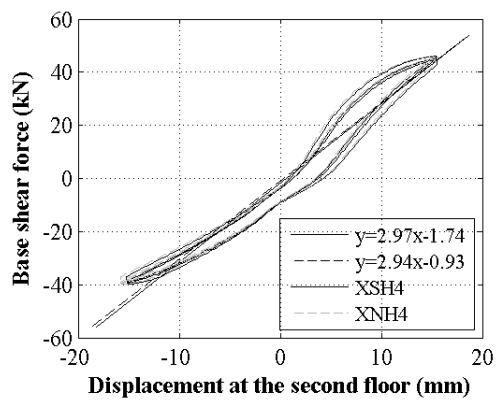


(a)

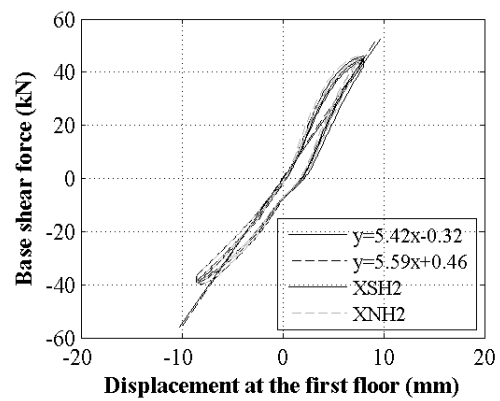


(b)

Figure D.17 – Cycle 13: Base shear force vs. displacement at the second (a) and at the first floor level (b).



(a)



(b)

Figure D.18 – Cycle 14: Base shear force vs. displacement at the second (a) and at the first floor level (b).

In the post-peak phase, ten cycles were performed with a minimum displacement of ± 0.7 mm up to a maximum displacement of -92.3 mm on average (Table D.3). The first two cycles were a repetition of the first and last cycle performed in the pre-peak phase. The last cycle of the post-peak phase consist of half of a run at the maximum displacement of -92.3 mm. Figure D.19 shows the force displacement curve for the entire phase. From Figure D.20 to Figure D.29, the force-displacement curves are reported for every cycle.

Table D.3 – Amplitude of the cycles in the Post-peak phase.

No. cycle	$d_{2,min}$ (mm)	$d_{2,max}$ (mm)	d_2 (mm)
2c	-0.70	0.76	± 0.7
14b	-15.97	16.58	± 15.5
15	-21.30	22.16	± 21.8
16	-26.89	27.91	± 27.4
17	-38.15	39.13	± 38.5
18	-49.31	50.62	± 50.0
19	-60.13	61.82	± 60.0
20	-70.97	73.04	± 72.0
21	-82.31	84.23	± 82.0
22	-92.30*	-	± 92.0

*half of one run.

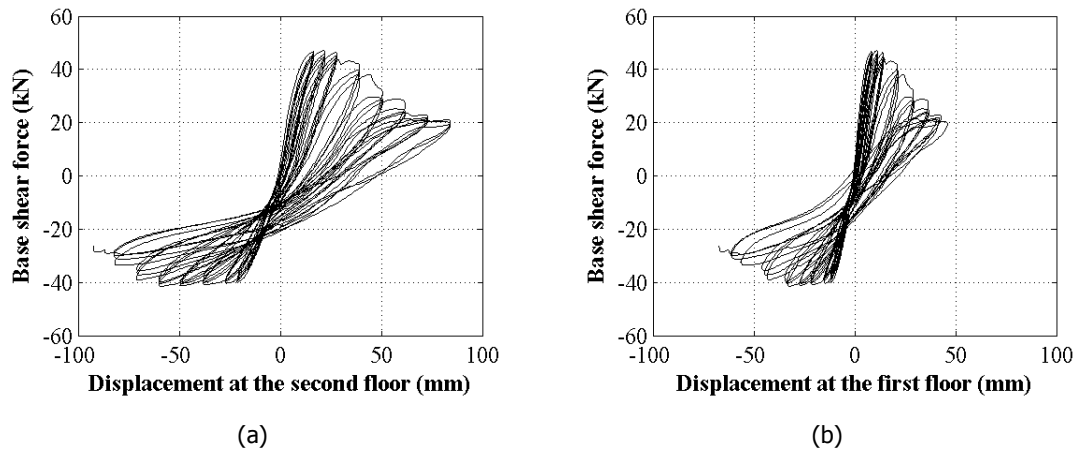
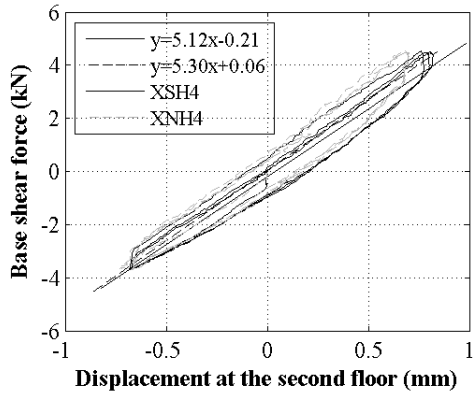
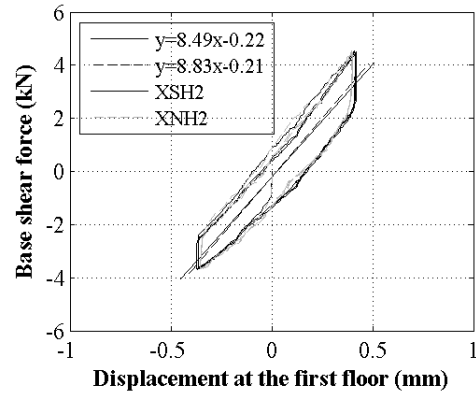


Figure D.19 – Post-peak phase: Base shear force vs. displacement at the second (a) and at the first floor level (b).

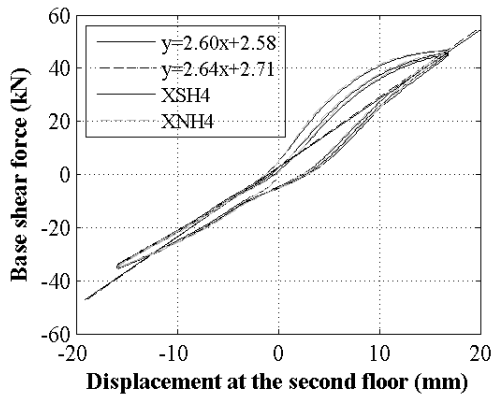


(a)

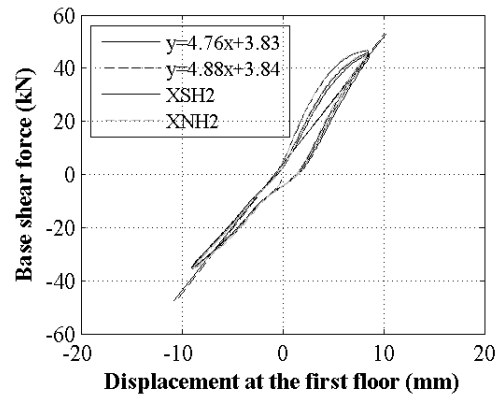


(b)

Figure D.20 – Cycle 2c: Base shear force vs. displacement at the second (a) and at the first floor level (b).

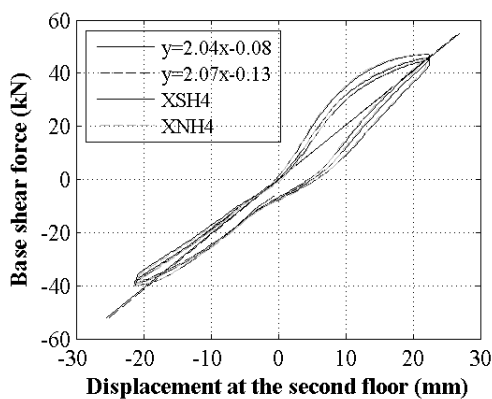


(a)

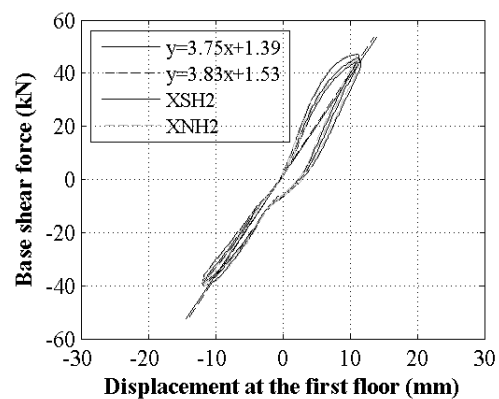


(b)

Figure D.21 – Cycle 14b: Base shear force vs. displacement at the second (a) and at the first floor level (b).

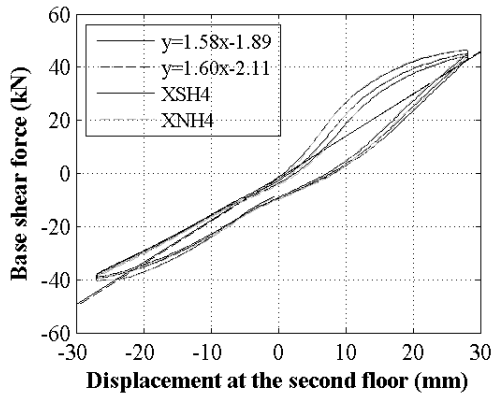


(a)

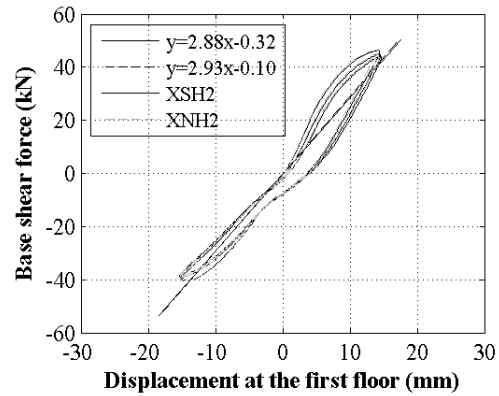


(b)

Figure D.22 – Cycle 15: Base shear force vs. displacement at the second (a) and at the first floor level (b).

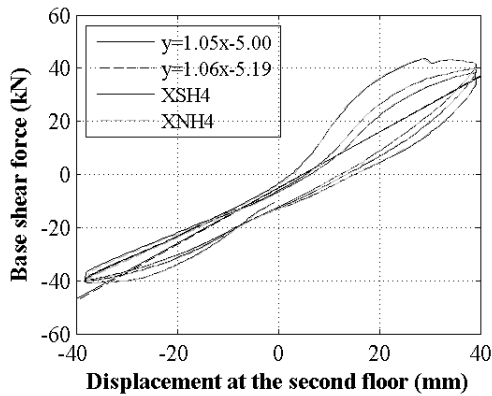


(a)

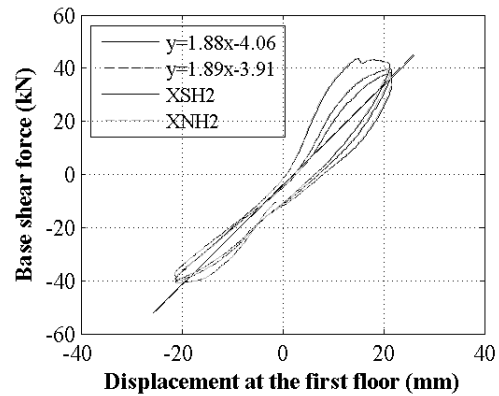


(b)

Figure D.23 – Cycle 16: Base shear force vs. displacement at the second (a) and at the first floor level (b).

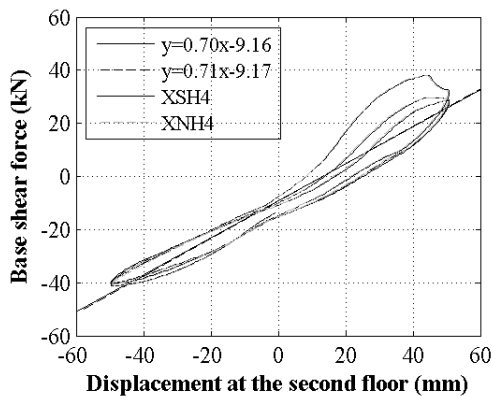


(a)

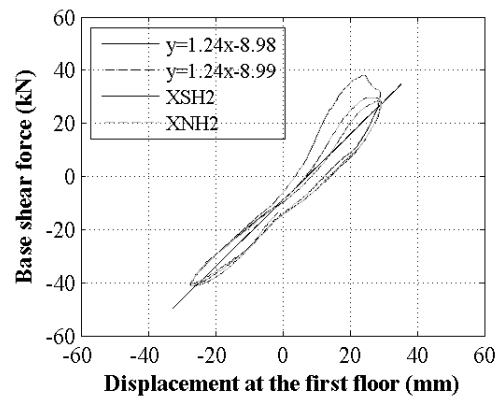


(b)

Figure D.24 – Cycle 17: Base shear force vs. displacement at the second (a) and at the first floor level (b).

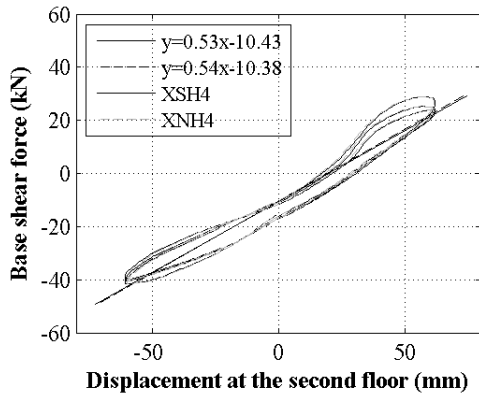


(a)

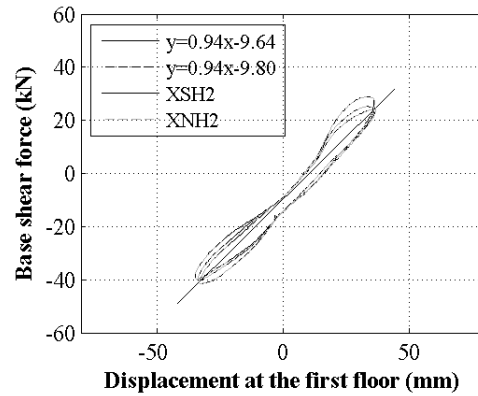


(b)

Figure D.25 – Cycle 18: Base shear force vs. displacement at the second (a) and at the first floor level (b).

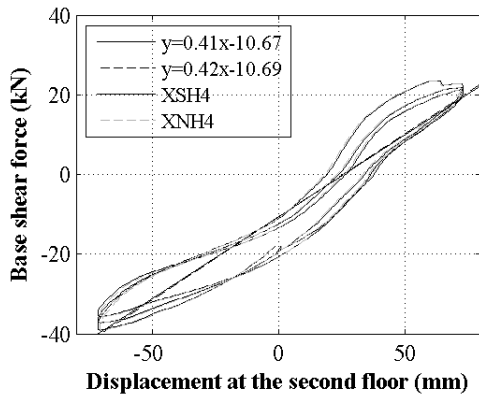


(a)

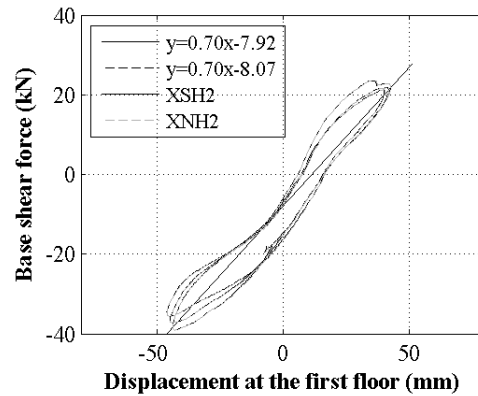


(b)

Figure D.26 – Cycle 19: Base shear force vs. displacement at the second (a) and at the first floor level (b).

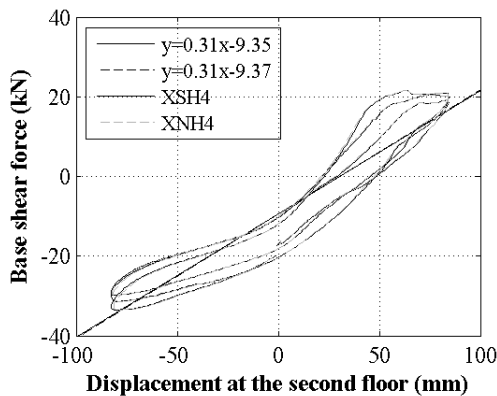


(a)

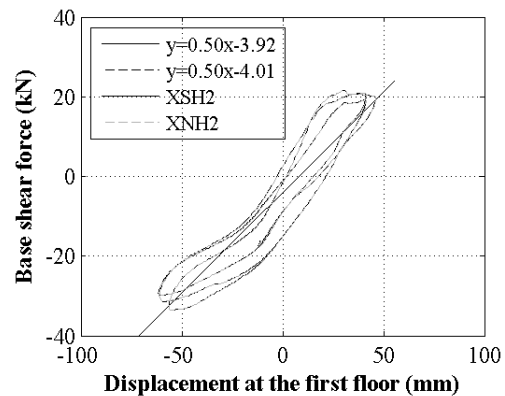


(b)

Figure D.27 – Cycle 20: Base shear force vs. displacement at the second (a) and at the first floor level (b).



(a)



(b)

Figure D.28 – Cycle 21: Base shear force vs. displacement at the second (a) and at the first floor level (b).

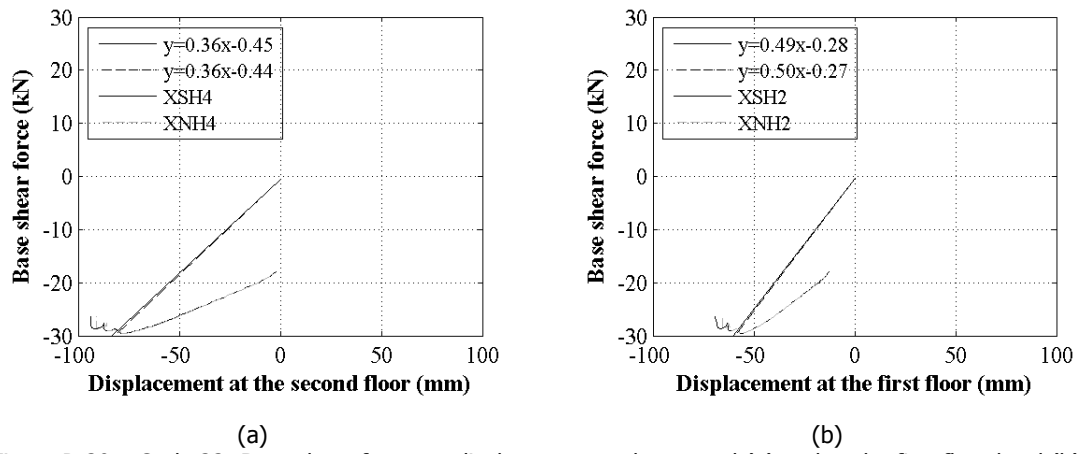


Figure D.29 – Cycle 22: Base shear force vs. displacement at the second (a) and at the first floor level (b).

E. Photographic documentation

In this appendix, the main outcomes of the visual inspection are reported for every cycle.

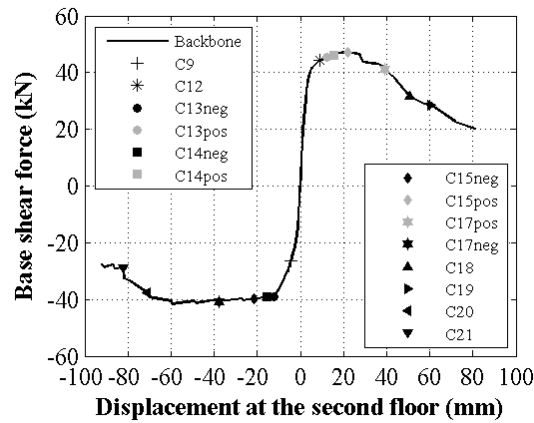


Figure E.1 – Capacity curve and cycles at which the visual inspection was carried out.



Figure E.2 – Pre-peak phase cycle 9 – ground floor: Crack at the bottom of pier P1 (1_C9-GF-P1).

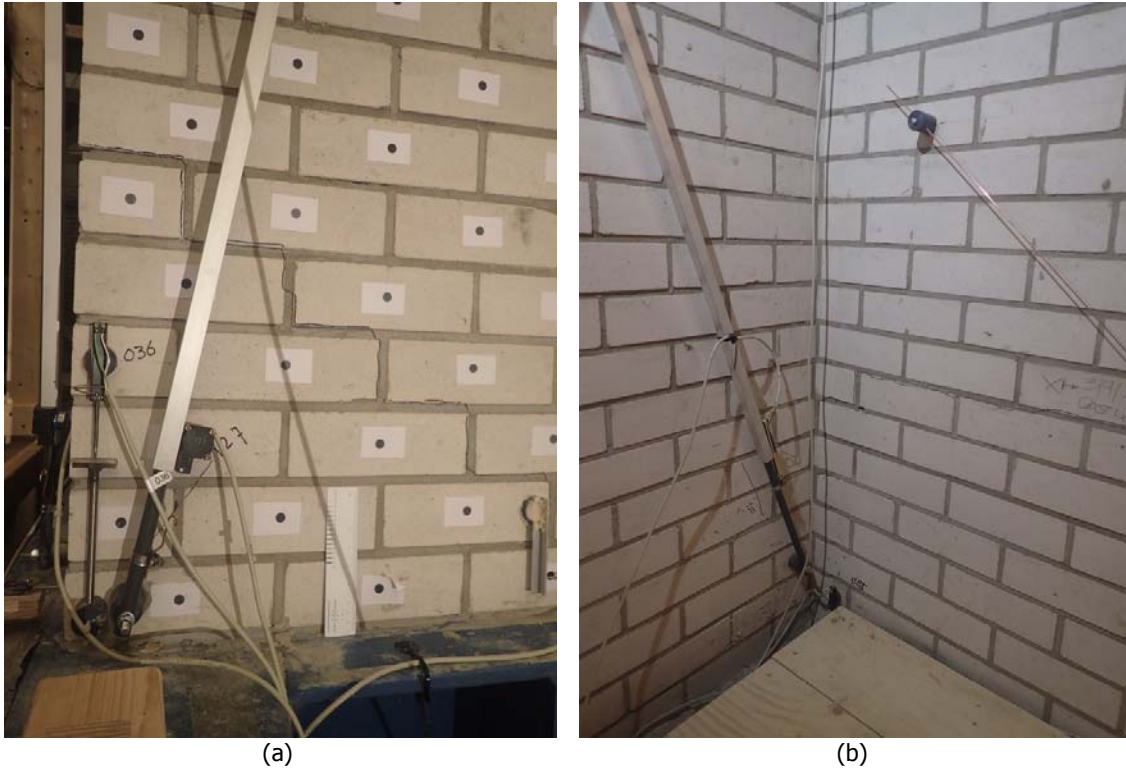


Figure E.3 – Pre-peak phase **cycle 12** – ground floor: (a) Crack at the bottom of pier P1 (2_C12-GF-P1); (b) Crack at the corner between the west wall and pier P1 (3_C12-GF-P1W).



Figure E.4 – Pre-peak phase **cycle 12** – ground floor: (a) Crack at the bottom of pier P2 (4_C12-GF-P1); (b) Crack at the bottom of pier P4 (5_C12-GF-P4).



Figure E.5 – Pre-peak phase **cycle 12** – ground floor: Crack at the bottom of west wall (6_C12-GF-W).



(a)



(b)

Figure E.6 – Pre-peak phase **cycle 13** – ground floor: (a) Crack at the bottom of pier P1 (7_C13-GF-P1); (b) Crack at the bottom of pier P3 (8_C13-GF-P3). Compare with Figure E.2.



(a)



(b)

Figure E.7 – Pre-peak phase **cycle 14 (negative displacement)** – ground floor: (a) Crack at the bottom of pier P1 (9_C14-GF-P1); (b) Crack at the bottom of pier P3 (10_C14-GF-P3). Compare with Figure E.6.



Figure E.8 – Pre-peak phase **cycle 14 (negative displacement)** – ground floor: (a) Crack at the corner between west wall and pier P1 (11_C14-GF-P1W); (b) Crack in pier P2 (12_C14-GF-P2). Compare with Figure E.6.



Figure E.9 – Pre-peak phase **cycle 14 (negative displacement)** – ground floor: Diagonal crack on the east wall at the ground floor (13_C14-GF-W).



Figure E.10 – Pre-peak phase **cycle 14 (negative displacement)** – first floor: (a) Crack between second floor slab and pier P1 (14_C14-FF-P1); (b) Crack between second floor slab and pier P3 (15_C14-FF-P3).



Figure E.11 – Pre-peak phase **cycle 14 (positive displacement)** – first floor: (a) Diagonal cracks on west wall (outside) at the first floor (16_C14-FF-W); (b) Detail of picture (a) (17_C14-FF-W).

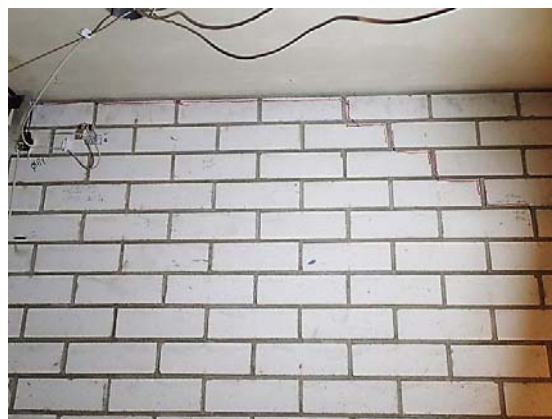


Figure E.12 – Post-peak phase **cycle 15 (negative displacement)** – ground floor: Crack between first floor slab and west wall at corner with pier P1 (18_C15-GF-WP1).



(a)

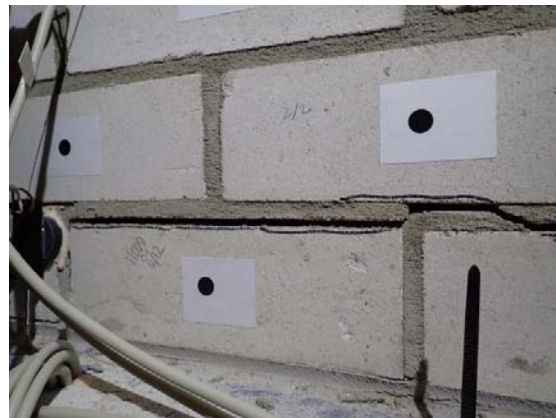


(b)

Figure E.13 – Post-peak phase cycle 15 (negative displacement) – ground floor: (a) Diagonal cracks on pier P1 (outside) at the ground floor (19_C15-GF-P2); (b) Detail of picture (a) (20_C15-GF-P2). Compare with Figure E.7(a).



(a)



(b)

Figure E.14 – Post-peak phase cycle 15 (negative displacement) – ground floor: (a) Crack at the bottom of pier P3 (outside) (21_C15-GF-P3); (b) Detail of picture (a) (22_C15-GF-P3). Compare with Figure E.7(b).

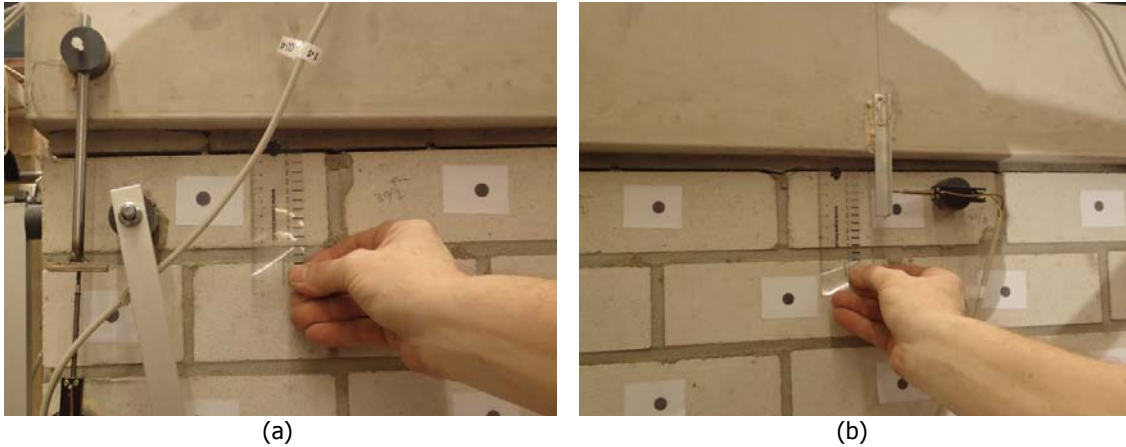


Figure E.15 – Post-peak phase **cycle 15 (negative displacement)** – first floor: (a) Crack between second floor slab and pier P1 (outside) (23_C15-FF-P1); (b) Detail of (a) (24_C15-FF-P1).

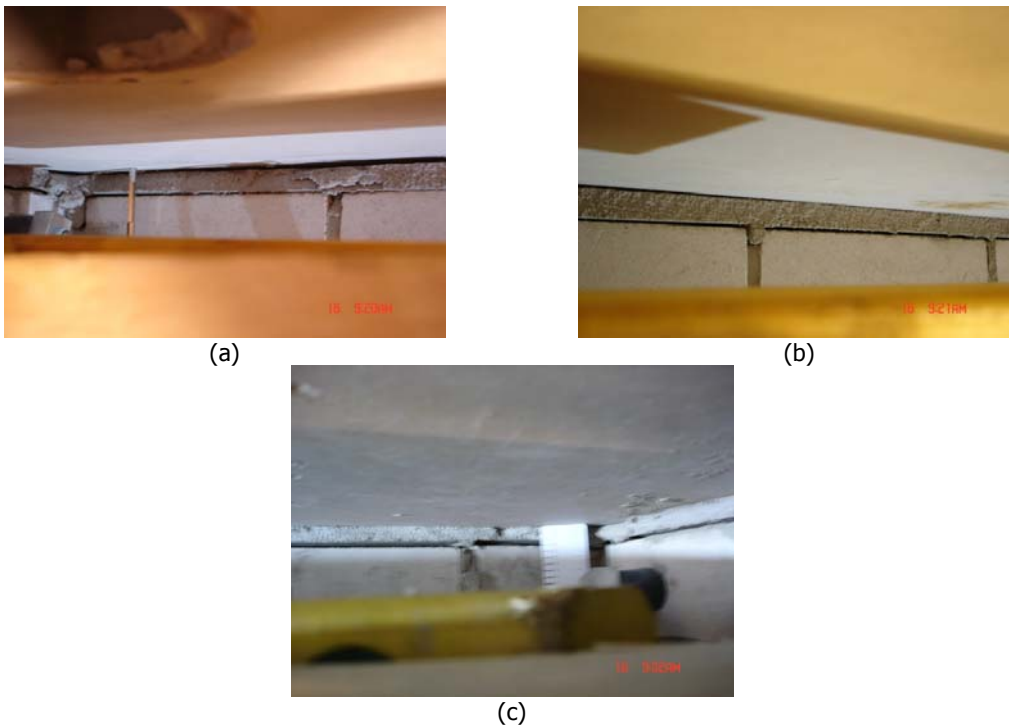


Figure E.16 – Post-peak phase **cycle 15 (negative displacement)** – first floor: Crack between second floor slab and west wall (a) at corner with pier P1 (2_C15-FF-WP1), (b) at the centre (26_C15-FF-W) and (c) at corner with pier P3 (27_C15-FF-WP3).

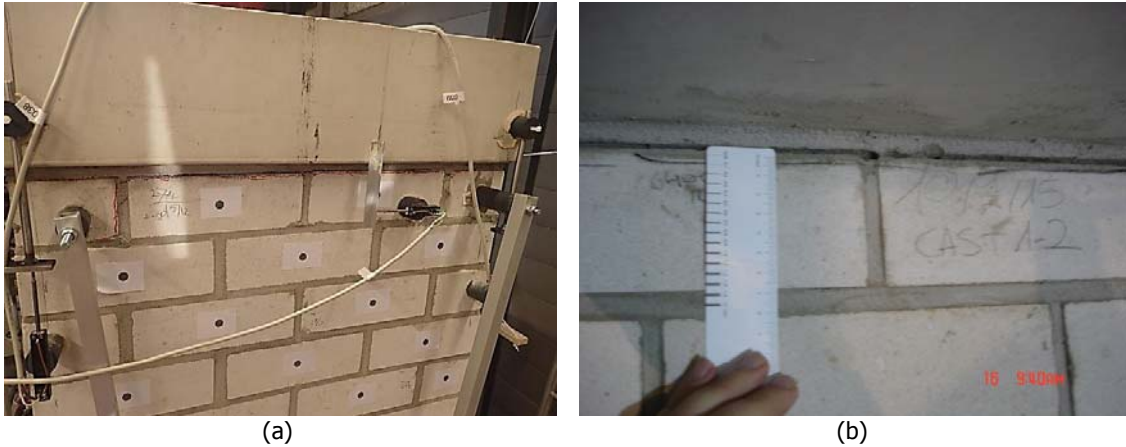


Figure E.17 – Post-peak phase **cycle 15 (positive displacement)** – first floor: (a) Crack between second floor slab pier P2 (28_C15-FF-P2); (b) Detail of (a) (29_C15-FF-P2).



Figure E.18 – Post-peak phase **cycle 15 (positive displacement)** – ground floor: Crack at the corner between west wall and pier P1 (30_C14-GF-P1W). Compare with Figure E.8.

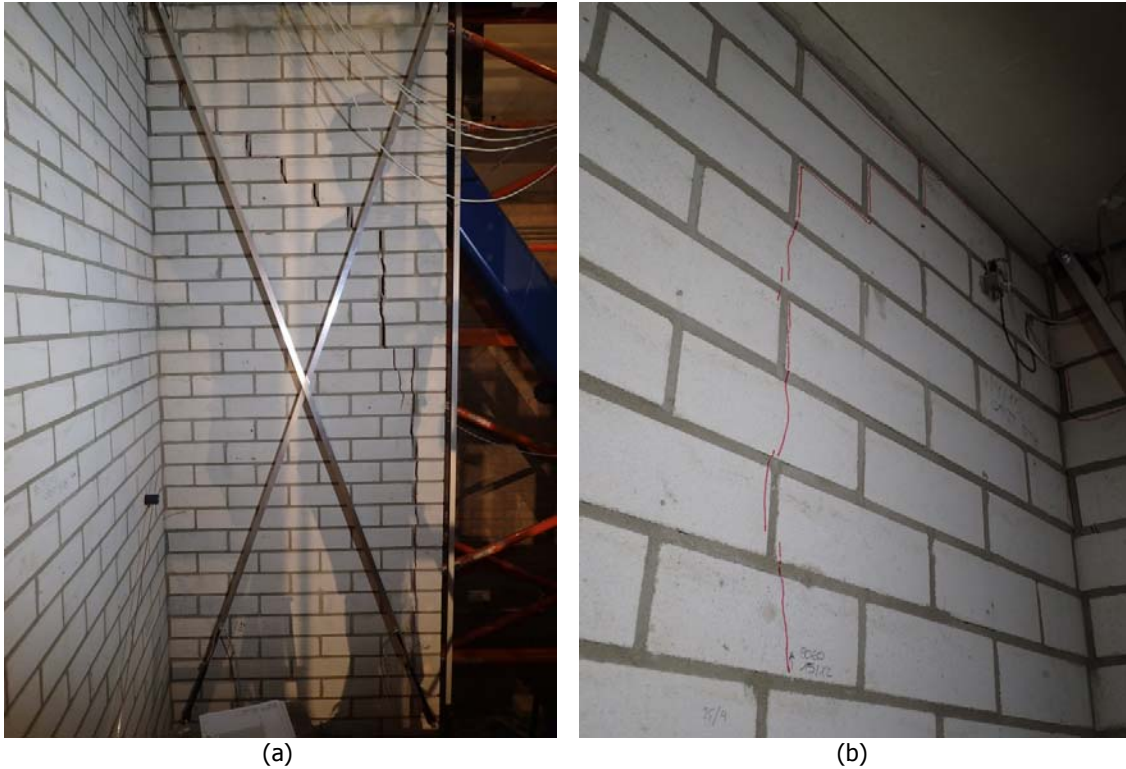


Figure E.19 – Post-peak phase **cycle 17 (negative displacement)** – ground floor: (a) Crack on pier P3 at the ground floor (31_C17-GF-P3); (b) Crack on west wall at the side with pier P3 (32_C17-GF-W).



Figure E.20 – Post-peak phase **cycle 17 (negative displacement)** – ground floor: (a) Diagonal cracks on east wall at the ground floor (33_C17-GF-E); (b) Detail of the left diagonal crack in figure (a) (34_C17-GF-E).

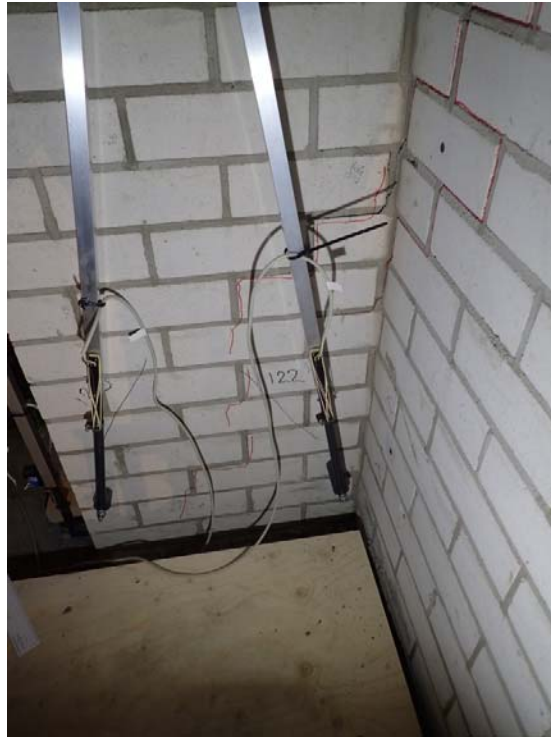


Figure E.21 – Post-peak phase **cycle 17 (negative displacement)** – ground floor: Cracks on pier P4 at the corner with east wall (35_C17_GF_P4E).



(a)



(b)

Figure E.22 – Post-peak phase **cycle 17 (negative displacement)** – first floor: (a) Crack between second floor slab and pier P3 (36_C17-FF-P3); (b) Crack between second floor slab and west wall (37_C17-FF-W). Compare with Figure E.16.



Figure E.23 – Post-peak phase **cycle 17 (negative displacement)** – first floor: (a) Crack between second floor slab and pier P1 (38_C17-FF-P1). Compare with Figure E.15.



(a)



(b)

Figure E.24 – Post-peak phase **cycle 17 (negative displacement)** – first floor: (a) Diagonal crack on west wall on the side of pier P1 at the first floor (39_C17-FF-P3); (b) Crack between first floor slab and west wall at the centre (40_C17-FF-W).

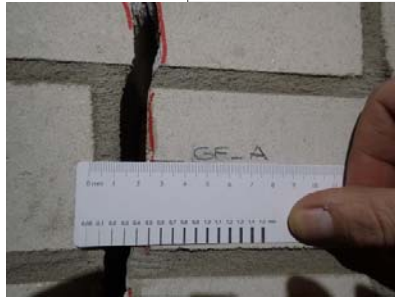
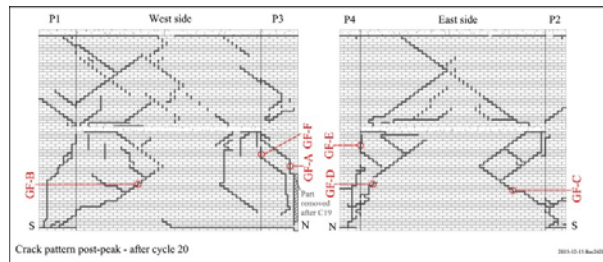


(a)



(b)

Figure E.25 – Post-peak phase **cycle 17 (positive displacement)** – ground floor: (a) Diagonal crack at the bottom of pier P2 at the ground floor (41_C17-GF-P2); (b) Crack on pier P3 at the side with west wall (42_C17-GF-P3).



(a) GF_A



(b) GF_B



(c) GF_C



(d) GF_D

Figure E.26 – Post-peak phase cycle 17 (positive displacement) – Crack width.

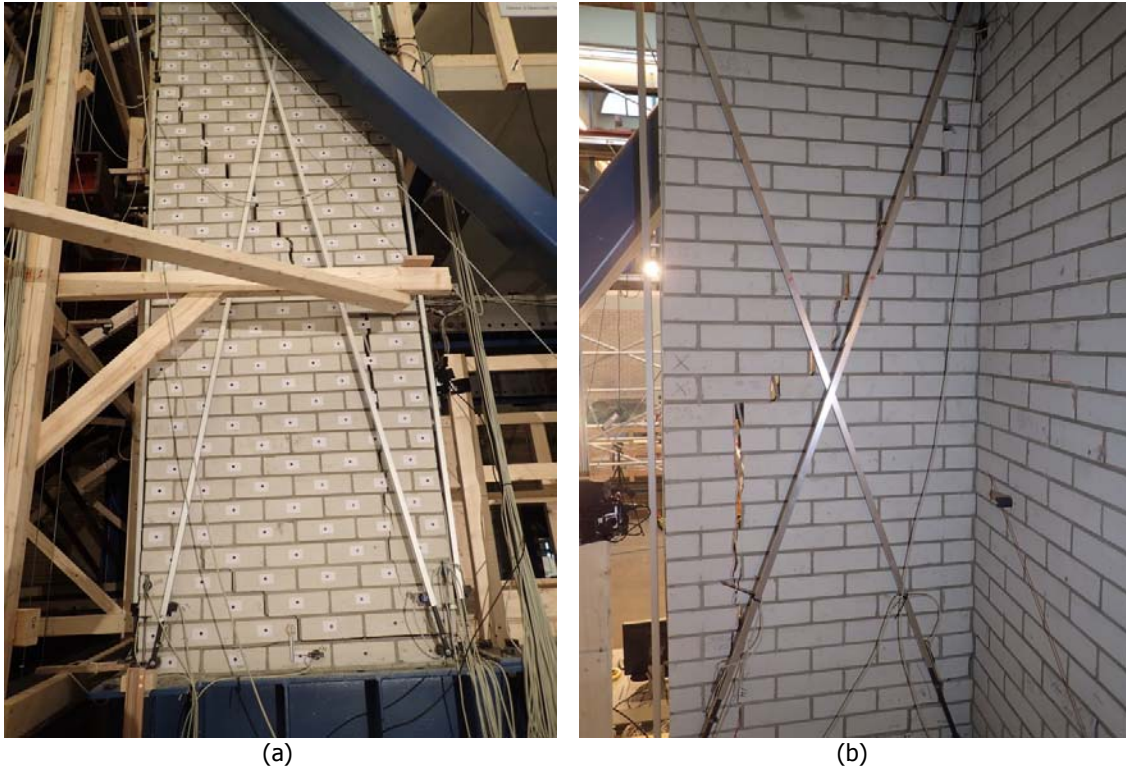


Figure E.27 – Post-peak phase **cycle 18** – ground floor - Diagonal crack on pier P1 at the ground floor (a): Outside (43_C18-GF-P1); (b) Inside (44_C18-GF-P1).

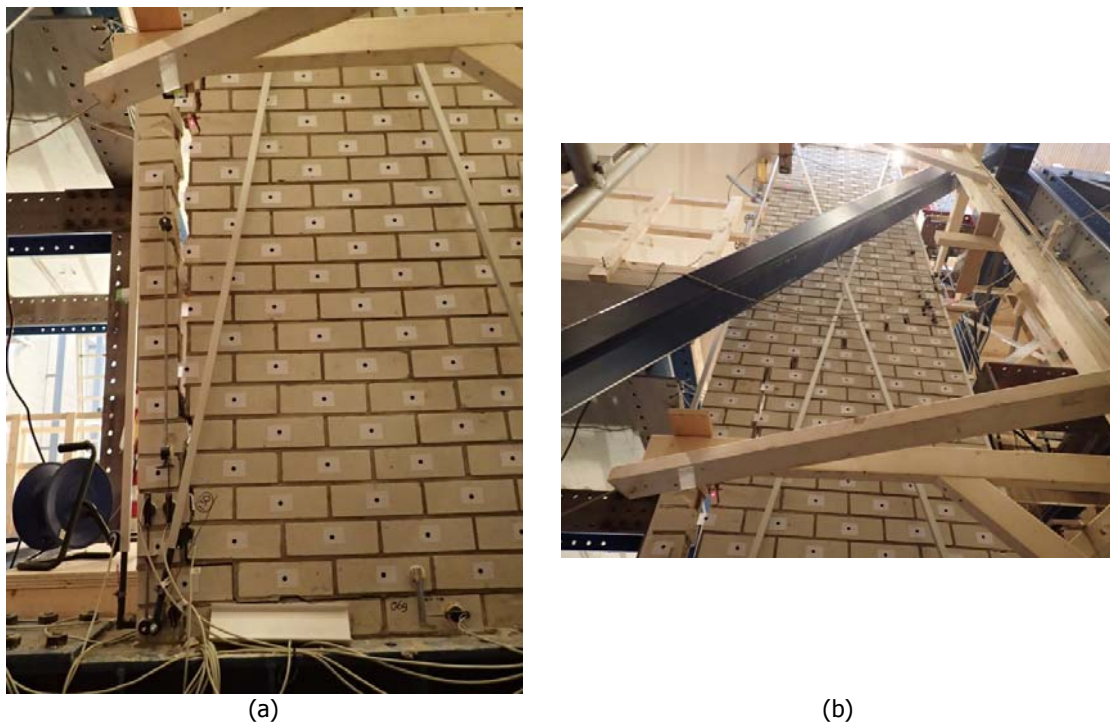


Figure E.28 – Post-peak phase **cycle 18** – ground floor - Diagonal crack on pier P3 at the ground floor (outside): (a) Bottom part (45_C18-GF-P3); (b) Upper part (46_C18-GF-P3). Compare with Figure E.19(a).

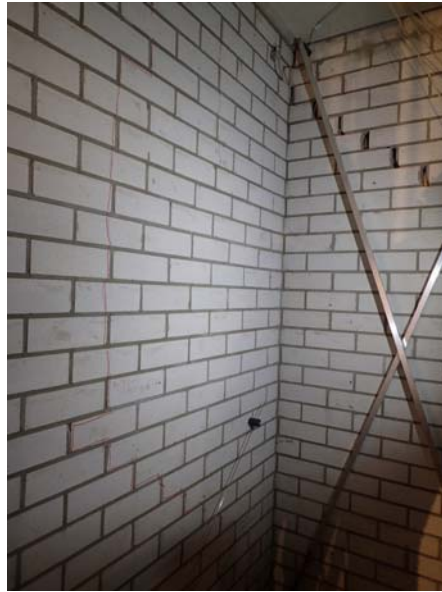
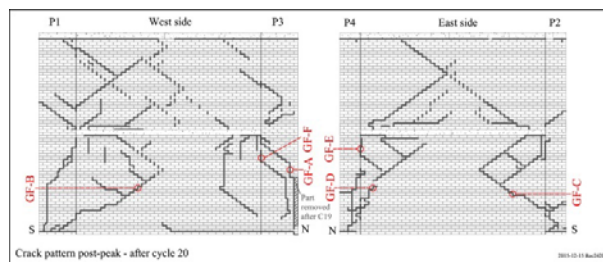


Figure E.29 – Post-peak phase cycle 18 – ground floor: Vertical crack on west wall at the side with pier P3 (47_C18-GF-WP3). Compare upper part of the photo with Figure E.19(b).



(a) GF_A



(b) GF_B



(c) GF_C



(d) GF_D

Figure E.30 – Post-peak phase cycle 18 – Crack width. Compare with Figure E.26.

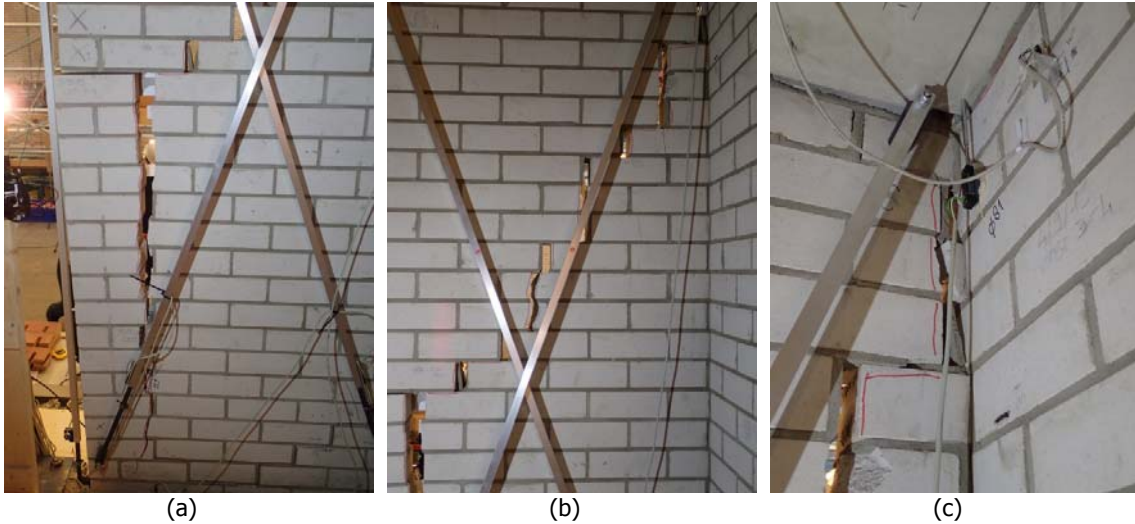


Figure E.31 – Post-peak phase **cycle 19** – ground floor – Vertical/diagonal crack on pier P1 at ground floor: (a) Bottom (48_C19-GF-P1); (b) Centre (49_C19-GF-P1); (c) Top (50_C19-GF-P1). Compare with Figure E.20.

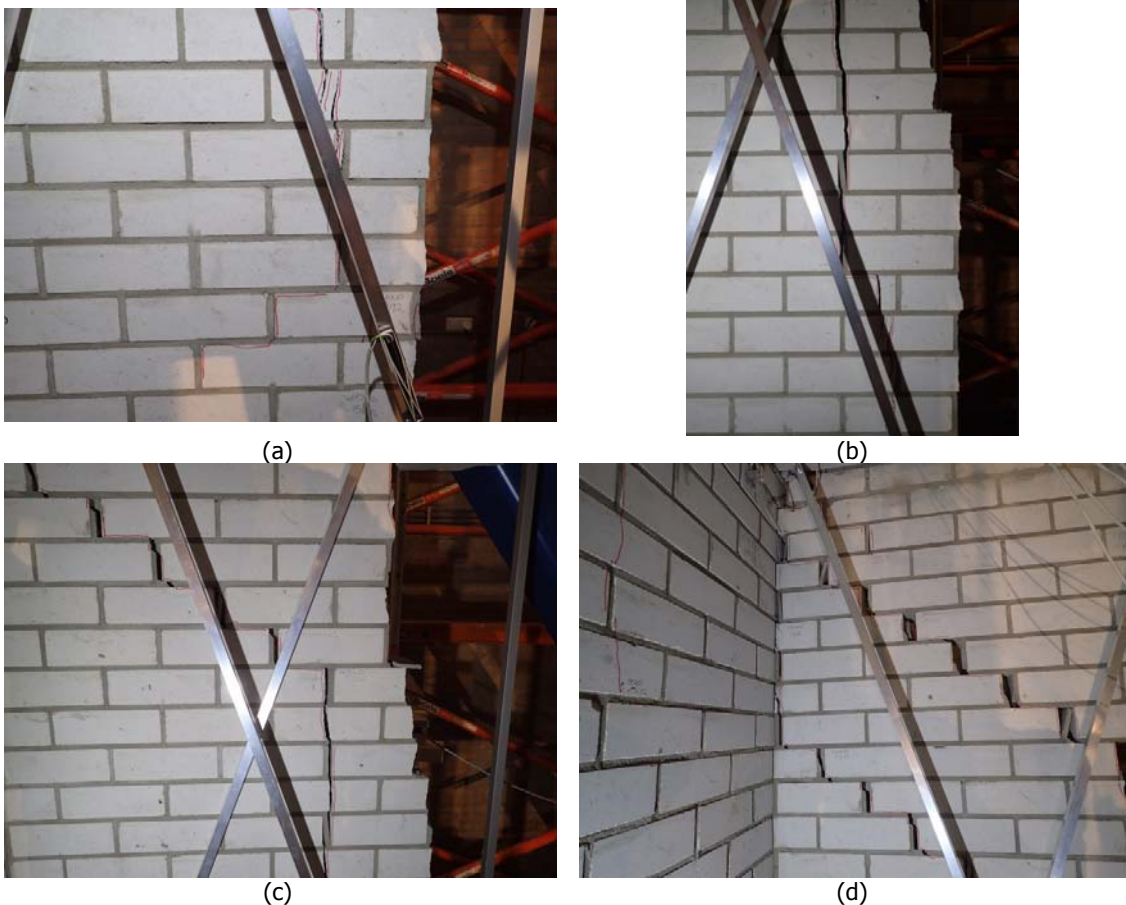


Figure E.32 – Post-peak phase **cycle 19** – ground floor – Vertical/diagonal crack on pier P3 at the ground floor: (a) Lower part (51_C19-GF-P3); (b) Mid-lower part (52_C19-GF-P3); (c) Mid-upper part (53_C19-GF-P3); (d) Upper part (54_C19-GF-P3). Compare with Figure E.28.

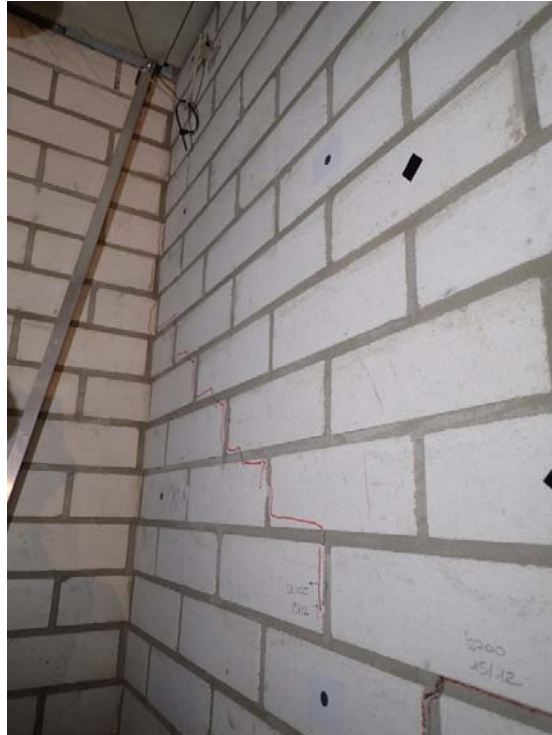
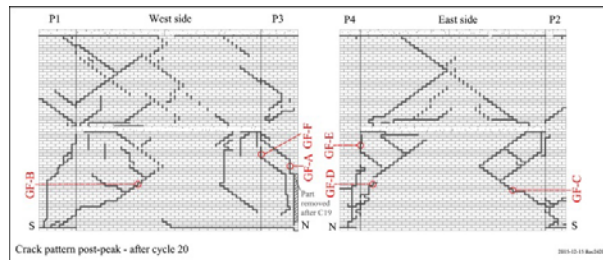


Figure E.33 – Post-peak phase cycle 19 – ground floor: Crack on east wall at the side with pier P4 at the ground floor (55_C19-GF-WP4).



Figure E.34 – Post-peak phase cycle 19 – first floor: Crack pier P3 at the first floor (56_C19-FF-P3).



(a) GF_B



(b) GF_C

Figure E.35 – Post-peak phase **cycle 19** – Crack width. Compare with Figure E.30..



(a)

(b)

(c)

Figure E.36 – Post-peak phase **cycle 20** – Vertical/diagonal crack on pier P1 (outside): (a) Overview (57_C20-P1); (b) Detail at the first floor slab (58_C20-GF-P1); (c) Detail at the second floor slab (59_C20-FF-P1). Compare with Figure E.31.



(a)



(b)

Figure E.37 – Post-peak phase **cycle 20** - Crack on pier P4: (a) Outside (60_C20-GF-P4); (b) Inside (61_C20-GF-P4). Compare with Figure E.21.



(a)



(b)

Figure E.38 – Post-peak phase **cycle 20** - Crack on east wall (outside): (a) At the side with pier P2 (62_C20-GF-EP2); (b) At the side with pier P4 (63_C20-GF-EP4).

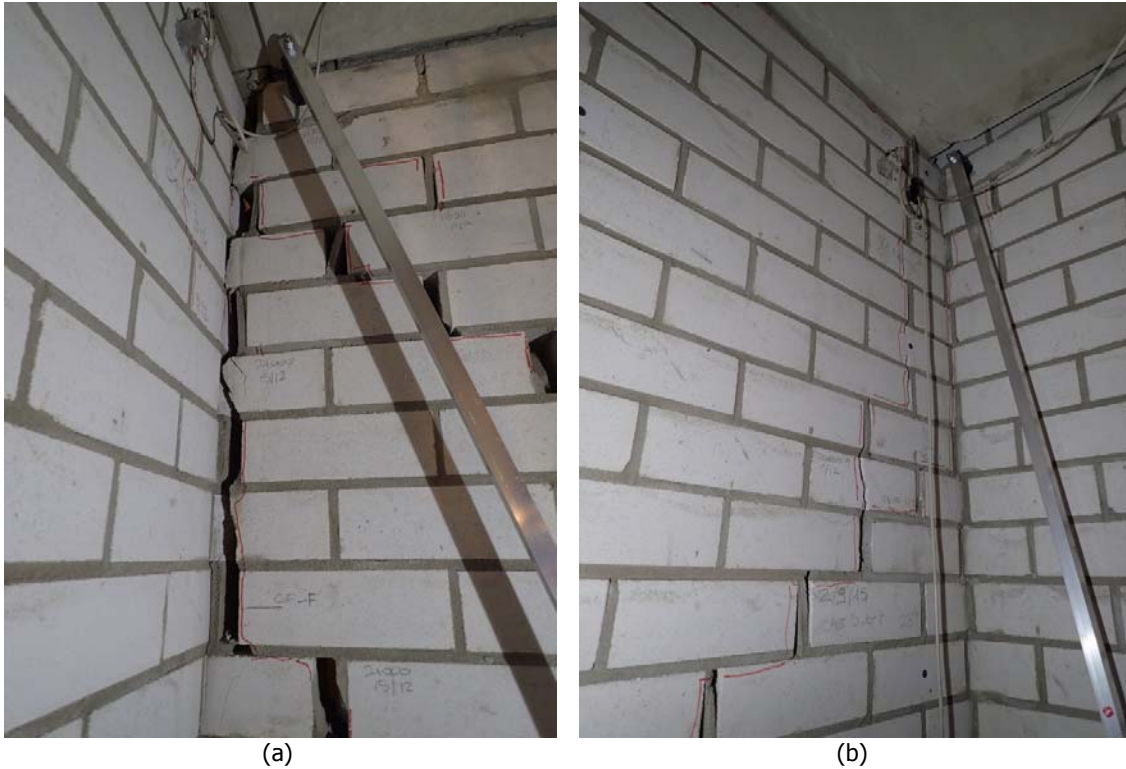


Figure E.39 – Post-peak phase **cycle 20**: (a) Crack between west wall and pier P3 (64_C20-GF-WP3); (b) crack between east wall and pier P2 (65_C20-GF-EP2).

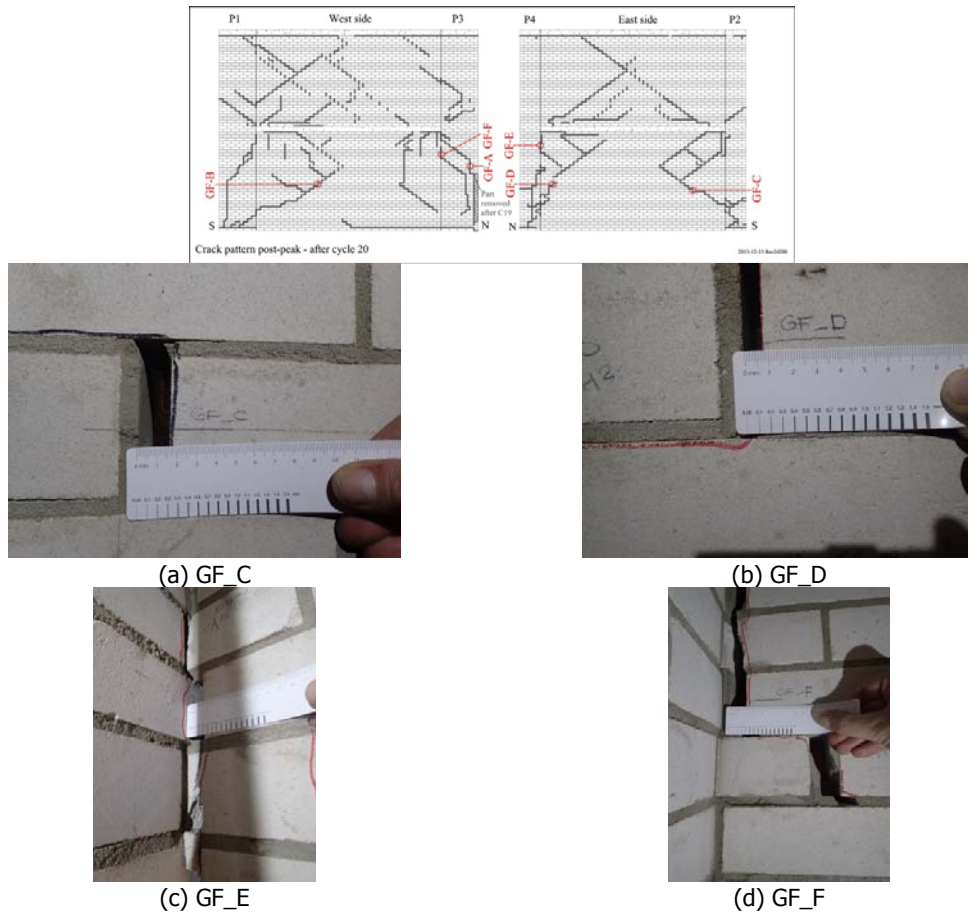


Figure E.40 – Post-peak phase cycle 20 – Crack width. Compare with Figure E.35.

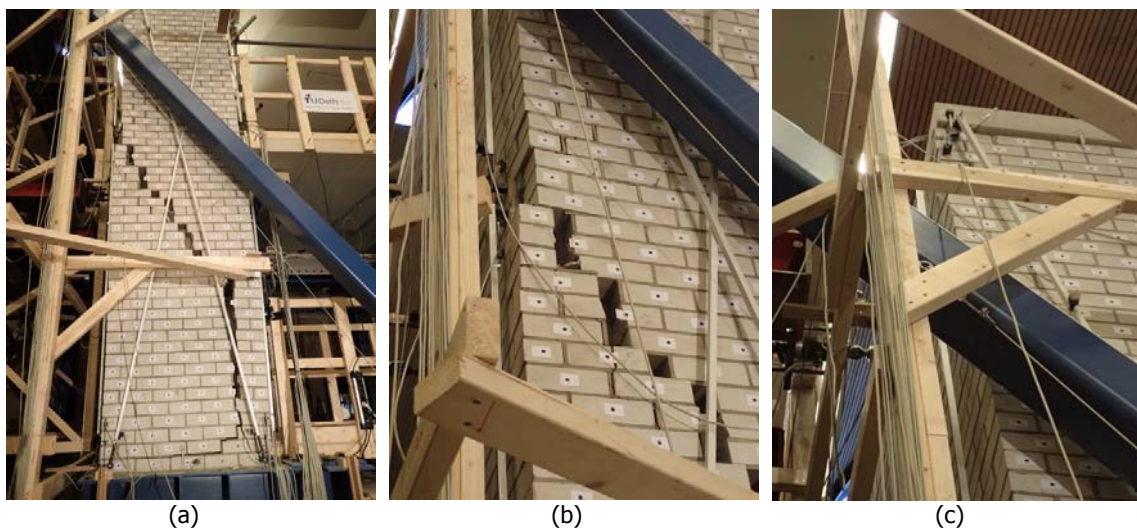


Figure E.41 – Post-peak phase cycle 21 – Vertical/diagonal crack on pier P1 (outside): (a) Overview (66_C21-P1); (b) Detail at the first floor slab (67_C21-GF-P1); (c) Detail at the second floor slab (68_C21-FF-P1). Compare with Figure E.36.



Figure E.42 – Post-peak phase **cycle 21**: (a) Cracks on pier P2 (69_C21-P2); (b) Crack on pier P4 (70_C20-P4). Compare with Figure E.37.

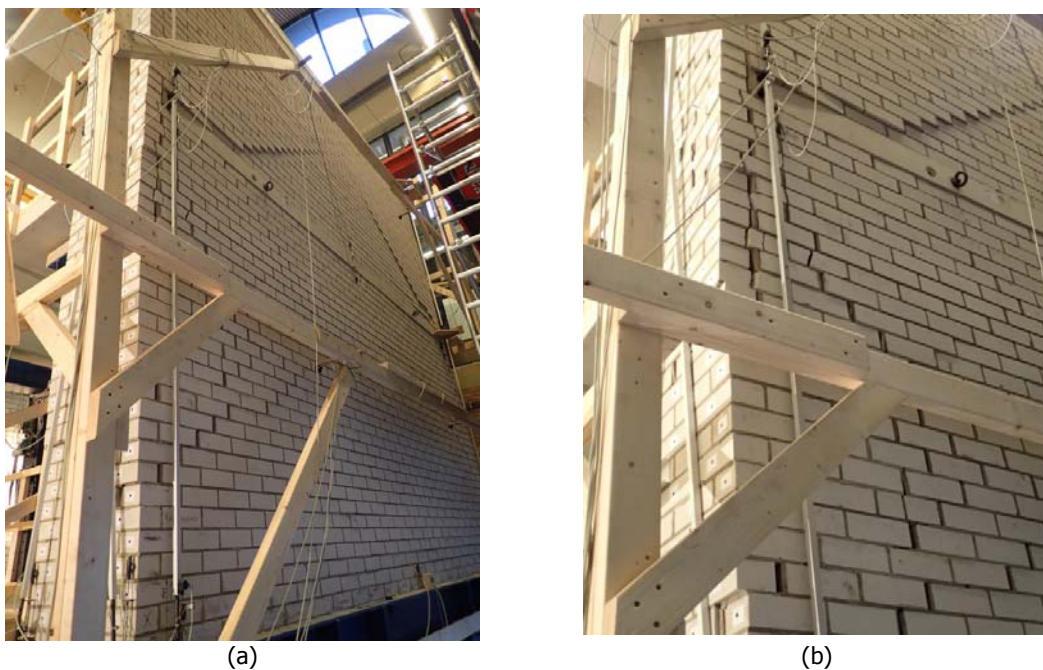


Figure E.43 – Post-peak phase **cycle 21**: (a) Cracks on east wall (71_C21-E); (b) Detail of figure (a) (72_C21-E).